

Atmosphere

Volume 14 Number 2 1976

Canadian Meteorological Society
Soci t  M t orologique du Canada

Atmosphere

Volume 14 Number 2 1976

Contents

61

Features of the Proportionality Coefficient in the Relationship
Between Visibility and Liquid Water Content in Haze and Fog
Claudio Tomasi and Francesco Tampieri

77

Spectra of Surface Atmospheric Quantities at Ocean Weathership P
David Fissel, Stephen Pond and Mikio Miyake

97

Meeting Announcements

98

Short-Term Forecasting with a Multi-Level Spectral Primitive Equation Model
Part I – Model Formulation
Roger Daley, Claude Girard, John Henderson and Ian Simmonds

117

Short-Term Forecasting with a Multi-Level Spectral Primitive Equation Model
Part II – Hemispheric Prognoses and Verification
Roger Daley, Claude Girard, John Henderson and Ian Simmonds

135

Notes and Correspondence

139

Book Reviews

143

Advertisement

ISSN 0004-6973

Canadian Meteorological Society
Société Météorologique du Canada

Features of the Proportionality Coefficient in the Relationship Between Visibility and Liquid Water Content in Haze and Fog

Claudio Tomasi and Francesco Tampieri

Sezione Microfisica dell'Atmosfera, C.N.R., Bologna, Italy

[Manuscript received 18 December 1975; in revised form 26 February 1976]

ABSTRACT

A wide set of size-distribution models of haze and fog droplets expressed in terms of the modified gamma distribution function have been used for evaluating the proportionality coefficient b in the empirical relationship between visibility V and liquid water content LWC , that is $V=b(LWC)^{-2/3}$, as proposed by Eldridge (1966). The evaluations of b turn out to be consistent with the values proposed in the literature and give evidence for its close dependence on the shape-parameters of the droplet size distribution, especially as regards the mode radius and the width of the larger-droplet wing. Three average relationship

curves are proposed respectively for dense haze, "dry and cold" fog and "wet and warm" fog.

Corresponding to these cases, three correlation lines are presented between b and the ratio of the volume extinction coefficient at $3.70 \mu\text{m}$ wavelength to that at $0.55 \mu\text{m}$, evaluated for the same uniform path in hazy and foggy atmospheres. Applied to measurements of infrared and visible transmission such correlation lines give the possibility of estimating the most proper value of b to be used in Eldridge's relationship for different atmospheric conditions.

1 Introduction

The relationship between atmospheric liquid water content and visibility involves several meteorological aspects related to the evolutionary processes of the droplet population in clouds and fog. Moreover the determination of liquid water content from simultaneously observed visibility has taken on great importance in the last few years as it has been discovered to play a fundamental role in some physico-chemical reactions occurring in the atmosphere. In fact oxidation processes of pollutant gases appear to take place inside the water droplets suspended in the atmosphere and turn out to be regulated by rates which are variably affected by the atmospheric liquid water content (see Junge and Ryan, 1958; Scott and Hobbs, 1967; Tomasi *et al.*, 1975).

Trabert (1901) derived a formula which predicts an inverse proportionality between visibility and liquid water content within clouds through an empirical factor which depends on the average radius of the droplet size-distribution.

Such a formula has been examined by aufm Kampe and Weickmann (1952) on the basis of droplet data collected in all types of cumulus clouds. They point out that the proportionality factor has a close dependence on the features of the droplet size spectrum. Best (1953) relates this factor to the shape parameters of his previously proposed formula for the drop-size distribution in cloud and fog (see Best, 1951).

By assuming a constant factor of proportionality, Trabert's (1901) formula tends to interpret the variations of visibility and liquid water content in terms of variable concentrations of the unvaried size-distribution. Thus, continuous and frequent choices of proper values of the proportionality factor have to correspond step by step to the slight variations which affect the evolving droplet size-distribution.

On the basis of continuous records of visibility and liquid water content, Houghton (1939) suggests that a proportionality between visibility and the $-2/3$ power of the liquid water content can more realistically describe the variations of the two atmospheric parameters associated with different evolutionary stages in the droplet population rather than by considering only modifications of the droplet concentration. Derived from an ample set of data pertaining to different evolutionary stages of fog, Eldridge (1966) proposes two best-fit empirical curves which have the general form

$$V = b (LWC)^{-2/3} \quad (1)$$

where V is the horizontal visibility expressed in kilometers, LWC is the liquid water content measured in grams per cubic meter of air and the proportionality coefficient b assumes the particular value of 0.017 for "dense haze and selective fog" and 0.024 for "stable and evolving fogs".

In particular, such a power law is consistent with computations based on large particle size distributions typical for urban areas and growing as a result of increasing relative humidity from 0.75 to 0.95 (see Tomasi *et al.*, 1975).

As regards the coefficient b of eq. (1), Platt (1970) suggests that low values should be related to "dry" or industrial-type haze and fogs having many more small droplets which grow in probable cold air masses whereas gradually higher values of b correspond to "wet" natural fogs characterized by increasing and predominant contents of larger though fewer droplets. Eldridge (1971) gives evidence for the influence of the width and of the radius range of the droplet size distribution on the coefficient b .

The purpose of the present paper is to study the dependence of b on the shape of the droplet size-distribution, especially with respect to the modal radius, and to suggest optical tools suitable for obtaining the most appropriate value of b for particular stages of development of fog-droplet populations evolving in the real atmosphere.

2 Size distribution models of haze and fog droplets

In a previous paper (Tampieri and Tomasi, 1976), a large number of empirical size spectra of fog droplets have been examined by a computational method

using the modified gamma distribution function proposed by Deirmendjian (1964, 1969). Such a size distribution function has the general form

$$n(r) = ar^\alpha \exp \left[-\frac{\alpha}{\gamma} \left(\frac{r}{r_c} \right)^\gamma \right], \quad 0 \leq r < \infty \quad (2)$$

where $n(r)$ is the volume concentration of droplets per unit radius (expressed in $\text{cm}^{-3} \mu\text{m}^{-1}$) at radius r (expressed in μm). The four parameters a , α , γ and r_c (this latter is the mode radius, i.e. the radius of maximum frequency) make this function very flexible for depicting variable and smoothed shapes so that it is satisfactory for fitting most of the empirical size spectra we have examined. The three parameters α , γ and r_c completely determine the shape of the distribution curve while the parameter a is such as to give for each size distribution a unit total concentration of droplets per cubic centimeter of air. If a certain droplet population is described by a modified gamma size-distribution model, as given by eq. (2) on the basis of appropriate values of the four parameters a , α , γ and r_c and N is its actual total concentration, then the real profile of such a droplet size distribution is obtained by multiplying this $n(r)$ by N .

The sets of the parameters α , γ , r_c and a giving the best-fit curves relative to eight size spectra of small water droplets measured by Garland (1971) and by Garland *et al.* (1973) are given in Table 1. These parameter sets give representative size-distribution models of haze droplets forming in air in which the relative humidity is very nearly equal to 1 and in which the availability of the water vapour is limited to such an extent as to inhibit their growth. In general, these distributions are characterized by the fraction of the smaller droplets which turns out to be gradually less important with respect to that of the larger droplets as r_c increases. Moreover, all such size-distribution curves give right wings which sharply drop in the radius range around $1 \mu\text{m}$. These features of the haze droplet size-distribution models are shown in Fig. 1, where the volume concentration of droplets per unit radius $n(r)$ is plotted as a function of the radius r for some representative size distributions of Table 1.

The wide spread of modified gamma size-distributions derived from empirical size spectra of fog droplets has been synthesized (Tampieri and Tomasi, 1976) into a limited number of average and representative droplet size-distribution models in terms of Deirmendjian's function. The parameter sets which determine all the size-distribution models we had found are listed in Tables 2 and 3, where the value of a gives for each model a unit total concentration of droplets per cubic centimeter of air. The general tendency of such average models is that the smaller-droplet wing gradually drops as r_c increases until the distributions become nearly symmetrical for the higher values of the mode radius. This behaviour is shown in Fig. 2, where the volume concentration of droplets per unit radius $n(r)$ is given as a function of the radius r for some representative models given in Tables 2 and 3 for well distinct values of the mode radius r_c .

3 Evaluation of the coefficient b and its dependence on the mode radius

The eight size-distributions of small water droplets reported in Table 1 have to

TABLE 1. Parameter sets of the modified gamma size distribution of small water droplets and concentration and liquid water content corresponding to 1 km horizontal visibility.

Size distributions	Parameter set				$N(\text{cm}^{-3})$	$LWC(\text{g m}^{-3})$
	$r_c(\mu\text{m})$	α	γ	a		
Garland (1971)						
21 Oct. 1968	0.734	7	1.25	3.7847×10^3	718.61	2.084×10^{-3}
23 Nov. 1968	0.374	3	0.94	8.0341×10^2	1356.72	1.481×10^{-3}
Garland et al. (1973)						
7 Dec. 1971 04:43hr	0.326	2	1.10	1.0268×10^2	1582.13	1.386×10^{-3}
04:48hr	0.295	2	1.00	1.5581×10^2	1707.83	1.377×10^{-3}
06:10hr	0.556	3	1.28	8.5200×10^1	886.52	1.917×10^{-3}
07:14hr	0.038	1	0.54	8.7474×10^2	9230.25	1.164×10^{-3}
10:05hr	0.315	2	1.03	1.2320×10^2	1572.83	1.441×10^{-3}
10:23hr	0.268	2	1.07	1.9091×10^2	2176.09	1.126×10^{-3}

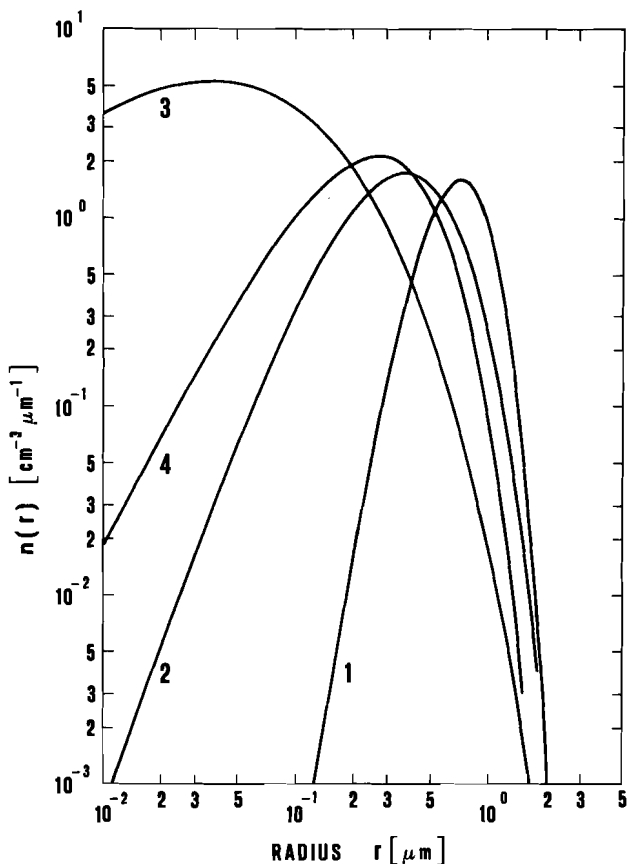


Fig. 1 Volume concentration of droplets per unit radius $n(r)$ as a function of the radius r for four modified gamma size-distribution models for haze droplets. The distribution curves are drawn for a unit total concentration of droplets per cubic centimeter of air. The sets of shape-parameters are given in Table 1: curve 1 corresponds to the size distribution 21 Oct. 1968; curve 2 to 23 Nov. 1968; curve 3 to 7 Dec. 1971, 07:14 hr; curve 4 to 7 Dec. 1971, 10:23 hr.

be related to the attenuation conditions in hazy atmospheres. As the horizontal visibility V ranges from 0.5 about 1.5 km in dense haze, we have assumed an average value of 1 km which permits us to find for each size-distribution the proper value of the total concentration of droplets N per cubic centimeter of air.

For this purpose we calculate for each size-distribution the volume extinction coefficient $\beta(\lambda)$ at wavelength $\lambda = 0.55 \mu\text{m}$ and for the sea-level atmospheric horizontal path of 1 km. This is obtained by integrating the weighted modified gamma size-distribution, according to

$$\beta(\lambda) = 10^{-3} a \pi \int_0^{\infty} r^{\alpha+2} \exp \left[-\frac{\alpha}{\gamma} \left(\frac{r}{r_c} \right)^{\gamma} \right] K(r, m(\lambda)) dr \quad (3)$$

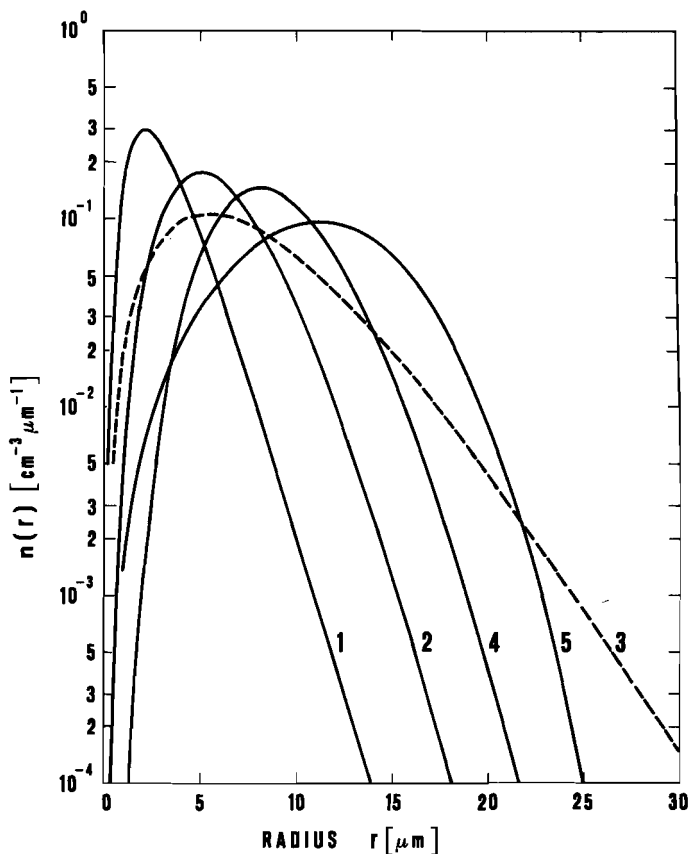


Fig. 2 Volume concentration of droplets per unit radius $n(r)$ as a function of the radius r for five size distribution models of fog droplets. The distribution curves are drawn for a unit total concentration of droplets per cubic centimeter of air. The sets of shape-parameters are given in Tables 2 and 3: curve 1 corresponds to the model radiation fog 1; curve 2 to radiation fog 2; curve 3 to arctic marine advection fog 2; curve 4 to advection fog 4; curve 5 to mature fog 5.

where $K(r, m(\lambda))$ is the total extinction efficiency factor for water spheres as given by Van de Hulst's (1957) approximation multiplied by the correction factors suggested by Deirmendjian (1960). The complex refractive index of the liquid water $m(\lambda)$ for $\lambda = 0.55 \mu\text{m}$ has been taken to be equal to $1.334 - i 1.5 \times 10^{-9}$, from Irvine and Pollack (1968).

Koschmieder's (1924) formula predicts that any haze droplet population gives a total extinction of 3.912 km^{-1} at $0.55 \mu\text{m}$ wavelength for the horizontal visual range of 1 km. On the other hand the total extinction is given by the total concentration N of droplets per cubic centimeter of air multiplied by the volume extinction coefficient $\beta(0.55 \mu\text{m})$ relative to a unit total concentration of droplets. Therefore the value of N , which is required to give the horizontal visual range of 1 km, is given by the ratio $3.912/\beta(0.55 \mu\text{m})$, where $\beta(0.55 \mu\text{m})$ has been calculated from eq. (3) for each set of shape-parameters of

TABLE 2. Parameter sets of the modified gamma size distribution of fog droplets and concentration and liquid water content corresponding to 0.2 km horizontal visibility.

Size-distribution models		Parameter sets				$N(\text{cm}^{-3})$	$LWC(\text{g m}^{-3})$
		$r_c(\mu\text{m})$	α	γ	a		
Radiation fog	1	2.13	4	0.70	4.3239×10^0	249.93	6.137×10^{-2}
	2	4.98	4	1.23	7.4438×10^{-3}	76.29	9.899×10^{-2}
	3	8.06	4	1.77	3.0410×10^{-4}	35.85	1.379×10^{-1}
	4	12.22	5	1.62	7.5475×10^{-6}	15.90	2.061×10^{-1}
Evaporation fog		1.86	4	0.56	3.0566×10^1	246.31	6.716×10^{-2}
Advection fog	1	2.75	4	0.85	4.9763×10^{-1}	184.55	6.795×10^{-2}
	2	5.04	5	1.17	4.2028×10^{-3}	78.75	9.534×10^{-2}
	3	6.20	3	1.05	8.1656×10^{-3}	37.73	1.537×10^{-1}
	4	8.10	6	1.47	3.0861×10^{-5}	36.13	1.348×10^{-1}
	5	21.16	5	3.09	8.9728×10^{-8}	6.50	3.059×10^{-1}
Arctic marine advection fog	1	3.07	1	0.98	1.0645×10^{-1}	51.89	1.627×10^{-1}
	2	5.40	2	1.09	2.2833×10^{-2}	39.33	1.597×10^{-1}
	3	7.85	3	1.15	2.6209×10^{-3}	25.66	1.830×10^{-1}
	4	10.37	2	2.97	1.7966×10^{-3}	24.08	1.701×10^{-1}
	5	12.88	5	1.93	3.6783×10^{-6}	15.31	2.060×10^{-1}

TABLE 3. Parameter sets of the modified gamma size distribution of valley fog droplets and concentration and liquid water content corresponding to 0.2 km horizontal visibility.

Size-distribution models		Parameter sets				$N(\text{cm}^{-3})$	$LWC(\text{g m}^{-3})$
		$r_c(\mu\text{m})$	α	γ	a		
Ground fog	1	0.86	1	0.89	1.3823×10^0	509.99	5.141×10^{-2}
	2	2.22	1	2.04	2.0338×10^{-1}	309.79	5.146×10^{-2}
Formation stage	1	3.49	3	1.26	5.6434×10^{-2}	138.04	7.548×10^{-2}
	2	7.50	5	1.40	2.1192×10^{-4}	39.32	1.325×10^{-1}
	3	9.07	5	1.69	4.0633×10^{-5}	29.26	1.504×10^{-1}
	4	10.82	4	2.17	5.1199×10^{-5}	21.73	1.738×10^{-1}
Mature fog	1	4.99	1	1.93	4.0001×10^{-2}	59.02	1.236×10^{-1}
	2	7.12	4	1.14	1.5416×10^{-3}	35.67	1.484×10^{-1}
	3	9.00	5	1.47	6.1487×10^{-5}	28.00	1.565×10^{-1}
	4	9.10	1	4.39	1.3900×10^{-2}	34.68	1.450×10^{-1}
	5	11.18	2	3.41	1.4058×10^{-3}	22.08	1.754×10^{-1}
Dissipation stage	1	6.92	4	0.94	3.3437×10^{-3}	32.51	1.623×10^{-1}
	2	10.10	4	2.00	8.0977×10^{-5}	24.14	1.662×10^{-1}

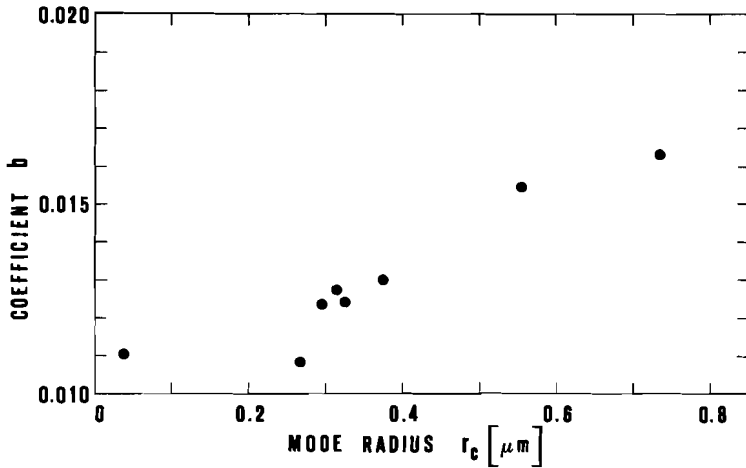


Fig. 3 Proportionality coefficient b of eq. (1) normalized to 1 km horizontal visibility and plotted versus the mode radius r_c for the eight modified gamma size-distributions of haze droplets listed in Table 1.

Table 1. These values of N are given for each droplet size-distribution in Table 1. Correspondingly the liquid water content expressed in grams per cubic metre of air can be computed from

$$LWC = \frac{4}{3} 10^{-6} a N \pi \rho \int_0^{\infty} r^{\alpha+3} \exp \left[-\frac{\alpha}{\gamma} \left(\frac{r}{r_c} \right)^{\gamma} \right] dr \quad (4)$$

where $\rho = 1 \text{ g cm}^{-3}$ is the density of the liquid water.

The values of LWC resulting from eq. (4) for the values of N obtained above are also given in Table 1. By introducing them into eq. (1) the values of the proportionality coefficient b have been derived for each haze droplet size-distribution of Table 1. The average value $V = 1 \text{ km}$ has been used throughout.

In Fig. 3 the values of the coefficient b we have found are plotted versus their mode radius r_c and range from 0.011 to 0.016 so that they turn out to be in good agreement with the value proposed by Eldridge (1966) for dense haze. Moreover, within the set of the presently adopted size-distribution models, Fig. 3 gives evidence for the tendency of b to increase rather regularly with the mode radius with an average slope of $0.009 \mu\text{m}^{-1}$.

The droplet size-distribution models of Tables 2 and 3 relative to different types and various evolutionary stages of fog have been normalized to 0.2 km horizontal visibility, as such a value of V corresponds to the average visual conditions occurring in foggy atmospheres.

Koschmieder's (1924) formula predicts that a total extinction by fog droplet populations of 19.56 km^{-1} corresponds to the horizontal visual range of 0.2 km. By following the above-adopted procedure, the total concentration N of droplets per cubic centimeter of air is given for each size-distribution model by the ratio $19.56/\beta(0.55 \mu\text{m})$ where the various $\beta(0.55 \mu\text{m})$ have been computed on the basis of eq. (3).

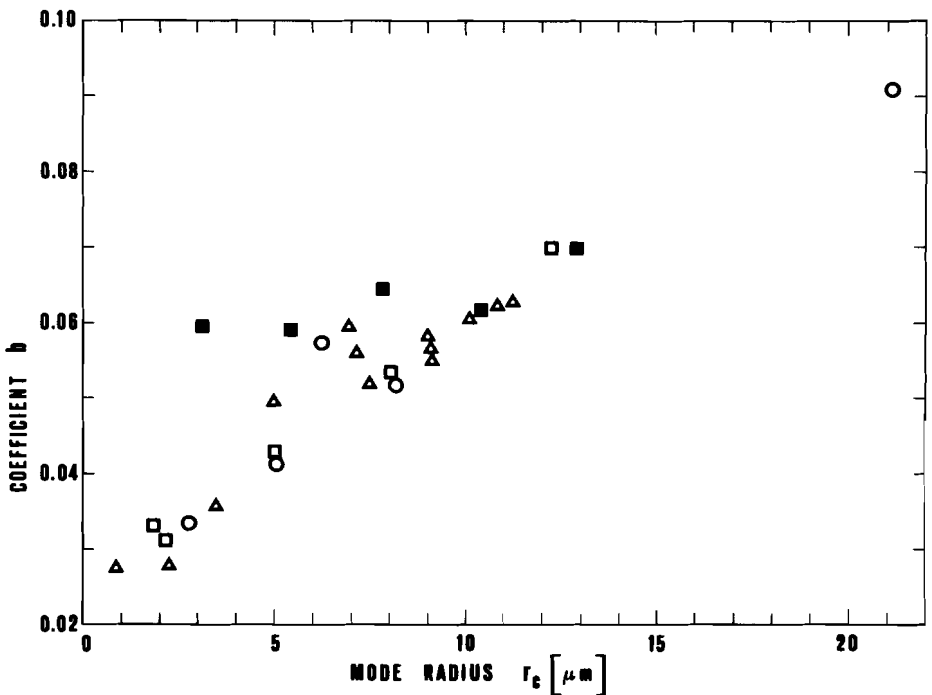


Fig. 4 Proportionality coefficient b of eq. (1) normalized to 0.2 km horizontal visibility and plotted versus the mode radius r_c for the modified gamma size-distribution models of fog droplets listed in Tables 2 and 3. Open squares refer to radiation and evaporation fogs. Open circles to advection fogs. Solid squares to arctic marine advection fogs. Triangles to valley fogs.

The resulting values of N and those of LWC we have derived from eq. (4) are given in Tables 2 and 3. Correspondingly the value of b for each size distribution of fog droplets has been computed from eq. (1). Fig. 4 shows the proportionality coefficient b versus the mode radius, indicating that it increases with r_c at an average rate of about $0.003 \mu\text{m}^{-1}$. The values of b cover the range from 0.03 to 0.07 which agrees well with the values proposed by Houghton and Radford (1938) and by Eldridge (1971). Some models concerning mostly arctic marine advection fogs exhibit values of b which are clearly higher than those given by the other fog models in the same range of the mode radius. On the other hand such values correspond to those size-distribution models which are characterized by broader shapes of the wing of the larger droplets, as one can verify from Tables 2 and 3 by considering that such models present lower values of the parameter α than the others and nearly equal values of the parameter γ (see also Fig. 2).

Following the suggestions of Platt (1970) such observations indicate that the coefficient b tends to assume gradually higher values as:

- i) the mode radius of the droplet size-distribution increases;
- ii) the fraction of the larger droplets predominates with respect to the others in such a way as to give large widths to the size distributions.

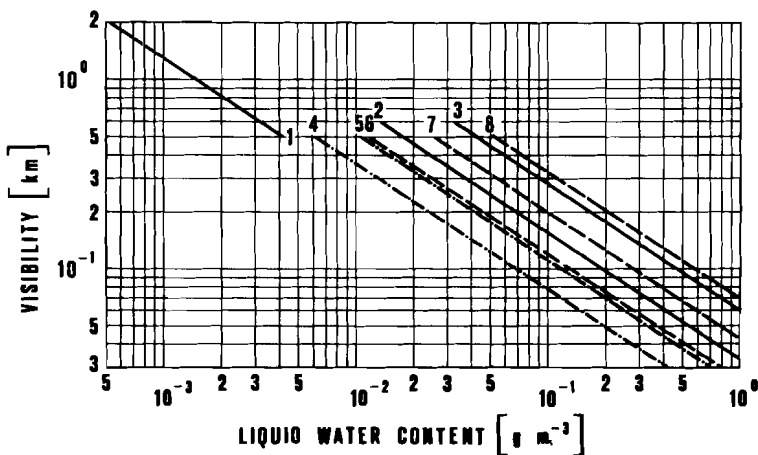


Fig. 5 Relationships between visibility and liquid water content. The curves 1, 2 and 3 correspond to the three average values of b proposed in the present paper: 1) $b = 0.013$ (dense haze); 2) $b = 0.034$ ("dry and cold" fog); 3) $b = 0.060$ ("wet and warm" fog). The curves 4 and 5 are those of Eldridge (1966): 4) $b = 0.017$ (dense haze and selective fog); 5) $b = 0.024$ (stable and evolving fog). The curves 6 and 7 correspond to those proposed by modification of the original data by Eldridge (1971): 6) b of about 0.026; 7) b of about 0.043. The curve 8 is relative to the data by Houghton and Radford (1938) and corresponds to a b of about 0.070.

On the basis of these results three average relationship curves can be proposed in terms of eq. (1) by adopting the following values of the coefficient b :

- 1) $b = 0.013$ for dense haze presenting mode radius of about $0.3 \mu\text{m}$;
- 2) $b = 0.034$ for fogs which are characterized by mode radius around $3 \mu\text{m}$ and predominant contents of small droplets ("dry and cold" fogs);
- 3) $b = 0.060$ for fogs which present mode radius around $9 \mu\text{m}$ and predominantly large droplets ("wet and warm" fogs).

In Fig. 5 these relationships are compared with the ones proposed by Eldridge (1966, 1971).

4 An optical procedure for the empirical determination of the coefficient b

The close dependence of the proportionality coefficient b of eq. (1) on the mode radius and on the shapes of the two wings of the droplet size distribution, which have different weight, leads us to search for a physical parameter which is immediately measurable and is conveniently and strictly related to the coefficient b . Such a parameter may be the volume extinction coefficient $\beta(\lambda)$, used above, which can be empirically obtained from monochromatic transmission measurements on atmospheric horizontal paths of known length. As evident in eq. (3), $\beta(\lambda)$ depends on the form of the size distribution $n(r)$ and on the geometrical cross section πr^2 of the droplets so that it turns out to be strongly affected by the same features of the droplet size distribution as those which determine the behaviour of the coefficient b . Moreover the use of $\beta(\lambda)$ at two wavelengths, the first in the visible, the second in the infrared, gives

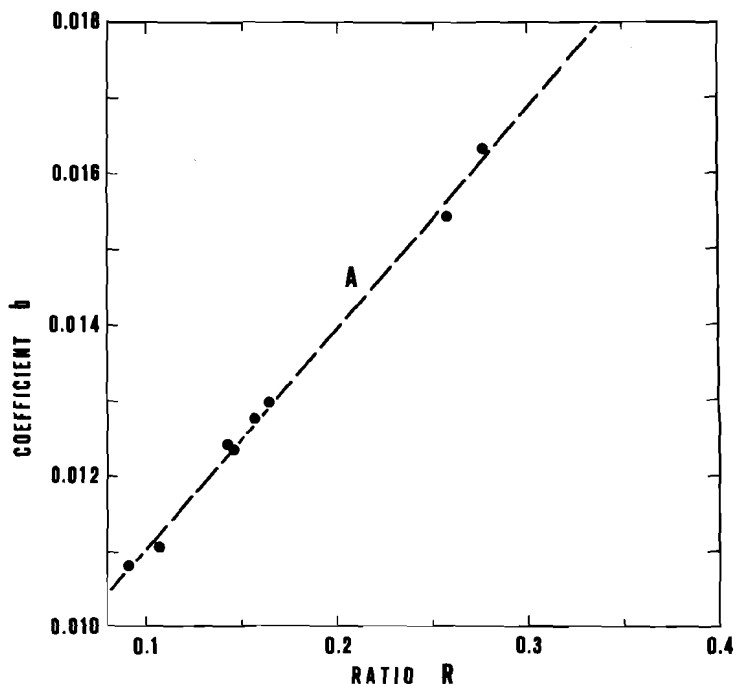


Fig. 6 Proportionality coefficient b of eq. (1) normalized to 1 km horizontal visibility and plotted versus the theoretically evaluated ratio $R = \beta(3.70 \mu\text{m}) / \beta(0.55 \mu\text{m})$ for the eight modified gamma size-distributions of haze droplets listed in Table 1. The correlation line A is given by eq. (5).

the possibility of shifting the extinction efficiency factor $K(r, m(\lambda))$ to give a weighting on the small-drop or large-drop portion of the distribution. The choice of an infrared wavelength of $3.70 \mu\text{m}$ corresponds to a spectral interval which is free from the strong absorption due to atmospheric water vapour bands and at the same time utilizes a relatively high value of the imaginary part of the refractive index $m(\lambda)$ of the liquid water. This choice renders the term $K(r, m(\lambda))$ and thus $\beta(3.70 \mu\text{m})$ particularly sensitive to the presence of large fog droplets on the atmospheric path. Simultaneous measurements on the same atmospheric path of spectral transmission at $0.55 \mu\text{m}$ wavelength, which corresponds to the visibility data, allow one to obtain valuable information about the extinction patterns of the atmosphere. Thus the ratio $R = \beta(3.70 \mu\text{m}) / \beta(0.55 \mu\text{m})$ should present features which can be related to the coefficient b through simple analytical expressions within the various size ranges proper for haze and fog droplets.

By assuming for $\lambda = 3.70 \mu\text{m}$ a value of $m(\lambda)$ equal to $1.382 - i 4.15 \times 10^{-3}$ (from Irvine and Pollack, 1968), the values of $\beta(3.70 \mu\text{m})$ have been computed for all the size distributions of Tables 1, 2 and 3 on the basis of eq. (3).

The values of the proportionality coefficient b for the eight size distributions of haze droplets are plotted versus the corresponding theoretical ratios R in

Fig. 6, which shows a close linear relationship between these two quantities in the range of R from 0.08 to 0.38. Such a relationship is well described by the correlation line A which is given by

$$b = 8.13 \times 10^{-3} + 2.91 \times 10^{-2} R \quad (5)$$

with a correlation coefficient of 0.998. The distributions from which eq. (5) is derived have modal radii less than $0.7 \mu\text{m}$. This relation makes it possible to estimate precisely the liquid water content of dense hazes from empirical measurements of spectral transmission.

Similarly the values of b relative to the size-distribution models of fog droplets are given in Fig. 7 versus the corresponding ratios R . The figure shows that for b greater than about 0.03 the dependence on the optical parameter R can be approximately represented by two distinct lines:

- in the range of R from 1.13 to 1.38 the coefficient b regularly decreases as R increases. Its trend is described by the correlation line C which corresponds to

$$b = 1.11 \times 10^{-1} - 6.08 \times 10^{-2} R \quad (6)$$

with the correlation coefficient of -0.957 . Eq. (6) appears to be related to size distributions of fog droplets characterized by the mode radius less than about $5 \mu\text{m}$, corresponding to "dry" fogs and to the initial stages of "wet" fogs.

- in the range of R from 1.13 to 1.05 the trend of b is represented by the correlation line D which is given by

$$b = 4.14 \times 10^{-1} - 3.29 \times 10^{-1} R \quad (7)$$

with the correlation coefficient of -0.948 . Eq. (7) includes size distributions of fog droplets centred at modal radii larger than about $5 \mu\text{m}$. In general such a relationship appears to be appropriate for the advanced stages of mature "wet" fogs.

The lines corresponding to eqs. (5), (6) and (7) fit the data with very high values of the correlation coefficient. This property, which demonstrates the close relationship between b and the optical parameter R as evaluated on the basis of Mie theory, can be ascribed to the capability of the ratio R of taking into account the important shape features of each size distribution.

5 Discussion of the results

As can be seen by comparing Figs. 3 and 4, there is an absence of values of the proportionality coefficient b between 0.016 and 0.028. If one considers unimodal configurations of the size distribution, such values would occur, corresponding to modal radii in the neighbourhood of $1 \mu\text{m}$. On the other hand Eldridge (1966, 1971) obtained values of b which cover this intermediate range from the examination of optical attenuation data in terms of bimodal size distributions consisting of haze droplets and of enough large droplets of fog.

Thus bimodal or multimodal profiles of the size distribution appear to give the possibility of characterizing the behaviour of b during the initial stages of fog formation. For this purpose, reliable concentrations and appropriate size-

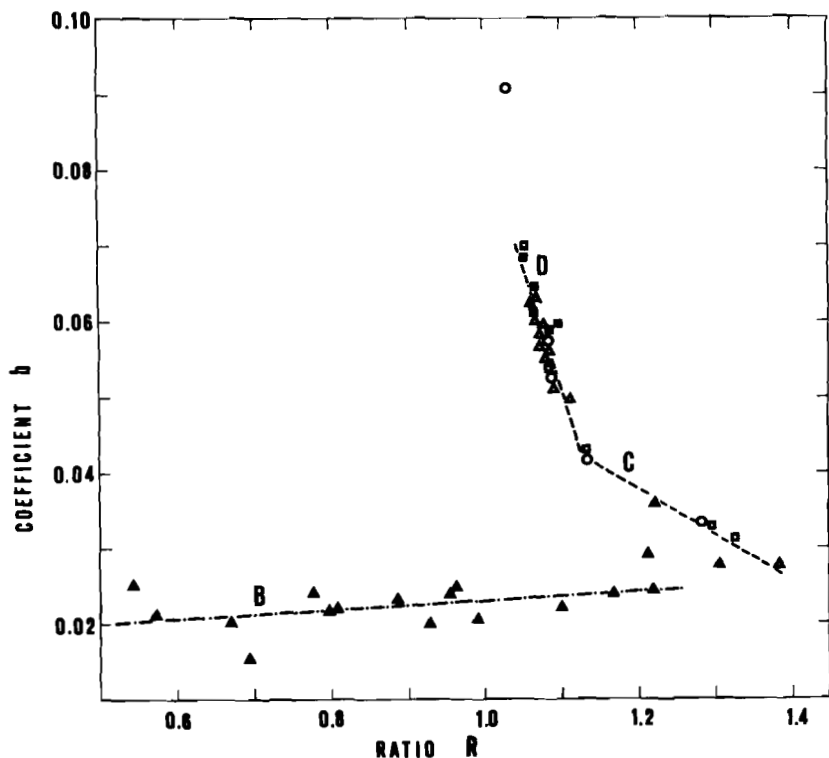


Fig. 7 Proportionality coefficient b of eq. (1) normalized to 0.2 km horizontal visibility and plotted versus the theoretical ratio $R = \beta(3.70 \mu\text{m}) / \beta(0.55 \mu\text{m})$ for the modified gamma size-distribution models of fog droplets listed in Tables 2 and 3. Open squares refer to radiation and evaporation fogs. Open circles to advection fogs. Solid squares to arctic marine advection fogs. Open triangles to valley fogs. The correlation line C is given by eq. (6). The correlation line D is given by eq. (7). In the lower side of the figure the solid triangles correspond to the data derived from the evaluations of Eldridge (1966) relative to bimodal size distributions of haze and fog droplets of various type. The correlation line B is given by eq. (8).

distribution models involving both haze and fog droplets should be chosen to closely reproduce the bimodal features which most frequently occur in the real atmosphere. This procedure would involve the use of a large set of concentration data and shape-parameters which should contribute to give realistic features to the bimodal size distributions. Moreover they should be related contemporaneously to many physical parameters which affect the growth processes of the water droplets. However, it may be assumed that those bimodal size distributions that result would present features which are intermediate between those proper for the small haze droplets of Table 1 and those typical of the size distributions of small fog droplets which are listed in Tables 2 and 3. From these data, the variations of b result as being related to the mean radius of these mixed populations of droplets through an average slope of about $0.01 \mu\text{m}^{-1}$.

A marked discontinuity affects also the dependence of b on the optical ratio R obtained on the basis of unimodal size-distribution models, as one can see from the comparison between the range of the correlation line A of Fig. 6, which is relative to haze droplets, and that of the line C of Fig. 7 concerning size distributions of fog droplets of intermediate sizes. In the region of the gap in R values between 0.38 and 1.38, the relationship between b and R can be investigated by using the data proposed by Eldridge (1966) in terms of bimodal size distributions of haze and fog droplets. The values of b have been calculated for each case from eq. (1) by adopting the data on visibility and liquid water content as estimated by Eldridge (1966) for evolving, selective and stable fogs. Correspondingly, the ratio R has been derived from the data of fog spectral attenuation examined in Eldridge's (1966) paper. Such values of b are plotted versus the ratio R in Fig. 7 showing that b rather regularly increases with the ratio R as the bimodal size distributions contain gradually more of large fog droplets. On the average the dependence of b on R can be represented by the best-fitting line B which is

$$b = 1.73 \times 10^{-2} + 5.96 \times 10^{-3} R \quad (8)$$

within the range of R from 0.38 to 1.38.

The opposite dependency of b on the ratio R in the lines A and B as opposed to the lines C and D can be explained in terms of the optically predominant radius range in the integral of eq. (3). In fact the extinction efficiency factor $K(r, m(\lambda))$ depends for each wavelength on the optical parameter $x = 2\pi r/\lambda$ and exhibits patterns characterized by a very sharp increase up to an x of about 6 and by wide oscillations in the upper range. On the other hand, b rather regularly increases with respect to the mean droplet radius within its whole range. Thus the linear approximation of the dependence of b on the ratio R as given by the line B agrees well with the features of the integral of eq. (3) and of the ratio R within the droplet size range which corresponds to the initial stages of fog formation.

Moreover the set of correlation lines we have proposed represents by simple and approximate formulas the dependence of the coefficient b on the ratio R . Such relations are probably characterized by a narrow maximum of R within the range of b around 0.03 and by a gradually decreasing profile which asymptotically tends to an R about equal to 1 for the highest values of b .

6 Conclusions

Based on a wide set of size-distribution models for haze and fog droplets of various type, the present procedure gives evaluations of the proportionality coefficient b to be used in eq. (1) which are in good agreement with those previously proposed by other authors. Moreover the average characteristics of the size-distribution models we use give evidence for the linear dependence of the coefficient b on the mode radius r_c of each size distribution. In particular, b turns out to be closely related also to the width of the wing for the larger droplets of the size distribution.

In the light of such general trends of b , the three relationships between visibility and liquid water content we have proposed in Fig. 5 correspond to three average and well diversified droplet populations which may be present in hazy and foggy atmospheres: small droplets in dense haze conditions, fog droplets growing to intermediate sizes by condensation in cold air masses, and "wet" large droplets formed in warm air masses.

The sensitivity of the coefficient b to the shape of the size distribution leads to the definition of a procedure based on the ratio between the optical thicknesses per unit length of an atmospheric horizontal path at $3.70 \mu\text{m}$ and $0.55 \mu\text{m}$ wavelengths. Such a methodology which can be applied to transmission measurements is supported by the proposed relationships of eqs. (5), (6), (7) and (8) for characterizing the most appropriate value of b to be used in eq. (1) according to the various configurations of the size distribution of haze and fog droplets, taking into account their different evolutionary stages.

References

- aufm KAMPE, H.J., and H.K. WEICKMANN, 1952: Trabert's formula and the determination of the water content in clouds. *J. Meteor.*, **9**, 167-171.
- BEST, A.C., 1951: Drop-size distribution in cloud and fog. *Quart. J. Roy. Meteor. Soc.*, **77**, 418-426.
- 1953: A modified form of Trabert's formula. *J. Meteor.*, **10**, 227-228.
- DEIRMENDJIAN, D., 1960: Atmospheric extinction of infra-red radiation. *Quart. J. Roy. Meteor. Soc.*, **86**, 371-381.
- 1964: Scattering and polarization properties of water clouds and hazes in the visible and infrared. *Appl. Opt.*, **3**, 187-196.
- 1969: *Electromagnetic scattering on spherical polydispersions*. Elsevier, New York, pp. 75-119.
- ELDRIDGE, R.G., 1966: Haze and fog aerosol distributions. *J. Atmos. Sci.*, **23**, 605-613.
- 1971: The relationship between visibility and liquid water content in fog. *J. Atmos. Sci.*, **28**, 1183-1186.
- GARLAND, J.A., 1971: Some fog droplet size distributions obtained by an impaction method. *Quart. J. Roy. Meteor. Soc.*, **97**, 483-494.
- , J.R. BRANSON and L.C. COX, 1973: A study of the contribution of pollution to visibility in a radiation fog. *Atmos. Environ.*, **7**, 1079-1092.
- HOUGHTON, H.G., 1939: On the relationship between visibility and the constitution of clouds and fog. *J. Aero. Sci.*, **6**, 408-411.
- and W.H. RADFORD, 1938: On the measurement of drop size and liquid water content in fogs and clouds. *Papers Phys. Oceanogr. Meteor.*, **6**, No. 4, 31 pp.
- IRVINE, W.M. and J.B. POLLACK, 1968: Infra-red optical properties of water and ice spheres. *Icarus*, **8**, 324-360.
- JUNGE, C.E. and T.G. RYAN, 1958: Study of the SO_2 oxidation in solution and its role in atmospheric chemistry. *Quart. J. Roy. Meteor. Soc.*, **84**, 46-55.
- KOSCHMIEDER, H., 1924: Theorie der horizontalen Sichtweite. *Beitr. Phys. Atmos.*, **12**, 33-55.
- PLATT, C.M.R., 1970: Transmission of sub-millimeter waves through water clouds and fogs. *J. Atmos. Sci.*, **27**, 421-425.
- SCOTT, W.D. and P.V. HOBBS, 1967: The formation of sulfate in water droplets. *J. Atmos. Sci.*, **24**, 54-57.
- TAMPIERI, F. and C. TOMASI, 1976: Size distribution models of fog and cloud droplets in terms of the modified gamma function. *Tellus*, **28**, to be published in No. 4.
- TOMASI, C., R. GUZZI and O. VITTORI, 1975: The " $\text{SO}_2 - \text{NH}_3$ - solution droplets" system in an urban atmosphere. *J. Atmos. Sci.*, **32**, 1580-1586.
- TRABERT, W., 1901: Die Extinction des Lichtes in einem trüben Medium (Sichtweite in Wolken). *Meteor. Z.*, **18**, 518-525.
- VAN DE HULST, H.C., 1957: *Light scattering by small particles*. Wiley, New York, pp. 174-183.

Spectra of Surface Atmospheric Quantities at Ocean Weathership P

David Fissel, Stephen Pond and Mikio Miyake
Institute of Oceanography,
University of British Columbia, Vancouver, B.C.

[Manuscript received 9 December 1975; in revised form 9 March 1976]

ABSTRACT

Ten years of surface weather data from Ocean Weather Station P were subjected to spectral analysis. The wind speed and air pressure auto-spectra reveal large variations at synoptic periods while the auto-spectra of the sea temperature, air temperature and absolute humidity are dominated by the annual variations. The rotary auto-spectrum of the wind features a broad peak of activity centered at a period of 3 days. In addition, the

spectra of quantities representative of the wind stress and sensible and latent heat fluxes are discussed. Spectra of these surface weather quantities computed for each season show that the activity changes both with respect to the size and frequency of the variations during the course of a year. The cross-spectra between selected pairs of quantities were also computed and are discussed.

1 Introduction

The atmosphere and the ocean are intricately coupled by a wide variety of physical phenomena. Such interactions take place over a very large range of time and space scales and it is useful to classify the types of interactions according to the characteristic scale size over which each occurs. In this study, the periodicities of surface layer meteorological and oceanographic quantities at Ocean Weather Station P in the N.E. Pacific are examined by means of spectral analysis of a ten year (1958–1967) time series of surface weather data. This technique allows computation of the contribution to the total variance at various frequencies. Periods ranging from 6 hours to two years are resolved. The cross-spectra between pairs of selected quantities were also computed. This analysis allows for the examination of the relationships between pairs of quantities at various frequencies.

Where possible, these spectral results are compared with previous results found by other investigators. Much work has been done on the spectra of wind speed at land and coastal weather stations but similar results for an open ocean environment are very limited. The previous work on spectra of the other quantities (such as air pressure, temperature and humidity) is even less extensive at both land and sea stations.

In order to examine the periodicities of air-sea transfer processes, the spectra of fluxes of momentum, sensible heat and water vapour were examined. These

fluxes are computed by means of bulk parameterization formulae (Roll, 1965). The momentum flux or wind stress (τ) can be written as

$$\tau = \rho C_D |U|U \quad (1)$$

where ρ is the air density, U is the mean wind velocity over a period of about an hour measured at some reference height, and C_D is the non-dimensional drag coefficient. Determinations of the wind stress or momentum flux with fairly direct estimates, show that $C_D = (1.3 \text{ to } 1.5) \times 10^{-3}$ on average with a considerable amount of scatter and an uncertainty of the mean of 20 to 30% (Pond *et al.*, 1974; Stewart, 1974). This coefficient may be a weak function of wind speed but as yet virtually no direct estimates have been made for winds greater than 15 m/s so this dependence remains uncertain.

Similar non-dimensional bulk transfer coefficients, C_T and C_q for sensible heat (H_S) and latent heat (H_L), respectively have been defined (Roll, 1965):

$$H_S = \rho C_T C_p U \Delta T \quad (2)$$

$$H_L = L C_q U \Delta q \quad (3)$$

where U is the mean wind speed over an hour (this is equal to $|U|$ within 1 to 2%), C_p is the specific heat of air at constant pressure, ΔT is the temperature difference between the sea surface and a reference height, L is the latent heat of vaporization per unit mass and Δq is the absolute humidity difference between the sea surface and a reference height. Direct estimates of C_T and C_q are rather limited, but those that are available indicate that both values are around 1.5×10^{-3} with a considerable amount of scatter (Pond *et al.*, 1974). Using equations (1), (2), and (3), values which are representative of fluxes of momentum ($|U|U$), sensible heat ($U\Delta T$) and latent heat ($U\Delta q$) were subjected to spectral analysis. The data from Station P were also used to investigate the effects of using averages much longer than one hour averages in formulae (1)–(3); this is often necessary at locations other than the ocean weather stations. The results of these computations are given in Fissel (1975) and will be reported elsewhere (Fissel and Pond, 1976).

2 Data and analysis

The data used in this study were collected by the Canadian Meteorological Service (now the Atmospheric Environment Service) at Ocean Weather Station P located at longitude 145W and latitude 50N approximately 1500 km west of Vancouver Island. The station was established in 1950 as one of a worldwide network of weatherships manned by various countries. The measurement program includes upper air soundings and routine surface meteorological readings.

The data were obtained from the Atmospheric Environment Service on digital magnetic tape in the International Meteorological format (80 column card images). These data, after some sorting and interpretation were transferred to another tape in a form more suitable for data processing. A description

of the procedure used in writing the second data tape and time series plots of selected quantities is found in Hertzman, Miyake and Pond (1974).

The data record is very nearly complete. Of the 175,296 possible samples (for 6 quantities recorded every 3 hours for ten years) only 1427, or 0.82% of the total, are missing or obviously incorrect. The worst case in the analysis that follows is for the seasonal spectra of the ten winters. Here, 1.5% of the values used are missing or incorrect. Of these 1427 values, 1404 are a result of the ship leaving its station and missing readings. The remaining 23 are apparently erroneous values. Examples of such errors are sea temperatures that suddenly plunge to 0.0°C , wet-bulb temperatures that exceed the air temperature by 0.5°C or more and wind directions that are greater than 360° .

In addition to the missing or incorrect data values discussed above, examination of the sea temperature time series plots revealed regular intervals of increased diurnal variations for the first five years of the data. Because the period of the increased activity is very nearly equal to the time that one ship is on station, it is thought that this effect is due to observers on one of the weatherships inadvertently exposing the surface water sample to the ambient air temperature for some time before taking the temperature; as a result, the sea temperature spectra discussed below are computed from all ten years of data but corrected at the diurnal period to agree with the diurnal spectral value computed from the last five years of data only.

In the time series subjected to spectral analysis, the missing and erroneous data values were replaced. The replacement values were simply determined by means of linear interpolation between the last correct value before the incorrect data and the first correct value following the incorrect data. This correction procedure will have little effect on the spectral contributions of periods longer than the period of replaced data but will reduce contributions at periods less than that of the replaced data. However, since the data replaced are a very small fraction of the total data, this effect is expected to be negligible.

The raw Fourier transform values were computed by means of a Fast Fourier Transform algorithm devised by Singleton (1969). The raw auto-spectral (also known as power spectral) and cross-spectral estimates were computed following the definitions of Jenkins and Watts (1968). For the wind, a vector time series, rotary auto- and cross-spectral estimates were computed following the method described by Mooers (1973). This technique resolves contributions to the variance and the covariance from two oppositely rotating vectors at discrete frequencies ranging from the fundamental to the Nyquist frequency. In addition, the derived rotary spectral quantities are independent of the coordinate system.

Due to the large number of data points used for calculating the spectral values, the frequency range is correspondingly large. In some of the spectra to be discussed, the frequency range is more than three decades. This wide range makes necessary the use of a logarithmic scale for frequency in the spectral plots. In order to display the relative contributions to total variance at different frequencies, the ordinate of the spectral plots is the product of the

spectral density $\phi(f)$ and the frequency. The use of graphs with $f\phi(f)$ plotted against $\log f$ ensures that equal areas under the plotted curve contribute equal amounts to the variance of the quantity being analysed. The spectral estimates were band-averaged in such a way that each smoothed estimate is nearly equally spaced on the logarithmic plots. For example, the first four estimates were computed from single frequency points (no frequency smoothing), the next estimate is averaged from 2 points, then 3 points and so on up to several hundred points per estimate. The number of points used for smoothing was chosen so that about 8 smoothed spectral estimates were produced for each decade of frequencies.

While this band averaging scheme is well suited to broad band (continuum) processes, it tends to obscure narrow band (line) processes at higher frequencies. To avoid missing significant line spectral peaks, single band auto-spectral values were examined at natural periods for which line spectral responses might occur: the diurnal, semi-diurnal (12 hours) and their overtones (8 and 6 hours) and the inertial period (18 hours at 50°N).

The total time series record was subdivided into N blocks and the frequency-smoothed spectral estimates were computed for each block. These estimates were then ensemble-averaged in order to provide further smoothing and to provide an empirical estimate of the statistical variability. The error bars shown on the graphs are the approximate 95% confidence intervals of the mean, computed as $\pm 2\sigma/(\sqrt{N-1})$ where σ is the standard deviation about the mean. To find the spectral character of each quantity the entire ten year record was divided into five blocks each of nearly two years duration ($N = 5$). The seasonal spectra were computed from 4, 3-month blocks of each year and averaged over the ten years for each season ($N = 10$). In order to make use of the available data, the 'seasons' were shifted slightly from the natural seasons. For example, the first day of winter for our purposes was taken to be Jan. 1 rather than Dec. 21. A more detailed description can be found in Fissel (1975).

Before the seasonal spectra were computed, the data were processed by the computer to effectively high-pass filter it. This filtering was done to remove the annual cycle from the signals. Otherwise, a large trend would be present in the time series making up the seasons which could produce large, fictitious spectral values at the low frequencies.

3 Auto-spectral results

The most striking feature of the wind speed spectrum (see Fig. 1a) is the broad synoptic peak at 3.1 days (0.32 cycles/day), a result of the passage of cyclones, anti-cyclones and their frontal systems. The peak which includes contributions from a wide range of scales (having its half-power points at periods of 10 days (0.1 cpd) and 1.3 days (0.77 cpd)) emphasizes the irregular nature of the passage of synoptic scale disturbances. The wind speed spectrum shows little variation at periods longer than one month with the exception of an important annual cycle. The annual cycle, seen as a peak at one year and a secondary peak at one-half year, due to some distortion, has a total variance

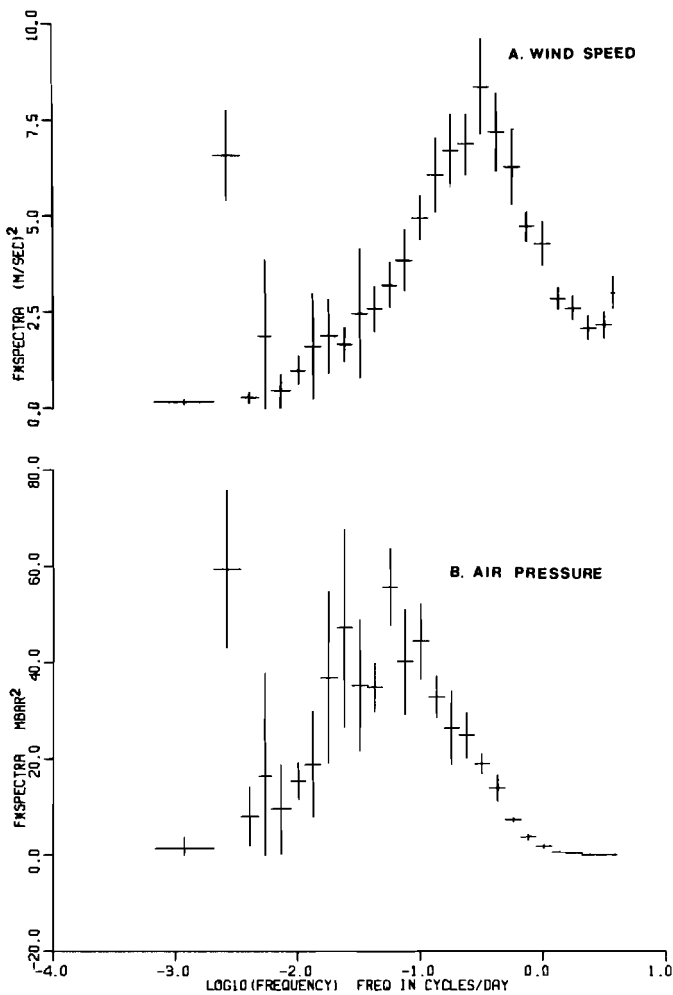


Fig. 1 The auto-spectra of (a) wind speed and (b) air pressure computed from five two-yearly data blocks over the period, 1958 to 1967. The vertical error bars represent approximate 95% confidence intervals about the mean of each spectral estimate.

of $3.9 \text{ m}^2/\text{s}^2$. This corresponds to an average annual range ($2[2 \cdot \text{variance}]^{1/2}$) of 5.7 m/s.

At the high frequency end of the spectrum, the graph shows a steady decline to periods of about 9 h (2.7 cpd) and then an increase out to the Nyquist period of 6 h (4 cpd). This upturn at the smallest periods is believed due to variance at smaller scales between 6 h and the 10 min instrumental averaging period being aliased back into the spectrum at lower frequencies. Because in our plots the spectrum is multiplied by frequency, the contributions due to aliasing are more apparent at small periods than at large periods (for a discussion of this effect see Oort and Taylor, 1969).

Fig. 1a shows no peak at the diurnal or semi-diurnal periods but a closer examination of single harmonics of the spectral values reveals some activity. The largest amount of energy is found in a semi-diurnal peak with a contribution to the variance of $0.022 \text{ m}^2/\text{s}^2$ corresponding to an average range of 0.42 m/s . At the diurnal period a small peak is found but it is not significant.

Several spectra of wind speed in the surface layer have been published. Oort and Taylor (1969) presented the wind speed spectrum for Caribou, Maine, a station with a continental climate. Van der Hoven (1957) has computed the wind speed spectrum at Brookhaven, on Long Island, New York. Wind spectra at stations on the Oregon coast are found in Frye *et al.* (1972) and Burt *et al.* (1974) while Hwang (1970) presents a wind spectrum for the tropical Pacific island of Palmyra. At stations over the open ocean, wind speed spectra have been computed by Byshev and Ivanov (1969), Millard (1971) and Dorman (1974). A summary of the results of these investigators, together with the important data parameters, is found in Table 1. A comparison with the results of these investigators indicates that the wind spectrum has the same general characteristics at each location: a dominant synoptic peak (ranging from periods of 2 to 12 days) and less important annual and diurnal (and/or semi-diurnal) peaks. At Station P, the level of the synoptic peak is comparatively high and the period short, reflecting the frequent passage of weather systems over this part of the North Pacific Ocean.

The differences among the results of Oort and Taylor (1969) and Byshev and Ivanov (1969) and those of this study, all at roughly the same latitude, indicate that important zonal variations exist in the wind speed spectrum. These may be due to local effects such as the limited fetches and different roughness characteristics of land in comparison with the open ocean and the position of the observation station in relation to anomalous meteorological regions such as areas associated with frequent cyclogenesis or frequent blocking patterns.

The spectrum of atmospheric pressure (see Fig. 1b), like the wind speed spectrum, is dominated by a broad, somewhat irregular peak at intermediate periods. However, this peak ranges over longer periods than that of the wind speed, having its half-power points at periods of 70 days (0.014 cpd) and 3 days (0.33 cpd). The spectrum also reveals a large annual periodicity in the air pressure by the presence of a peak at one year (0.0027 cpd) and a smaller peak at a period of one-half year (0.0055 cpd). The spectrum at the shortest periods or highest frequencies is notable for its very low levels. There is no evidence of any aliasing at these periods.

An examination of the single harmonic spectral values of the air pressure reveals a sharp semi-diurnal peak with a variance of 0.037 (mb)^2 corresponding to an average range of 0.55 mb . Smaller variations are found at periods of one day and one-third of a day.

Unlike the wind and pressure spectra discussed above, the spectra of sea temperature, air temperature and absolute humidity are dominated by annual and semi-annual variations (see Fig. 2). The variations at shorter periods,

TABLE 1. A summary of the period and level ($f\phi$) of the synoptic peak of the wind speed spectra as determined by various investigators. Z is the height of the anemometer and U is the mean wind speed of the data analyzed. In cases where these values were not available, a '—' is shown.

Investigators	Location	Z (m)	U m/s	Data Period	Synoptic	
					Period (days)	Level (m/s) ²
Van der Hoven (1957)	40N 73W	108	—	Aug. 1955 to Feb. 1956	4	5
Oort and Taylor (1969)	47N 68W	11	—	Jan. 1949 to Dec. 1958	3.9	3
Byshev and Ivanov (1969)	53N 36W	—	—	Jan. 1961 to Dec. 1963	6.4	5
	44N 41W	—	—			
	8S 14W	—	—	July 1957 to July 1958	12	1
	16S 6W	—	—			
Hwang (1970)	6N 162W	2	—	Mar. 1967 to May 1967	5.9	1.1
Millard (1971)	30N 70W	—	5.7	Apr. 1967 to June 1967	4	6
Frye et al. (1972)	45N 125W	20	—	July 1970 to Aug. 1970	2	3.5
					5	1.5
Burt et al. (1974)	45N 125W	10	11.8	Aug. 1970	3.0	7.5
Dorman (1974)	30N 140W	25	6.2	Jan. 1951 to Dec. 1970	8	2.9
This Study	50N 145W	22	10.1	Jan. 1958 to Dec. 1967	3	8.2

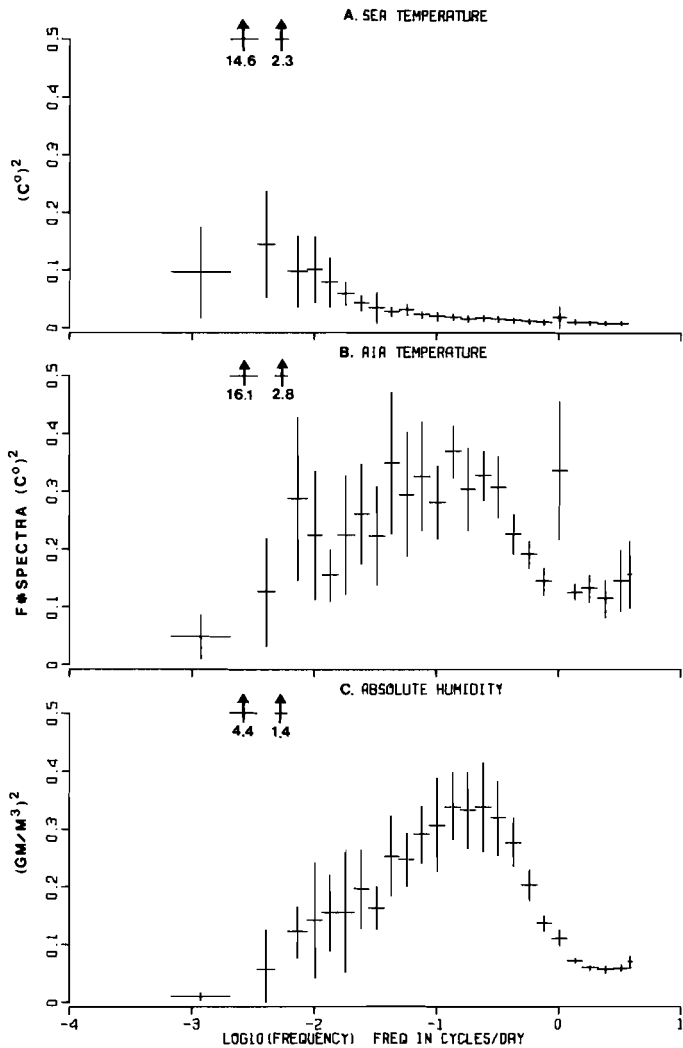


Fig. 2 The auto-spectra of (a) the sea temperature, (b) air temperature and (c) absolute humidity computed from five two-yearly data blocks over the period, 1958 to 1967. The vertical error bars represent approximate 95% confidence intervals about the mean of each spectral estimate. At the annual and semi-annual periods, the spectral levels are off-scale as indicated by the bold arrows with the numerical values written below the arrows.

though relatively small, are of considerable interest. The sea temperature spectrum declines steadily with decreasing periods (with the exception of a peak at 1 cpd) indicating no synoptic periods of increased activity. The air temperature spectrum reveals a very broad, uneven peak between periods of 2 days (0.5 cpd) and 60 days (0.017 cpd) with spectral levels that are an order of magnitude larger than the corresponding sea temperature spectrum. This broad region of increased activity seems to be associated with the passage

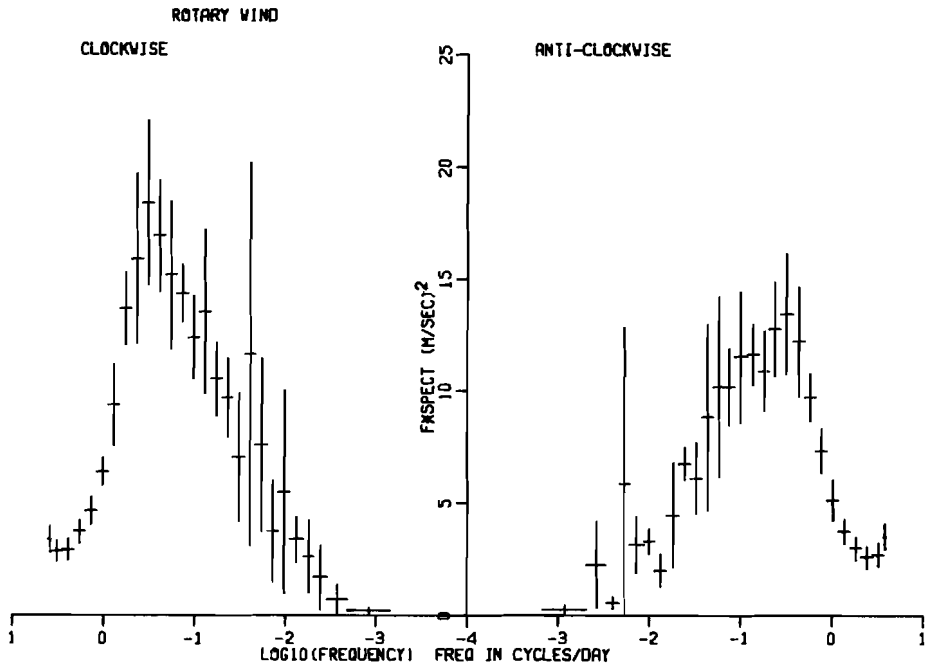


Fig. 3 The rotary auto-spectrum of the wind computed from five two-yearly data blocks over the period, 1958 to 1967. The vertical error bars represent approximate 95% confidence intervals of the mean of each spectral estimate.

of different air masses. The synoptic peak of the humidity spectrum is somewhat sharper than that of the air temperature spectrum and the level is somewhat higher relative to the annual peak.

The behaviors of the three quantities at the diurnal period show major differences. As expected, the air temperature has the largest diurnal variation corresponding to an average daily temperature range of 0.64°C . This variation changes with season being largest in spring and summer. The single harmonic spectral values of sea temperature show a very small but statistically significant diurnal variation corresponding to an average daily range of 0.13°C over the entire year. The diurnal variation is largest in spring and virtually disappears in winter. Denman (1973) has developed a model of the upper layer of the ocean which was tested for the months of May and June at Station P. His model, using a constant wind speed of 8 m/s, predicts a diurnal sea temperature range of 0.18°C . This result is very close to the spring value found in this analysis of 0.19°C . The absolute humidity has a small but significant diurnal variation corresponding to an average daily range of 0.11 g/m^3 (about an average absolute humidity of 7.35 g/m^3).

Fig. 3 shows the rotary wind spectrum. The synoptic peak dominates both the anti-clockwise and clockwise spectra with each having the peak occurring at a period of 3 days. The levels of the peaks differ: the clockwise peak has $f\phi = 18.4\text{ (m/s)}^2$ compared to $f\phi = 13.5\text{ (m/s)}^2$ for the anti-clockwise peak.

This result can be explained by the general pattern of synoptic weather system movements in the N.E. Pacific. The most common storm track is to the north of Station P over the Gulf of Alaska (see U.S. Navy, Marine Climatic Atlases). Eastward moving weather systems, whether cyclonic or anti-cyclonic, when passing to the north of the observation station, cause the observed wind to rotate in a clockwise manner. Consider, for example, the passage of an eastward moving cyclonic system to the north of the observation station (the most common situation at Station P). As it passes by, this would cause the observed wind to change from southwesterly to westerly to northwesterly in direction. That is, the wind rotates in a clockwise sense. Weather systems moving to the south of Station P, make greater contributions to the anti-clockwise spectrum. Of course, the situation is complicated by such events as the passage of storm fronts with their abrupt changes in wind direction. Nevertheless, the computed rotary spectrum appears to differentiate between the passage of weather systems to the north and south of the observation station and is consistent with the known pattern of pressure system movements.

The rotary wind stress spectrum is similar to the rotary wind spectrum with both clockwise and anti-clockwise rotations having a synoptic peak at 3 days. The clockwise rotations dominate the wind stress rotary spectrum to a greater extent than the wind rotary spectrum.

Spectra of quantities that are representative of turbulent heat transports are displayed in Fig. 4. The figure contains three plots: a plot of the spectrum of $U\Delta T$ which by equation (2) is proportional to the sensible heat flux, a plot of the spectrum of $U\Delta q$ which by equation (3) is proportional to the latent heat flux and a plot of the spectrum of $1.2 U\Delta T + 2.44 U\Delta q$ which is proportional to the total turbulent heat transport (taking $\rho = 1.2 \times 10^{-3} \text{ g/cm}^3$, $L = 2440 \text{ joules/g}$, $C_p = 1.00 \text{ joules/g-}^\circ\text{C}$ and $C_T = C_q$ in equations (2) and (3)). Each plot in Figure 4 is scaled in such a way that equal displacements from the horizontal axis represent equal contributions to the variance of the total heat flux. Each spectrum has the same general features: relatively small but significant amounts of energy at the annual and semi-annual periods and a broad synoptic peak that contains most of the energy. The synoptic peak has its highest levels at periods of 7 and 4 days (0.14 and 0.25 cpd) for each of the quantities.

It is clear from Fig. 4 that the auto-spectral values of the total heat flux represent considerably more heat transfer variations than the sum of the sensible and latent heat flux auto-spectral values at all periods greater than one day. This is a result of the high correlation between $U\Delta T$ and $U\Delta q$ variations. Over periods from two days to two years, the correlation between $U\Delta T$ and $U\Delta q$ is 0.7 or greater.

On the plots in Fig. 4, the semi-annual peaks are larger than the annual peaks because in the $\log f$ plots the bandwidth is narrower at the semi-annual period. However, the contribution to the variance from the semi-annual period is less than that from the annual period.

An inspection of the single harmonic values shows a very sharp diurnal

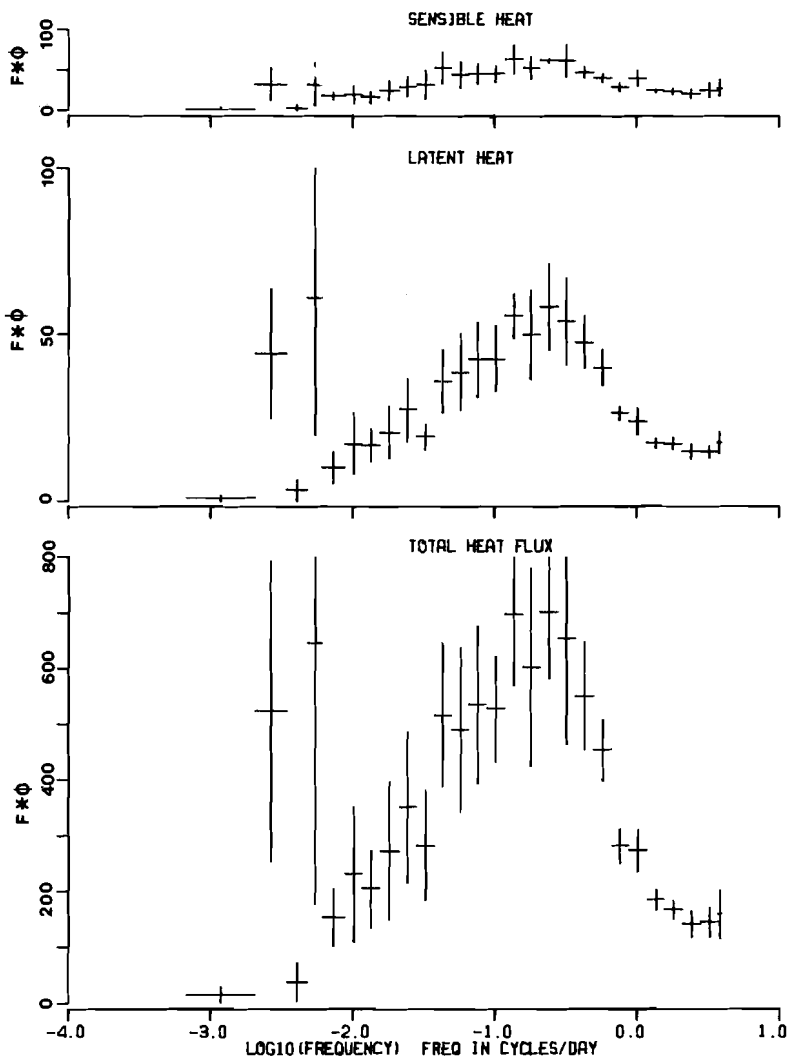


Fig. 4 The auto-spectra of $U\Delta T$ (in $(^{\circ}\text{C}\cdot\text{m}/\text{sec})^2$, representative of the sensible heat flux), $U\Delta q$ (in $(\text{gm}/\text{m}^2\cdot\text{sec})^2$, representative of the latent heat flux) and $1.2 U\Delta T + 2.44 U\Delta q$ (representative of the total turbulent heat flux).

peak in the $U\Delta T$ spectrum. This peak has an energy of $2.27 (^{\circ}\text{C m}/\text{s})^2$ corresponding to an average daily range of the sensible heat flux of $16.9 \text{ cal}/(\text{cm}^2 \text{ day})$. A smaller semidiurnal peak is found as well. The $U\Delta q$ spectrum shows no diurnal peak and only a very small semi-diurnal peak. Thus, there exists no daily cycle in latent heat transport similar to that of sensible heat transport. The spectrum of the total heat flux shows a prominent diurnal peak and a smaller semi-diurnal peak. The average diurnal range is $18.9 \text{ cal}/(\text{cm}^2 \text{ day})$, very nearly equal to that of the sensible heat flux, which suggests the variation is largely due to the daily sensible heat cycle.

TABLE 2. Integrals under auto-spectra. Note that the fundamental frequency for the seasonal spectra and the overall spectra is one cycle in 91 days and one cycle in 729 days, respectively. The highest frequency resolved in both cases is one cycle in 6 hours.

Quantity	Integral				
	Overall	Winter	Spring	Summer	Fall
Wind Speed (m/s) ²	28.3	28.1	19.4	16.9	31.4
Clockwise U (m/s) ²	63.0	75.8	43.7	36.7	80.7
Anti-Clockwise U (m/s) ²	50.5	60.0	34.8	28.2	61.8
Pressure (mb) ²	176.	194.	87.1	70.6	175.
Sea Temperature (C°) ²	8.46	0.106	0.179	0.248	0.172
Air Temperature (C°) ²	10.7	1.83	0.949	0.837	2.19
Absolute Humidity (c/m ³) ²	3.94	1.11	0.726	1.28	1.72
Clockwise UU (m/s) ⁴	18200	23400	9290	7300	28900
Anti-clockwise UU (m/s) ⁴	13200	16900	7130	5060	19500
Sensible Heat Flux (cal/(cm ² day)) ²	4130	5020	1500	952	6850
Latent Heat Flux (cal/(cm ² day)) ²	14300	12400	5130	6870	22100

4 Seasonal spectra

The spectra of each quantity were analysed separately for each of the seasons. In general, important changes are found between one season and another. The integrals of the spectral densities for each quantity for the four seasons are listed in Table 2. The integrals under the spectra for the ten year record are also given. Note that these values are often larger than the average of the seasonal values because of the wider bandwidth (in particular, the annual cycle is included).

Important changes in the wind speed spectra occur between one season and another. Fig. 5 shows the wind speed spectra calculated separately for the four seasons with each season's spectrum being averaged over the ten years. Dif-

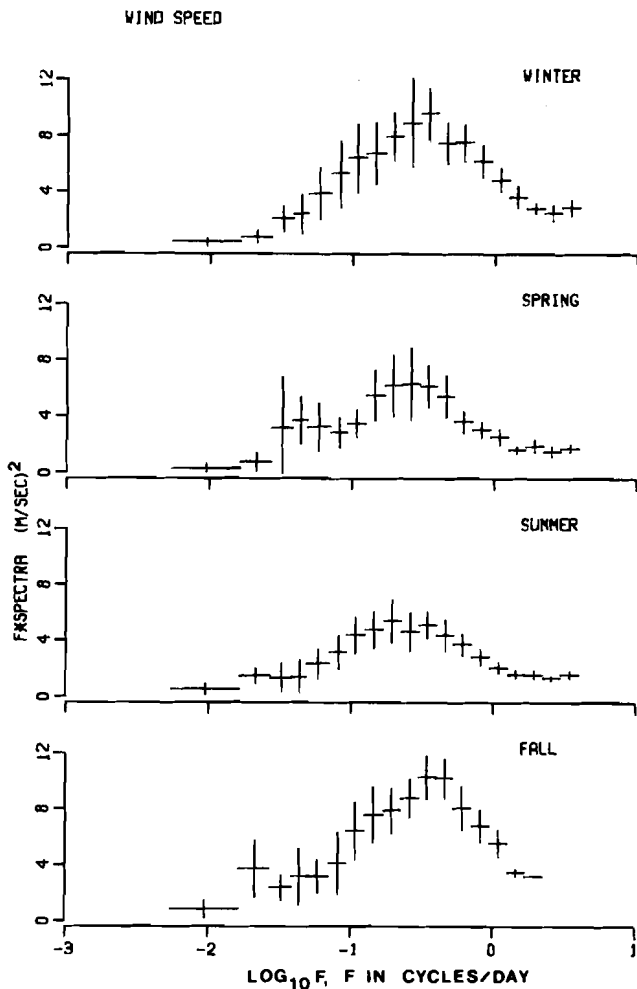


Fig. 5 Wind speed spectra for each of the seasons averaged over the ten years, 1958 to 1967. The vertical error bars represent approximate 95% confidence intervals of the mean of each spectral estimate.

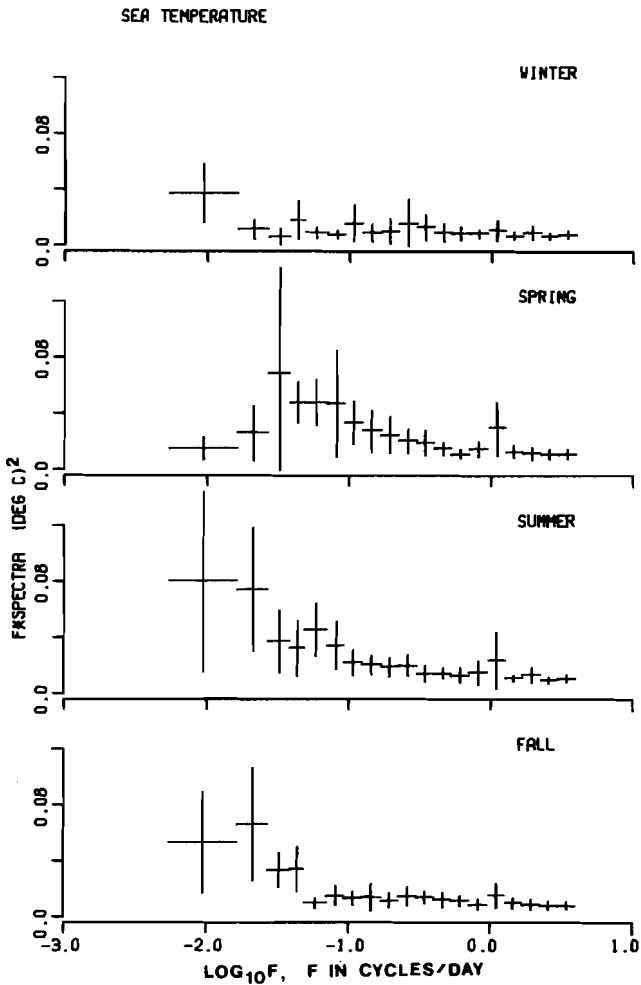


Fig. 6 Sea temperature spectra for each of the seasons averaged over the ten years, 1958 to 1967.

ferences are found in both the level and the period of the synoptic peak. The peak is largest in the fall ($f\phi = 10.3 \text{ m}^2/\text{s}^2$) declining through the winter ($9.7 \text{ m}^2/\text{s}^2$) and spring ($6.4 \text{ m}^2/\text{s}^2$) to the lowest level in summer ($5.5 \text{ m}^2/\text{s}^2$). The period at which the peak occurs shows a similar variation being smallest in fall (2.5 days or 0.4 cpd) increasing through winter and spring and being largest in summer (4.4 days or 0.23 cpd). These results illustrate the general seasonal pattern of synoptic disturbances which occur more frequently and with greater intensity in the fall and winter than in the spring and summer. In the spring and fall, there is some evidence of activity at longer periods (20 to 45 days or 0.05 to 0.022 cpd) but in both cases the peaks are not statistically significant.

The same general patterns of low spectral activity in the spring and summer and high spectral activity in the fall and winter are found for the rotary wind spectra, the air pressure, air temperature, absolute humidity and bulk transfer fluxes. With the exception of the air pressure (with somewhat higher values in winter than fall) and sea temperature (with peak values in summer), the highest levels of activity occur in the fall; these are usually markedly above the activity found during the summer. The fall seems to be the season when major changes are taking place in the surface layer.

The seasonal spectra of sea temperature (see Fig. 6), in contrast to the spectra of the other quantities, have their largest values in summer and the smallest values in winter. The largest values in the seasonal spectra of sea temperature occur at periods ranging from 10 to 100 days (0.1 to 0.01 cpd). In spring, the largest values are found at periods of 12 to 30 days (0.08 to 0.033 cpd), while the other seasons show the largest spectral values at longer periods. In all cases, the 95% confidence intervals are large indicating a large year to year variability and the fact that the longest-period spectral estimates have the least amount of smoothing.

The diurnal variations of the sea temperature and air temperature are largest in the spring and smallest in the fall and winter.

5 Cross-spectra

Cross-spectral analysis provides information on the relationship of pairs of quantities over the periods resolved. The cross-spectral results are displayed by graphs of the coherence and phase. On the coherence plots, the dashed line represents those coherence values below which there is a 95% probability that a randomly coherent signal will fall (Groves and Hannan, 1968). It should be noted that, for the shorter periods, the numbers of degrees of freedom are so large that it is possible to find statistical significance in coherence estimates that are small (say less than 0.3). Such small coherence estimates, though statistically significant, are of little value in attempting to predict the behavior of one quantity from that of another quantity.

The coherence between the wind speed and the scalar quantities (air pressure, air temperature, sea temperature, and absolute humidity) are generally low as is the rotary coherence between the vector wind and these scalar quantities. As an example, the coherence and phase between the wind speed and air pressure is displayed in Fig. 7. At the annual period, very high coherences occur. In addition, statistically significant levels are found at synoptic scales. However, these levels are too low to be of predictive value. The coherence of the sea temperature with other quantities (air pressure, air temperature and absolute humidity) follows a similar pattern.

As one would expect, the air temperature-absolute humidity cross-spectrum, displayed in Fig. 8, indicates a strong correlation over most scales, as seen from the high coherence levels and small phase values. For periods less than 3 days, the coupling declines sharply although the coherence between the signals does remain statistically significant.

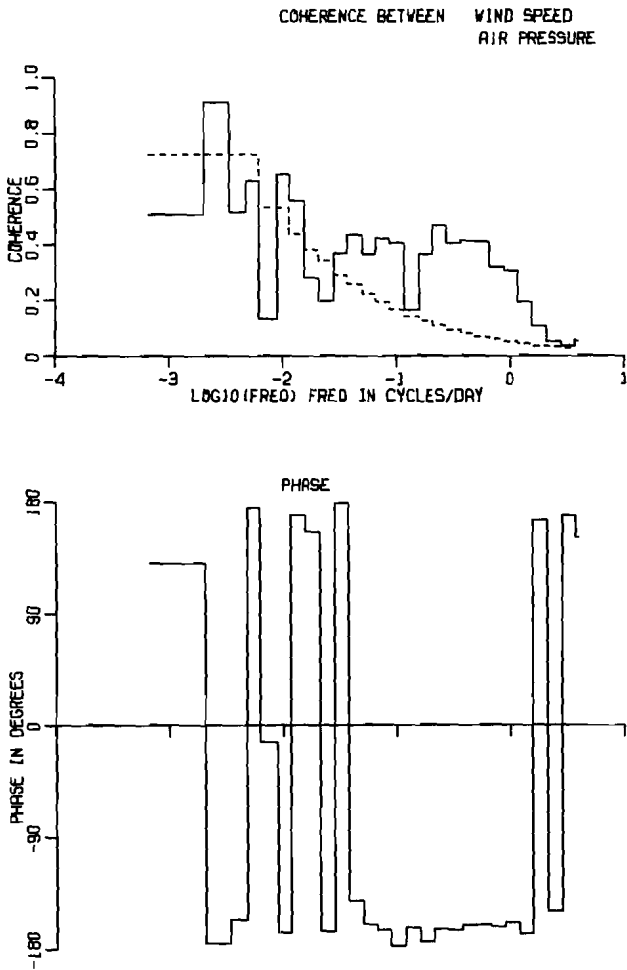


Fig. 7 The phase and coherence between the wind speed and the air pressure.

High levels of coherence are found between the air temperature and absolute humidity with quantities representative of sensible and latent heat fluxes, respectively. For example, Fig. 9 shows the coherence and phase between air temperature and $U\Delta T$, a quantity representative of the sensible heat flux. The cross-spectral results show a very significant and high level of coherence between these quantities at all periods less than or equal to one-half year, largely because the variations in the sea temperature are considerably smaller than those of the air temperature at these periods. At periods longer than one-half year, the coherence levels are poor, with the exception of very good coherence at the annual cycle. Over the synoptic and mesoscale periods, the phase between the two signals is very uniform, remaining within 15 degrees of being exactly out of phase.

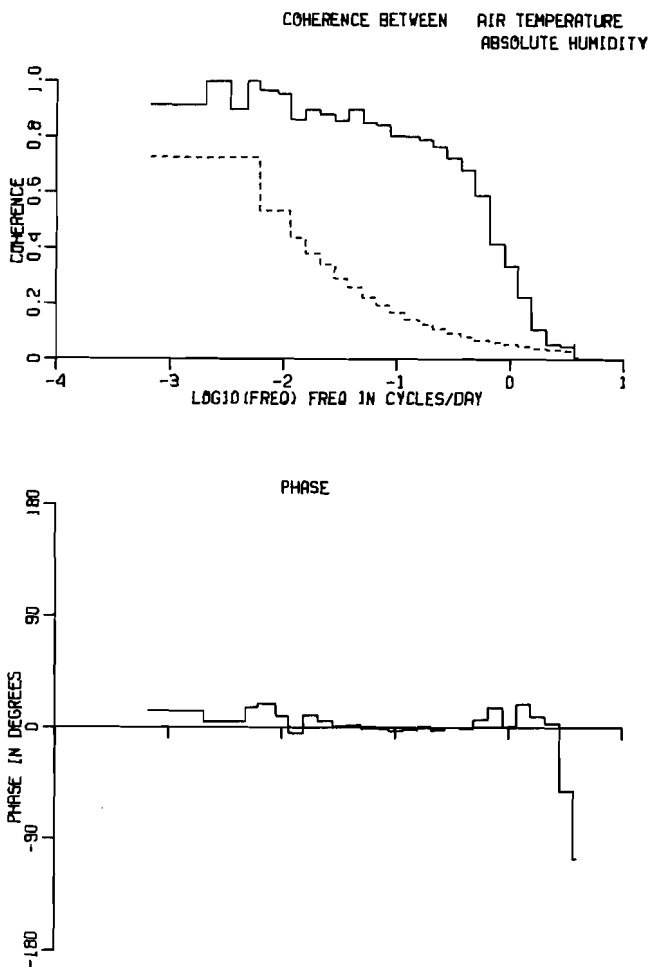


Fig. 8 The phase and coherence between the air temperature and the absolute humidity.

Air temperature shows generally high coherence with humidity and $U\Delta T$; humidity shows high coherence with $U\Delta q$. This suggests that one could make a fair estimate of variations in the total turbulent heat flux simply from the variations in air temperature. The coherence between the air temperature and $1.2 U\Delta T + 2.44 U\Delta q$, which is representative of the total heat flux (see Fig. 10), reveals a coherence of 0.7 or greater over periods ranging from 3 to 180 days (0.33 to 0.0055 cpd).

6 Summary

The spectra of the wind and air pressure at Ocean WeatherShip P are dominated by activity of the synoptic scales. The peak level in the $f\phi$ spectrum of wind speed of 8.2 (m/s)^2 occurs at a period of 3 days. The annual peak is prominent

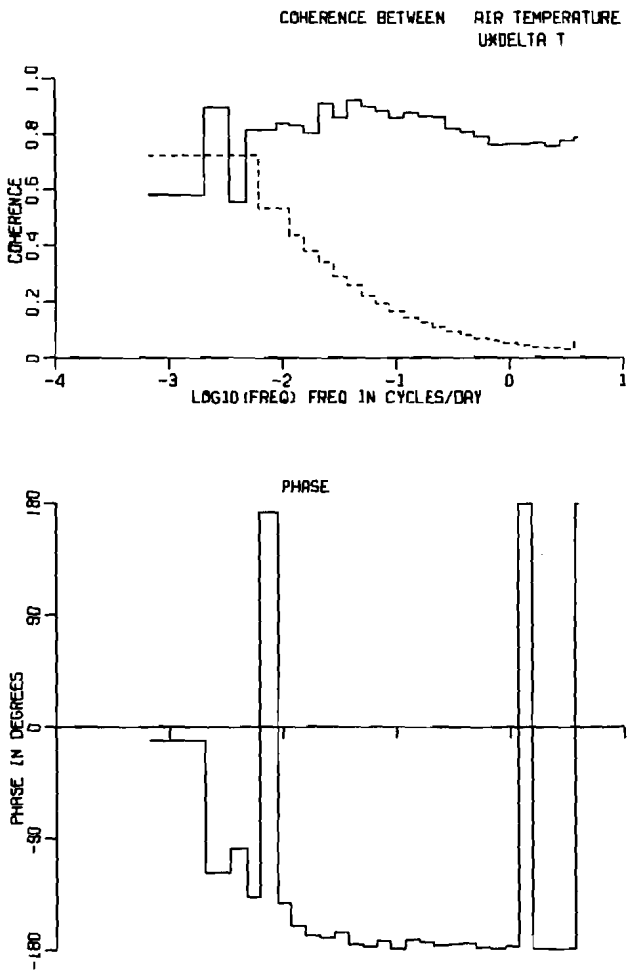


Fig. 9 The phase and coherence between the air temperature and $U\Delta T$, a quantity representative of the sensible heat flux.

while there is no significant diurnal peak. A small but significant amount of activity is present at the semi-diurnal period. Seasonal changes are found in the behavior of the wind speed. The wind speed spectra of the fall and winter feature a larger amplitude synoptic peak centered on shorter periods as compared to the synoptic peak of the spring and summer. A comparison with the wind speed spectra determined by other investigators at various locations, reveals that Ocean Weather Station P is characterized by higher levels of activity occurring at generally shorter periods.

The spectra of sea temperature, air temperature and absolute humidity are dominated by annual and semi-annual variations. A limited amount of activity is found at synoptic scales in the air temperature and absolute humidity

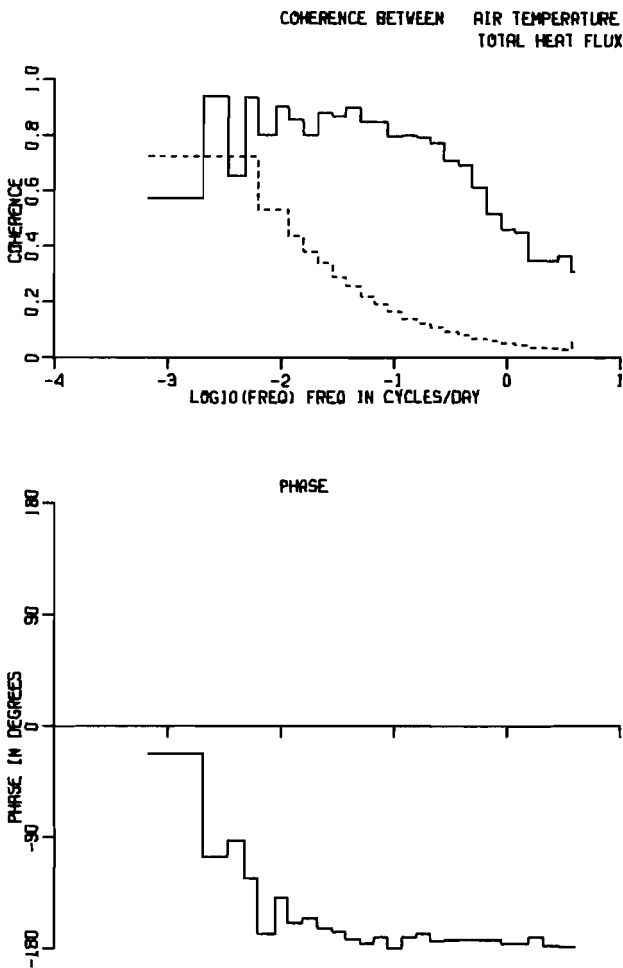


Fig. 10 The phase and coherence between the air temperature and $1.2 U\Delta T + 2.44 U\Delta q$, a quantity representative of the total turbulent heat flux.

spectra. The sea temperature and air temperature have an average diurnal variation of 0.13°C and 0.64°C respectively.

The rotary auto-spectrum of the wind shows peak levels at a period of 3 days. The clockwise side of the spectrum has larger spectral values, apparently a result of the prevailing weather system movements to the north of Station P.

The rotary auto-spectrum of the time series (UU_x, UU_y) , proportional through the bulk aerodynamic parameterization to the wind stress (where U_x and U_y are the eastward and northward wind components, respectively), has the same general characteristics as the rotary auto-spectrum of the wind. The spectra of $U\Delta T$ (representative of sensible heat flux) and $U\Delta q$ (representative of latent heat flux) each show a strong annual peak and a broad synoptic peak that accounts for most of the quantities' variance.

The results of the cross-spectral analysis indicate generally low coherence levels between the wind and other quantities and the sea temperature and other quantities except at annual and synoptic scales. At synoptic scales, while the coherence values are statistically significant, they are generally too low to be useful for predictive purposes.

Higher coherences are found between pairs of the following quantities; air temperature and humidity and quantities representative of heat fluxes. These larger coherences may be useful for some purposes. For example, one could make a fair estimate of variations in the total turbulent heat flux simply from the variations in air temperature, at least for periods of greater than 2 to 3 days.

Acknowledgements

The authors thank the Atmospheric Environment Service of Canada for providing the data and the National Research Council of Canada (grant A8301) and the U.S. Office of Naval Research (Contract N00014-66-C-0047 under Project 083-207) for supplying the computing expenses. We also thank Dr. R.W. Burling of the Institute of Oceanography, University of British Columbia for helpful discussions. One of us (D.F.) received personal support from the National Research Council of Canada.

References

- BURT, W., H. CREW, N. PLUTCHAK and J. DUMON, 1974: Diurnal variations of winds over an upwelling region off Oregon. *Boundary-Layer Meteor.*, **6**, 35-45.
- BYSHEV, V.I. and YU. A. IVANOV, 1969: The time spectra of some characteristics of the atmosphere above the ocean. *Izvestia, Atmos. and Ocean. Phys.*, **5**, 17-28.
- DENMAN, K.L., 1973: A time dependent model of the upper ocean. *J. Phys. Ocean.*, **3**, 173-184.
- DORMAN, C.E., 1974: Analysis of meteorological and oceanographic data from Ocean Station Vessel N (30N 140W). Ph.D. Thesis, Oregon State University. 136 pp.
- FISSEL, D.B., 1975: A frequency analysis of ten years of surface atmospheric data at Ocean Weathership 'Papa'. M.Sc. Thesis, Institute of Oceanography, University of British Columbia. 136 pp.
- FISSEL, D.B. and S. POND, 1976: Computation of surface fluxes from climatological and synoptic data. (in preparation for *Mon. Wea. Rev.*)
- FRYE, D.E., S. POND and W.P. ELLIOTT, 1972: Note on the kinetic energy spectrum of coastal winds. *Mon. Wea. Rev.*, **100**, 671-672.
- GROVES, G.W. and E.J. HANNAN, 1968: Time series regression of sea level on weather. *Rev. of Geophys.*, **6**, 129-174.
- HERTZMAN, O., M. MIYAKE and S. POND, 1974: Ten years of meteorological data at Ocean Station Papa. Manuscript Report No. 29, Institute of Oceanography, University of British Columbia. 46 pp.
- HWANG, H., 1970: Power density spectrum of surface wind speed on Palmyra Island. *Mon. Wea. Rev.*, **98**, 70-74.
- JENKINS, J.M. and D.G. WATTS, 1968: *Spectral Analysis*. Holden-Day, San Francisco. 325 pp.
- MILLARD, R.C., 1971: Wind measurements from buoys; a sampling scheme. *J. Geophys. Res.*, **76**, 5819-5828.
- MOEERS, C.N.K., 1973: A technique for the cross spectrum analysis of pairs of complex-valued time series, with emphasis on properties of polarized components and rotational invariants. *Deep-Sea Res.*, **20**, 1129-1141.

- OORT, A.H. and A. TAYLOR, 1969: On the kinetic energy spectrum near the ground. *Mon. Wea. Rev.*, **97**, 623-636.
- POND, S., G.T. PHELPS, J.E. PAQUIN, G. MCBEAN and R.W. STEWART, 1971: Measurements of the turbulent fluxes of momentum, moisture and sensible heat over the ocean. *J. Atmos. Sci.*, **28**, 901-917.
- POND, S., D.B. FISSEL and C.A. PAULSON, 1974: A note on bulk aerodynamic coefficients for sensible heat and moisture fluxes. *Boundary-Layer Meteor.*, **6**, 333-339.
- ROLL, H.V., 1965: *Physics of the Marine Atmosphere*. Academic Press Inc., New York. 426 pp.
- SINGLETON, RICHARD C., 1969: An algorithm for computing the mixed radix Fast Fourier Transform. *IEEE Transactions on Audio and Electroacoustics*, **17**, 93-103.
- STEWART, R.W., 1974: The air-sea momentum exchange. *Boundary-Layer Meteorology*, **6**, 151-167.
- U.S. NAVY, Chief of Naval Operations (1955 to 1969). Marine climatic atlas of the world. Vol. I to VIII. Washington, D.C. NAVAER 50-1C-528.
- VAN DER HOVEN, I., 1957: Power spectrum of horizontal wind speed in the frequency range from 0.0807 to 900 cycles/hour. *J. Meteor.*, **14**, 160-164.

CANADIAN WORKSHOP ON WIND ENGINEERING

Toronto, Ontario

September 23 and 24, 1976

This workshop will bring together Canadian workers, both researchers and users of information, who are interested in some aspect of Wind Engineering. The field of wind engineering is concerned with the interactions between the wind and objects or fluids subjected to it at altitudes below about 1000 metres. It is planned to have workers in this field meet to discuss areas which are presently receiving attention and to identify those which are in need of future study. It is intended that users and producers of information will engage in frank and open discussion of their mutual needs and desires for the purpose of attaining common goals.

The workshop will also provide a forum for discussion of the need for and possible structure of a formalized Canadian committee on wind engineering. Such a committee would serve to coordinate wind engineering activities in Canada and would communicate formally with the recently created International Association of Wind Engineering.

A session will be held to discuss each of the following major problem areas:

BUILDINGS AND STRUCTURES	POLLUTANT DISPERSAL
WIND-BLOWN PARTICLES	TRANSMISSION LINES
STREET-LEVEL WINDS	WIND ENERGY
METEOROLOGICAL DATA	AIRCRAFT/SURFACE VEHICLES

Additional information may be obtained by telephoning or writing the organizing secretary:

Dr. H.W. Teunissen
 Atmospheric Environment Service
 4905 Dufferin Street
 Downsview, Ontario M3H 5T4
 Telephone: (416) 667-4910

announcements continued on p. 144

Short-Term Forecasting with a Multi-Level Spectral Primitive Equation Model Part I – Model Formulation

Roger Daley, Claude Girard and John Henderson
Atmospheric Environment Service, Montreal, Quebec

and

Ian Simmonds
*Geophysical Fluid Dynamics Program/NOAA
Princeton University, Princeton, N.J., 08540. U.S.A.*

[Manuscript received 12 November 1975; in revised form 24 February 1976]

ABSTRACT

A global baroclinic primitive equation model using the spectral technique has been constructed for short- and medium-range numerical weather prediction. The spectral technique, which is a special case of the Galerkin method, employs spherical harmonic basis functions in the evaluation of all horizontal derivatives. The use of a transform technique allows all the

horizontal operations to be performed efficiently and allows physical processes to be evaluated in real space. The model employs a semi-implicit algorithm for time integration and finite differencing in the vertical. Physical processes include orography, moist convection, large scale precipitation and boundary layer processes.

1 Introduction

In recent years there has been increasing interest in the Galerkin method for use in numerical weather prediction. In this method, the dependent variables of the problem are expanded in a truncated series of linearly independent basis functions. The Galerkin procedure requires that the error caused by the truncation of this series be made orthogonal to the basis functions of the truncated expansion. Two variants of this method are used in meteorology. The first is the finite-element method in which the basis functions are piecewise-continuous functions of compact support. The second is the spectral method in which the basis functions are non-local continuously differentiable functions, which are usually the solutions of a relevant eigenvalue problem.

The history of the spectral method in meteorology goes back to Blinova (1943) and Silberman (1954). For large-scale numerical weather prediction over the globe, the basis functions employed have usually been spherical harmonic functions, although Hough functions (Flattery, 1970) and trigonometric functions (Robert, 1966; Orszag, 1974) have also been proposed. Spherical harmonics have the useful properties that they are mutually orthogonal, and that a

variable expanded in a properly truncated series of these functions is invariant under rotation of the coordinate system. This last fact implies that the pole problem, which occurs in most finite-difference global models, does not exist in a global spectral model based on spherical harmonics: Because of the Galerkin formulation, the unresolvable scales are not misrepresented in terms of the scales resolved and thus, there is no aliasing. Another advantage of the spectral formulation is that more information is carried per degree of freedom than in a grid-point model, minimizing computer storage.

Despite these advantages, the spectral method has not been practical for operational use because of the enormous amount of computation required in the calculation of non-linear terms. However, Eliassen *et al.* (1970) and Orszag (1970) independently developed the transform method in which the real-space forms of the dependent variables are evaluated from the spectral coefficients for the calculation of non-linear terms, and the results transformed back to spectral space, every timestep. This formulation has the additional advantage that physical processes can be easily parameterized using the real-space form of the dependent variables on the transform grid.

The transform technique (also known as collocation) was first tested on the free-surface equations by Eliassen *et al.* (1970) and by Bourke (1972). Later Machenhauer and Daley (1972) extended the technique to the full primitive equations using a vertical spectral representation. In contrast to this fully Galerkin approach, Bourke (1974) extended his free-surface formulation to the full primitive equations using finite differencing in the vertical.

The discovery of the transform technique has, at last, made possible an operational spectral forecast model. The present work is an attempt to formulate an efficient spectral model able to compete with conventional methods in short- and medium-range forecasting.

The model is a multi-level global primitive equation model using sigma coordinates (Phillips, 1957). In the horizontal, all dependent variables are expanded in a truncated series of spherical harmonic functions and a transform technique similar to that of Bourke (1972) is used. As in Bourke (1974) vertical operations are handled by finite differencing. However, a quite different vertical discretization is assumed, to be compatible with the semi-implicit time integration scheme of Robert *et al.* (1972). The model simulates several physical effects including precipitation and latent heat release, the earth's surface topography, transport of heat and moisture from the oceans, small-scale convection and boundary-layer stresses.

Part II¹ of this paper will discuss the results of a year of day-to-day forecasting with this model. It will be demonstrated that spectral models do indeed have operational capabilities. In addition, forecasts made with a grid-point multi-level primitive equation model, having vertical structure, semi-implicit algorithm and physical parameterizations similar to the spectral model, will provide a useful basis for comparison.

¹This issue

2 Governing equations

The model is developed in sigma coordinates in the form $\sigma = p/p_s$, where p is the pressure and p_s the surface pressure. Thus $\sigma = 0$ at the top of the atmosphere and $\sigma = 1$ at the earth's surface. We will employ the usual boundary conditions $\dot{\sigma} = 0$ at $\sigma = 1$ and $\sigma = 0$.

It is convenient to define the following operators before developing the governing equations:

$$\hat{F}^\sigma = \int_\sigma^1 F d\sigma, \quad \hat{F} = \int_0^1 F d\sigma. \quad (1)$$

The equations of motion are written in differentiated form and the other equations are the thermodynamic equation, continuity equation, hydrostatic equation and a moisture equation, as follows:

$$\frac{\partial \zeta}{\partial t} = -\nabla \cdot (\zeta + f) \mathbf{V} - \mathbf{k} \cdot \nabla \times \left(RT \nabla q + \dot{\sigma} \frac{\partial \mathbf{V}}{\partial \sigma} - \mathbf{F} \right), \quad (2)$$

$$\begin{aligned} \frac{\partial D}{\partial t} = \mathbf{k} \cdot \nabla \times (\zeta + f) \mathbf{V} - \nabla \cdot \left(RT \nabla q + \dot{\sigma} \frac{\partial \mathbf{V}}{\partial \sigma} - \mathbf{F} \right) \\ - \nabla^2 \left(\Phi + \frac{\mathbf{V} \cdot \mathbf{V}}{2} \right), \end{aligned} \quad (3)$$

$$\frac{\partial T}{\partial t} = -\nabla \cdot \mathbf{V} T + TD + \dot{\sigma} \gamma - \frac{RT}{C_p} \left(D + \frac{\partial \dot{\sigma}}{\partial \sigma} \right) + H_T, \quad (4)$$

$$\frac{\partial q}{\partial t} = -D - \frac{\partial \dot{\sigma}}{\partial \sigma} - \mathbf{V} \cdot \nabla q, \quad (5)$$

$$\sigma \frac{\partial \Phi}{\partial \sigma} = -RT \quad (6)$$

and

$$\begin{aligned} \frac{\partial S}{\partial t} = -\nabla \cdot \mathbf{V} S + SD - \dot{\sigma} \frac{\partial S}{\partial \sigma} + H_T - H_M \\ - \left[\frac{RT}{C_p} - \frac{RT_d^2}{\epsilon L(T_d)} \right] \left[D + \frac{\partial \dot{\sigma}}{\partial \sigma} - \frac{\dot{\sigma}}{\sigma} \right], \end{aligned} \quad (7)$$

where

f = Coriolis parameter,

\mathbf{V} = horizontal vector wind,

ζ = vertical component of vorticity = $\mathbf{k} \cdot \nabla \times \mathbf{V}$,

D = horizontal divergence = $\nabla \cdot \mathbf{V}$,

T is the absolute temperature,

$q = \ln p_s$,

$$\gamma = \text{static stability} = \frac{RT}{C_p \sigma} - \frac{\partial T}{\partial \sigma}, \quad (8)$$

σ = vertical motion in sigma coordinates

$$= (\sigma - 1) \left(\hat{D} + \hat{\mathbf{V}} \cdot \nabla q \right) + \hat{D}^\sigma + \hat{\mathbf{V}}^\sigma \cdot \nabla q \quad (9)$$

- Φ = geopotential height,
 F is the horizontal frictional force per unit mass,
 H_T is the diabatic heating,
 R is the gas constant for dry air,
 C_p is the specific heat of dry air at constant pressure,
 T_d is the dewpoint temperature,
 $S = T - T_d$ is the dewpoint depression,
 ϵ is the ratio of the molecular weight of water vapour to effective molecular weight of dry air (0.622),
 $L(T_d)$ is the latent heat of vaporization of water or ice,
 H_M represents moisture sources or sinks.

The derivation of equation (7) will be discussed in some detail in Section 6.

The governing equations are next transformed to spherical coordinates. Following Robert (1966) the horizontal wind components u and v are converted into true scalars $U = u \cos \theta/a$ and $V = v \cos \theta/a$, where a is the radius of the earth, u is the zonal wind component, v is the meridional wind component, θ is the latitude and λ , the longitude.

In order to simplify the spherical coordinate form of the governing equations we define \bar{F}^{-H} to be the horizontal mean of F .

$$\bar{F}^{-H} = \frac{1}{4\pi} \int_{-\pi/2}^{\pi/2} \int_0^{2\pi} F(\lambda, \theta, \sigma, t) \cos \theta d\lambda d\theta$$

We decompose the temperature field into its initial horizontal mean and a deviation. Thus $T = T^* + T'$ where $T^* = \bar{T}^{-H}(\sigma, t = 0)$. In a similar way $\gamma = \gamma^* + \gamma'$. The following operator will also be useful:

$$\alpha(A, B) = \frac{1}{\cos^2 \theta} \left[\frac{\partial A}{\partial \lambda} + \cos \theta \frac{\partial B}{\partial \theta} \right]. \quad (10)$$

With these definitions the governing equations become

$$\frac{\partial \zeta}{\partial t} = -\alpha(A, B), \quad (11)$$

$$\frac{\partial D}{\partial t} + \nabla^2(\Phi + RT^*q) = \alpha(B, -A) - a^2 \nabla^2 E, \quad (12)$$

$$\frac{\partial T}{\partial t} - \gamma^* \dot{\sigma} - \frac{RT^*}{C_p} \frac{\partial q}{\partial t} = -\alpha(UT', VT') + B_T, \quad (13)$$

$$\frac{\partial q}{\partial t} + \hat{G} + \hat{D} = 0, \quad (14)$$

$$\frac{\partial S}{\partial t} = -\alpha(US, VS) + B_S \quad (15)$$

and the hydrostatic equation is unchanged. Here,

$$A = (\zeta + f)U + \dot{\sigma} \frac{\partial V}{\partial \sigma} + \frac{RT'}{a^2} \cos \theta \frac{\partial q}{\partial \theta} - \cos \theta \frac{F_\theta}{a}, \quad (16)$$

$$B = (\zeta + f)V - \dot{\sigma} \frac{\partial U}{\partial \sigma} - \frac{RT'}{a^2} \frac{\partial q}{\partial \lambda} + \cos \theta \frac{F_\lambda}{a}, \quad (17)$$

$$G = \frac{1}{\cos^2 \theta} \left[U \frac{\partial q}{\partial \lambda} + V \cos \theta \frac{\partial q}{\partial \theta} \right], \quad (18)$$

$$E = \frac{(U^2 + V^2)}{2 \cos^2 \theta}, \quad (19)$$

$$\dot{\sigma} = (\sigma - 1)(\hat{G} + \hat{D}) + \hat{G}^\sigma + \hat{D}^\sigma, \quad (20)$$

$$B_T = T'D + \gamma' \dot{\sigma} - \frac{RT'}{C_p} (\hat{G} + \hat{D}) + \frac{RT}{C_p} G + H_T, \quad (21)$$

$$B_S = SD - \dot{\sigma} \frac{\partial S}{\partial \sigma} + \left[\frac{RT}{C_p} - \frac{RT_d^2}{\epsilon L(T_d)} \right] \left[\frac{\dot{\sigma}}{\sigma} + G - \hat{G} - \hat{D} \right] + H_T - H_M \quad (22)$$

and ∇^2 is the horizontal Laplacian operator in spherical coordinates.

We have transferred some of the terms to the left-hand side in equations (12), (13) and (14). These terms will be treated implicitly when the semi-implicit algorithm is introduced. Following Robert *et al.* (1972) we introduce the following two definitions which will be useful in the semi-implicit formulation:

$$P = \Phi + RT^*q \quad (23)$$

and

$$W = \dot{\sigma} - \sigma(\hat{G} + \hat{D})$$

We also define $W_s \equiv W(\sigma = 1) = -(\hat{G} + \hat{D})$. Substituting these new variables into the left-hand side of the divergence, thermodynamic and continuity equations, we find

$$\frac{\partial D}{\partial t} + \nabla^2 P = \alpha(B, -A) - a^2 \nabla^2 E, \quad (24)$$

$$\sigma \frac{\partial^2 P}{\partial t \partial \sigma} + R\gamma^*W = R\alpha(UT', VT') - RB_T \quad (25)$$

and

$$\frac{\partial q}{\partial t} - W_s = 0. \quad (26)$$

We now have one more variable than equations and we therefore generate an equation for W from the definitions of $\dot{\sigma}$ and W .

$$\frac{\partial W}{\partial \sigma} + D = B_w \quad \text{where} \quad B_w = -G \quad (27)$$

3 Spectral form of the governing equations

The spectral form of the governing equations is developed in a manner analogous to that of Machenhauer and Daley (1972) and, more specifically, Bourke (1974). The vorticity ζ , for example, is expanded in the following truncated series of spherical harmonics:

$$\zeta = \sum_{m=-J}^J \sum_{l=|m|}^{|m|+J} \zeta_l^m Y_l^m, \quad (28)$$

where ζ_l^m are complex expansion coefficients, functions of σ and t .

$Y_l^m(\lambda, \theta) = X_l^m(\sin \theta)e^{im\lambda}$ are the spherical harmonics.

$X_l^m(\sin \theta)$ are associated Legendre functions of the first kind of order m .

m is the east-west (zonal) wavenumber.

l is the degree of the associated Legendre function.

J denotes the rhomboidal wavenumber truncation (Ellsaesser, 1966).

The condition $(\zeta_l^m)^c = (-1)^m \zeta_l^{-m}$ where $(^c)$ indicates complex conjugation, ensures reality of the representation. The spherical harmonics satisfy the following orthonormality condition:

$$\overline{Y_l^m Y_j^n}^H = \frac{1}{2} \delta_j^l \delta_m^n, \quad (29)$$

where δ_j^l is the Kronecker delta.

D, T, P, Φ, S and W are expanded in the same manner as equation (28). The variable q is similarly expanded except that the q_l^m are functions of time only. In the expansions for U and V there is one extra component for each m , in order to be consistent with the expansions for ζ and D (Eliassen *et al.* 1970).

$$U = \sum_{m=-J}^J \sum_{l=|m|}^{|m|+J+1} U_l^m Y_l^m, \quad V = \sum_{m=-J}^J \sum_{l=|m|}^{|m|+J+1} V_l^m Y_l^m \quad (30)$$

Diagnostic relations between U, V and D, ζ can be obtained as in Eliassen *et al.* (1970). Helmholtz's theorem states that an arbitrary wind field can be represented as the sum of the gradient of a potential function and the curl of a stream function. Using the properties of spherical harmonics, it can be shown that:

$$l(l+1)U_l^m = -(l+1)\epsilon_l^m \zeta_{l-1}^m + l\epsilon_{l+1}^m \zeta_{l+1}^m - imD_l^m \quad (31)$$

and

$$l(l+1)V_l^m = +(l+1)\epsilon_l^m D_{l-1}^m - l\epsilon_{l+1}^m D_{l+1}^m - im\zeta_l^m \quad (32)$$

where

$$\epsilon_l^m = \sqrt{(l^2 - m^2)/(4l^2 - 1)} \quad (33)$$

and $U_0^0 = \epsilon_1^0 \zeta_1^0, V_0^0 = -\epsilon_1^0 D_1^0$ are special cases. Other diagnostic relationships involving P, Φ, T and q can be obtained from the hydrostatic equation (6):

$$T_l^m = -\frac{\sigma}{R} \frac{\partial P_l^m}{\partial \sigma} + \sigma \frac{\partial T^*}{\partial \sigma} q_l^m \quad (34)$$

and

$$T_l^m = -\frac{\sigma}{R} \frac{\partial \Phi_l^m}{\partial \sigma}. \quad (35)$$

The history-carrying variables are ζ_l^m , D_l^m , P_l^m , S_l^m and q_l^m . The variables T_l^m , Φ_l^m , U_l^m , V_l^m are all related to the history-carrying variables by the preceding diagnostic relations. The variable W_l^m is only carried for formal reasons; it will eventually be eliminated when the semi-implicit algorithm is derived in the next section.

To simplify the notation, we introduce the following operator:

$$\{F\}_l^m = \frac{1}{2\pi} \int_{-\pi/2}^{\pi/2} \int_0^{2\pi} F(\lambda, \theta, \sigma, t) Y_l^c(\lambda, \theta) \cos \theta d\lambda d\theta. \quad (36)$$

With this definition, the spectral form of the governing equations become, for all m, l :

$$\frac{\partial \zeta_l^m}{\partial t} = -\{\alpha(A, B)\}_l^m, \quad (37)$$

$$\frac{\partial D_l^m}{\partial t} - a^{-2}l(l+1)P_l^m = \{\alpha(B, -A) - a^2 \nabla^2 E\}_l^m, \quad (38)$$

$$\sigma \frac{\partial^2 P_l^m}{\partial \sigma \partial t} + R\gamma^* W_l^m = R\{\alpha(UT', VT') - B_T\}_l^m, \quad (39)$$

$$\frac{\partial W_l^m}{\partial \sigma} + D_l^m = \{B_w\}_l^m, \quad (40)$$

$$\frac{\partial q_l^m}{\partial t} - W_s{}_l^m = 0, \quad (41)$$

$$\frac{\partial S_l^m}{\partial t} = \{-\alpha(US, VS) + B_s\}_l^m. \quad (42)$$

Integrals on the right-hand side of equations (37) to (42) all fall into one of three categories, typified by

$$\{B_T\}_l^m = \frac{1}{2\pi} \int_{-\pi/2}^{\pi/2} \int_0^{2\pi} B_T Y_l^c \cos \theta d\lambda d\theta, \quad (43)$$

$$\{a^2 \nabla^2 E\}_l^m = -\frac{l(l+1)}{2\pi} \int_{-\pi/2}^{\pi/2} \int_0^{2\pi} \frac{U^2 + V^2}{2 \cos \theta} Y_l^c d\lambda d\theta, \quad (44)$$

and

$$\{\alpha(A, B)\}_l^m = \frac{1}{2\pi} \int_{-\pi/2}^{\pi/2} \int_0^{2\pi} \frac{1}{\cos \theta} \left[\frac{\partial A}{\partial \lambda} + \cos \theta \frac{\partial B}{\partial \theta} \right] Y_l^c d\lambda d\theta, \quad (45)$$

Now B_T , E , A , B and $\alpha(A, B)$ are all nonlinear expressions. The integrals of type (43), (44) and (45) are calculated using the methods of Eliassen *et al.* (1970) and Orszag (1970). That is, all variables (ζ , D , U , V , T , S , $\partial q/\partial \lambda$ and $\cos \theta \partial q/\partial \theta$) required in the calculation of the right-hand sides of equations (37) to (42) are

first synthesized onto the real-space transform grid. From the real-space form of the variables, the non-linear expressions A , B , E , $T'U$, $T'V$, SU , SV , B_T , B_W and B_S can be calculated. The integrals on the right-hand sides of equations (37) to (42) are then simply calculated by exact numerical quadrature. Integrals of type (43) and (44) are straightforward, but integrals of type (45) employ an integration by parts in the manner of Bourke (1972). Thus if

$$A = \sum_{m=-J}^J A_m e^{im\lambda} \quad \text{and} \quad B = \sum_{m=-J}^J B_m e^{im\lambda}$$

then

$$\{\alpha(A, B)\}_l^m = \int_{-\pi/2}^{\pi/2} \left[imA_m X_l^m - B_m \cos \theta \frac{\partial X_l^m}{\partial \theta} \right] \frac{d\theta}{\cos \theta} \quad (46)$$

The transform grid consists of equally spaced longitudes and almost-equally-spaced Gaussian latitudes. In the synthesis from spectral to grid, an associated Legendre transform is first performed at each Gaussian latitude circle, to produce Fourier coefficients. A discrete Fourier transform is then performed to produce functional values at each longitude of the transform grid. After the non-linear calculations are carried out on the grid, the integrals on the right-hand sides of equations (37) to (42) are calculated by first performing a discrete inverse Fourier transform at each Gaussian latitude. The final step is the inverse associated Legendre transform performed by Gaussian quadrature. In all cases, the contributions to the integrals are accumulated successively at each Gaussian latitude in the manner of Eliassen *et al.* (1970). This successive accumulation procedure has the advantage that storage at any time is only required for a single Gaussian latitude of grid point information. It is this procedure, together with the fact that each spectral degree of freedom carries more information than its finite-difference counterpart, that makes the spectral model so efficient with respect to storage requirements.

All numerical quadratures are performed exactly with respect to linear or quadratic terms. This is ensured by requiring that the transform grid contains $\geq (5J + 1)/2$ Gaussian latitudes and $\geq 3J + 1$ longitudes for a global integration. Triple products such as $\gamma\delta$ are not performed alias-free, but this aliasing seems to be acceptable (Bourke, 1974). In the same manner, any physical parameterizations which are not linear or quadratic in nature are also aliased.

In fig. 1 is plotted the rhomboidal truncation used in the model as a function of the zonal wavenumber m and the two-dimensional wavenumber l . The diagram represents the case $J = 10$, although in practice the resolution of the model would be considerably higher, lying between 15 and 30.

If it is desired to integrate the model over only one hemisphere, considerable savings of computer time and storage space can be made. Spherical harmonics are either symmetric or antisymmetric with respect to the equator. In the case of a hemispheric model, only symmetric modes are used for the expansion of D , P , S , T , q , Φ , W and U , while only antisymmetric modes are used for ζ and V . The governing equations imply that the other modes, if initially zero, will

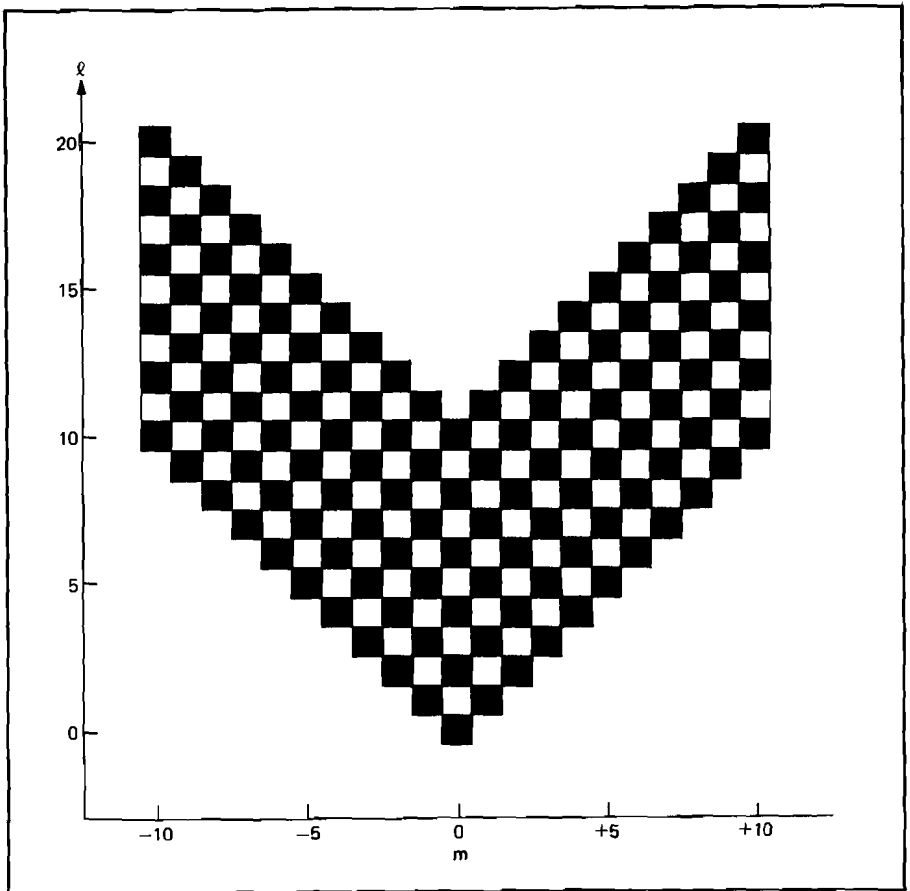


Fig. 1 Schematic representation of the spherical harmonic modes included in the rhomboidal truncation $J = 10$. The ordinate is the two-dimensional wavenumber l . The abscissa is the zonal (east-west) wavenumber. Black squares indicate symmetric modes, white squares anti-symmetric modes.

remain zero. The above choice of symmetric and antisymmetric modes is equivalent to specifying that the north-south wind and the north-south derivatives of U , Φ etc. vanish at the equator, i.e. a free-slip wall condition. The model is designed to utilize and store only the non-zero components, which makes hemispheric integrations particularly efficient.

Some authors, notably Baer (1972), have suggested the use of triangular truncation. In this case, if L denotes the triangular wavenumber truncation then all modes would have to satisfy $-L \leq m \leq L$, $l \leq L$. In fig. 1, this would give a triangular shape, rather than a double rhomboid. There are some advantages to the triangular truncation, particularly in the calculation of energetics and energy spectra. However, the superiority of the triangular truncation with respect to the integration of a complicated numerical model has never been demonstrated. Moreover, the rhomboidal truncation is much simpler to code,

particularly if it is desired to take full advantage of the symmetries in integrating a hemispheric model.

4 The semi-implicit algorithm

The semi-implicit formulation follows Robert *et al.* (1972). In equations (37) to (42), time derivatives are replaced by centered time differences (except at initial time where forward differences are applied), i.e. $\partial F/\partial t$ is approximated by $[F(t + \Delta t) - F(t - \Delta t)]/2\Delta t$ where Δt is the timestep. The remaining terms on the left-hand sides are handled implicitly by the application of the time averaging operator ($\overline{\quad}^t$) defined by $\overline{F}^t = 1/2[F(t + \Delta t) + F(t - \Delta t)]$, while the right-hand-sides are calculated explicitly.

Two equations remain fully explicit. They are the vorticity and moisture equations:

$$\zeta_i^m(t + \Delta t) = -2\Delta t\{\alpha(A, B)\}_i^m + \zeta_i^m(t - \Delta t) \quad (47)$$

and

$$S_i^m(t + \Delta t) = 2\Delta t\{-\alpha(US, VS) + B_s\}_i^m + S_i^m(t - \Delta t). \quad (48)$$

The remaining equations are handled in a semi-implicit manner using the ($\overline{\quad}^t$) operator:

$$\overline{D_i^m}^t - a^{-2}\Delta t l(l+1)\overline{P_i^m}^t = \Delta t\{\alpha(B, -A) - a^2\nabla^2 E\}_i^m + D_i^m(t - \Delta t), \quad (49)$$

$$\sigma \frac{\partial \overline{P_i^m}^t}{\partial \sigma} + \Delta t R \gamma^* \overline{W_i^m}^t = \Delta t R \{\alpha(UT', VT') - B_T\}_i^m + \sigma \frac{\partial P_i^m}{\partial \sigma}(t - \Delta t), \quad (50)$$

$$\overline{q_i^m}^t - \Delta t \overline{W_{s_i}^m}^t = q_i^m(t - \Delta t) \quad (51)$$

and

$$\frac{\partial \overline{W_i^m}^t}{\partial \sigma} + \overline{D_i^m}^t = \{B_w\}_i^m. \quad (52)$$

The integrals on the right hand side are all evaluated at time t . Some of the terms in the integrals are forcing terms and should really be calculated at time $t - \Delta t$ to avoid the growth of a computational mode. In the case of non-linear forcing terms this would necessitate the transform from spectral to real space of many $t - \Delta t$ variables. This is undesirable from the point of view of computational efficiency, so we have chosen to calculate certain forcing terms at time t and suppress the computational mode with a very weak time filter (Asselin, 1972).

In the manner of Robert *et al.* (1972), $\overline{D_i^m}^t$ is eliminated between equations (49) and (52). Then $\overline{W_i^m}^t$ is eliminated between the resulting equation and equation (50) giving a diagnostic equation for $\overline{P_i^m}^t$

$$\frac{\partial}{\partial \sigma} \sigma \frac{\partial \overline{P_i^m}^t}{\partial \sigma} - \frac{R\Delta t^2}{a^2} l(l+1)\overline{P_i^m}^t = \frac{\partial}{\partial \sigma} \left\{ \frac{C_T}{\gamma^*} \right\}_i^m + \{C_D\}_i^m, \quad (53)$$

where

$$\{C_T\}_l^m = R\Delta t\{\alpha(UT', VT') - B_T\}_l^m + \sigma \frac{\partial}{\partial \sigma} P_l^m(t - \Delta t) \quad (54)$$

and

$$\{C_D\}_l^m = -R\Delta t\{B_w - \Delta t\alpha(B, -A) + a^2\Delta t\nabla^2 E\}_l^m + R\Delta t D_l^m(t - \Delta t). \quad (55)$$

Thus, equations (49) to (52) have been reduced to a two-point boundary value problem for each horizontal mode. If $\{C_T\}_l^m$ and $\{C_D\}_l^m$ are known at time t , the \overline{P}_l^m can be calculated for each m, l provided the boundary conditions at $\sigma = 0$ and $\sigma = 1$ are given. The remaining variables $\overline{D}_l^m, \overline{W}_l^m, \overline{W}_s^m, \overline{q}_l^m$ can be calculated by back substitution into (49) to (52) and the same variables at $t + \Delta t$ can then be calculated from the definition of the $(^{-t})$ operator. Discussion of the appropriate boundary condition for the solution of equation (53) will be delayed until the vertical discretization has been introduced in the next section.

It is appropriate at this time to comment briefly upon the semi-implicit algorithm just derived, since it might appear that certain non-linear terms are being handled implicitly. Thus, at first sight, it appears that the non-linear term G is being included on the left-hand (implicit) side of equation (25) because of the definition for W given in equation (23). This is not so, as was pointed out by Asselin (1975), because the equation for W that is actually used in the model is equation (27), in which the non-linear term G is on the right-hand (explicit) side. Thus, the introduction of the variable W does not allow the implicit treatment of some non-linear terms, but it is very convenient, as will be demonstrated subsequently.

5 Vertical discretization

The vertical finite-difference scheme is a somewhat more general form of the scheme used by Robert *et al.* (1972). The basic feature of the scheme is that the temperatures are carried at levels intermediate to the levels of the geopotentials. We will dwell principally on the finite-difference analogues to the left-hand sides of equations (49)–(53). The vertical finite-differencing involved in the right-hand-sides of these equations is conventional and will not be discussed at length. It should be stated, though, that logarithmic vertical differencing has generally been used, particularly with respect to the thermodynamic variables. To simplify the notation, the subscript l and superscript m will be understood. Thus, F_l^m is written as F , and $\{F\}_l^m$ is written as $\{F\}$.

We define N as the number of levels in the model. These levels can be specified completely arbitrarily. In the case where the levels are to be equally spaced in σ , they are defined as $\sigma = \sigma_n \equiv (2n - 1)/2N, 1 \leq n \leq N$. On these levels are calculated U, V, ζ, D, Φ and P . The vorticity equation (47), divergence equation (49) and equation (52) are applied at these levels. For convenience we

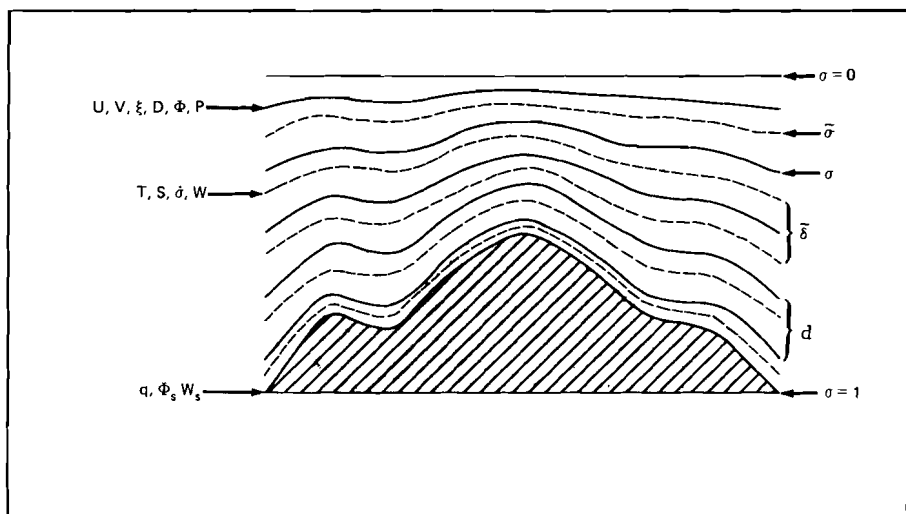


Fig. 2 Schematic representation of the vertical structure of the model ($N = 5$, equally spaced in σ). The solid lines represent the levels σ_n , $1 \leq n \leq N$. The dashed lines represent the layers $\tilde{\sigma}_n$, $1 \leq n \leq N$. The level increments d and layer increments $\tilde{\delta}$ are also illustrated.

will define $\sigma_{N+1} = 1$, where we carry q , Φ_s (the surface topography) and W_s . In the case of an equally-spaced 5-level model (illustrated in figure 2) $\sigma_1 = 0.1$, $\sigma_2 = 0.3$, $\sigma_3 = 0.5$, $\sigma_4 = 0.7$, $\sigma_5 = 0.9$ and $\sigma_6 = 1.0$.

As mentioned earlier, the thermodynamic equation is applied at intermediate levels. These levels are obtained from a finite difference form of the hydrostatic equation. The following finite-difference approximation to the hydrostatic equation (34) is second-order accurate, provided that the layer temperatures \tilde{T}_n are defined at the geometric mean of the adjacent σ -level values, i.e. by

$$\tilde{T}_n = (\Phi_n - \Phi_{n+1})/Rd_n, \quad 1 \leq n \leq N, \quad (56)$$

where

$$\Phi_n = \Phi(\sigma = \sigma_n), \quad d_n = \ln(\sigma_{n+1}/\sigma_n).$$

We will hereinafter refer to the σ -values where the thermodynamic equation is applied as the layer values. They are thus defined as $\tilde{\sigma}_n = \sqrt{\sigma_n \sigma_{n+1}}$. The tilde (\sim) notation will be used to indicate which variables are carried in the layers ($\sigma = \tilde{\sigma}_n$); these are \tilde{T}_n , \tilde{S}_n and \tilde{W}_n . Note that \tilde{W}_N is not carried; instead we use W_s which is applied at a level $\sigma_{N+1} = 1$ and therefore appears without a tilde. For an equally-spaced 5-level model the layer values of σ are $\tilde{\sigma}_1 = 0.173$, $\tilde{\sigma}_2 = 0.387$, $\tilde{\sigma}_3 = 0.592$, $\tilde{\sigma}_4 = 0.794$, $\tilde{\sigma}_5 = 0.949$.

It is convenient to define vertical increments in σ ; i.e., $\tilde{\delta}_n = \tilde{\sigma}_{n+1} - \tilde{\sigma}_n$, $1 \leq n \leq N - 2$. Both the top and bottom increments are special cases. Thus $\tilde{\delta}_0 = \tilde{\sigma}_1$ and $\tilde{\delta}_{N-1} = 1 - \tilde{\sigma}_{N-1}$.

Now $P_n = \Phi_n + RT_n^*q$ is defined on the levels σ_n , whereas the temperatures

\tilde{T}_n and thus \tilde{T}_n^* are carried in the layers $\tilde{\sigma}_n$. We obtain T_n^* and thus P_n from \tilde{T}_n^* and q by simply taking the logarithmic average of the adjacent layer temperatures \tilde{T}_n^* and \tilde{T}_{n+1}^* . To second order accuracy

$$T_n^* = (d_{n-1}\tilde{T}_n^* + d_n\tilde{T}_{n-1}^*)/(d_n + d_{n-1}), \quad 2 \leq n \leq N. \quad (57)$$

T_1^* cannot be calculated in this manner and is instead simply obtained by linear extrapolation.

$$T_1^* = 1.5\tilde{T}_1^* - .5T_2^*.$$

The T'_n are obtained in a similar manner.

The static stability γ^* can be calculated at the layers $\tilde{\sigma}_n$ simply as

$$\tilde{\gamma}_n^* = \frac{1}{\tilde{\sigma}_n} \left(\frac{R\tilde{T}_n^*}{C_p} - \frac{T_{n+1}^* - T_n^*}{d_n} \right), \quad 1 \leq n \leq N \quad (58)$$

where $T_{N+1}^* = T_s^*$. In the absence of an equation for T_s , it has been assumed that $\tilde{\gamma}_N^* = \tilde{\gamma}_{N-1}^*$. This, in effect, formally defines T_s^* in terms of \tilde{T}_N^* and T_N^* . A similar expression and assumption is used to relate $\tilde{\gamma}'_n$ to \tilde{T}'_n , T'_n and T'_{n+1} .

Vertically discretized analogues of the vertical integration operators ($\hat{\sigma}$) and ($\hat{\Delta}$) defined in equation (1) are required for the calculation of \hat{G} , \hat{D} , \hat{G} , \hat{D} and ultimately $\hat{\sigma}$ (from equations (9) and (18)) at the layers $\tilde{\sigma}_n$. The vertical integral $\hat{F}^{\hat{\sigma}}$ is approximated by \hat{F}^n , a simple quadrature extending from the surface ($\sigma = 1$) to $\tilde{\sigma}_n$. \hat{F} is approximated by $\hat{F}^{\hat{\sigma}}$, the same quadrature extending from $\sigma = 1$ to $\sigma = 0$. Thus, if F is a level variable, then the approximation for \hat{F} at $\sigma = \tilde{\sigma}_n$ is

$$\hat{F}^n = \sum_{k=n+1}^N F_k \tilde{\delta}_{k-1} \quad 1 \leq n \leq N-1 \quad (59)$$

and the approximation for \hat{F} is

$$\hat{F}^{\hat{\sigma}} = \sum_{k=1}^N F_k \tilde{\delta}_{k-1}$$

In this manner, it is possible to obtain the quadrature analogues of \hat{G} , \hat{G} , \hat{D} , \hat{D} and thus $\hat{\sigma}$ at each of the layers $\tilde{\sigma}_n$, $1 \leq n \leq N-1$. At $\tilde{\sigma}_N$ we have assumed $\tilde{\sigma}_N = h\tilde{\sigma}_{N-1}$ where h is an empirical constant $0 \leq h \leq 1$.

Similar approximations are used for any remaining terms on the right-hand-sides of equations (49)–(53).

All that remains to be discussed is the solution of the boundary value problem (53). The consistent vertically discretized form of this equation for $2 \leq n \leq N-1$ is

$$\frac{1}{\delta_{n-1}} \left[\left(\frac{\overline{P_{n+1}} - \overline{P_n}}{\overline{\tilde{\gamma}}_n^* \overline{d_n}} \right) - \left(\frac{\overline{P_n} - \overline{P_{n-1}}}{\overline{\tilde{\gamma}}_{n-1}^* \overline{d_{n-1}}} \right) - \frac{R\Delta t^2}{a^2} l(l+1) \overline{P_n} = \right. \\ \left. \frac{1}{\delta_{n-1}} \left[\frac{1}{\overline{\tilde{\gamma}}_n^*} \{ \overline{\tilde{C}_T} \}_n - \frac{1}{\overline{\tilde{\gamma}}_{n-1}^*} \{ \overline{\tilde{C}_T} \}_{n-1} \right] + \{ \overline{C_D} \}_n \right] \quad (60)$$

where, as mentioned previously, n refers to level or layer, (\sim) indicates a layer value, and $\{ \}$ refers to a horizontal integration (equation 36).

Equation (60) yields $N - 2$ equations in the N unknowns $\overline{P_n}$, $1 \leq n \leq N$. To close the system it is necessary to obtain 2 additional equations involving respectively $\overline{P_1}$ and $\overline{P_N}$.

The top boundary condition is straightforward to apply. At $\sigma = 0$, $\dot{\sigma} = 0$, which implies $W = 0$ in the finite difference analogue of equation (52) applied at σ_1 . This leads to the following relation between \overline{W}_1 and \overline{D}_1 :

$$\frac{\overline{W}_1}{\overline{\delta}_0} + \overline{D}_1 = \{ \overline{B_w} \}_1.$$

Combining the above equations with the finite difference analogues of equations (49) and (50), applied at σ_1 and $\tilde{\sigma}_1$ respectively, yields an equation involving $\overline{P_1}$ and $\overline{P_2}$ only:

$$\frac{1}{\overline{\delta}_0} \left(\frac{\overline{P_2} - \overline{P_1}}{\overline{\tilde{\gamma}}_1^* \overline{d_1}} \right) - \frac{R\Delta t^2 l(l+1)}{a^2} \overline{P_1} = \frac{\{ \overline{\tilde{C}_T} \}}{\overline{\delta}_0 \overline{\tilde{\gamma}}_1^*} + \{ \overline{C_D} \}_1 \quad (61)$$

To close the system at the bottom boundary is less straightforward. Recalling the definition of W and the assumptions made for $\tilde{\gamma}_N$ and $\tilde{\sigma}_N$ and noting that Φ_s is time-invariant, it can be shown that the finite difference analogue of equation (50) degenerates to the following when applied at $\tilde{\sigma}_N$.

$$\frac{-\overline{P_N}}{\overline{\tilde{\lambda}}_N^* \overline{d_N}} + \frac{R\Delta t}{\overline{\tilde{\lambda}}_N^*} h \overline{\tilde{\gamma}}_{N-1}^* \overline{W}_{N-1} + R\Delta t \overline{W}_s = \frac{\{ \overline{\tilde{C}_T} \}_N}{\overline{\tilde{\lambda}}_N^*} \quad (62)$$

where

$$\overline{\tilde{\lambda}}_N^* = \frac{R \overline{T}_N^*}{\overline{C}_p} + \frac{\overline{T}_N^*}{\overline{d}_N} - h \overline{\tilde{\gamma}}_{N-1}^* \overline{\sigma}_{N-1}$$

The finite difference analogues of equations (49) and (52) applied at σ_N yield a relation between \overline{W}_s , \overline{W}_{N-1} and $\overline{P_N}$. A third relation between $\overline{P_{N-1}}$, $\overline{P_N}$ and \overline{W}_{N-1} can be obtained by applying the finite difference analogue of equation (50) at $\tilde{\sigma}_{N-1}$. This yields 3 equations in 4 unknowns $\overline{P_N}$, $\overline{P_{N-1}}$, \overline{W}_s and \overline{W}_{N-1} which can be used to obtain a single equation in $\overline{P_N}$ and $\overline{P_{N-1}}$; i.e.

$$\frac{1}{\delta_{N-1}} \left[\frac{-P_N}{\tilde{\lambda}_{N-1}^* d_N} - \left(\frac{P_N - P_{N-1}}{\tilde{\lambda}_{N-1}^* d_{N-1}} \right) \right] - \frac{R\Delta t^2 l(l+1)}{a^2} P_n^{-t} =$$

$$\frac{1}{\delta_{N-1}} \left[\frac{1}{\tilde{\lambda}_{N-1}^*} \{\tilde{C}_T\}_N - \frac{1}{\tilde{\lambda}_{N-1}^*} \{\tilde{C}_T\}_{N-1} \right] + \{C_D\}_N \quad (63)$$

where

$$\tilde{\lambda}_{N-1}^* = \frac{\tilde{\gamma}_{N-1}^* \tilde{\lambda}_{N-1}^*}{\tilde{\lambda}_{N-1}^* + h\tilde{\gamma}_{N-1}^*}$$

Equations (60), (61) and (63) define an $N \times N$ tri-diagonal matrix relationship for each horizontal mode (m, l) of the P_n^{-t} , $1 \leq n \leq N$. These matrix problems are easily solved by an efficient tri-diagonal matrix algorithm. Once the P_n^{-t} have been calculated, back substitution into the vertically discretized forms of (49) and (50) yields D_n^{-t} and \tilde{W}_n^{-t} respectively. Substitution of P_N^{-t} and \tilde{W}_{N-1}^{-t} into (62) yields \tilde{W}_s , from which q can be obtained using (51). The definition of the $(-t)$ operator then yields $P_n(t + \Delta t)$, $D_n(t + \Delta t)$ and $q(t + \Delta t)$. The remaining variables $\Phi_n(t + \Delta t)$ and $\tilde{T}_n(t + \Delta t)$ are calculated diagnostically using the vertically discretized forms of equations (34) and (35). The explicit prognostic equations (47) and (48) yield $\zeta_n(t + \Delta t)$ and $S_n(t + \Delta t)$.

This formulation of the semi-implicit method does have the advantage of yielding a tri-diagonal matrix in the vertical at the expense of some conceptual complication. However, the extra calculations per timestep due to the semi-implicit calculation are completely negligible.

6 Physical parameterization

a Precipitation, Latent Heat Release and Convective Adjustment.

Consideration of large-scale heating by precipitation requires the introduction of a moisture variable to denote the local amount of water vapour present in the atmosphere, plus an assumption for the release of latent heat. All of the many measures of the local water vapour content of the air can be related, provided the temperature and pressure are known; the question arises as to which is most suitable for a spectral model. Experiments conducted by one of the authors (Simmonds, 1975) indicated that a spherical harmonic series approximation to the horizontal variation of dew point depression contains more information than a similar series approximation to relative humidity or water-vapour mixing-ratio. Dew-point depression also has the attractive property for a spectral model that it can never become physically unrealizable due to spectral truncation. Its simple vertical structure makes it well suited for sigma-coordinate models. It is the variable currently analysed at the Canadian Meteorological Centre.

The prognostic equation for dew-point depression (7) is obtained by subtracting the following tendency equation for dew-point temperature from the

thermodynamic equation (4). Since $T_d = T_d(p, r)$, where p is the pressure and r is the water-vapour mixing-ratio, we can write:

$$\frac{dT_d}{dt} = \left(\frac{\partial T_d}{\partial p} \right)_r \frac{dp}{dt} + \left(\frac{\partial T_d}{\partial r} \right)_p \frac{dr}{dt} \quad (64)$$

A natural assumption for the parameterization of large-scale heat release is that of no supersaturation, which can be satisfied in the following simple steps. Moisture is first advected conservatively

$$\left(\frac{dr}{dt} = 0 \right).$$

Since

$$\left(\frac{\partial T_d}{\partial p} \right)_r = \frac{RT_d^2}{\epsilon p L(T_d)}, \quad (65)$$

equation (64) leads to equation (7) for S . Next, supersaturation is removed by a procedure which consists essentially in solving the following set of equations

$$T_a - T = \frac{L}{C_p} (r - r_a) \quad (66)$$

$$r_a = h_s r_s(T_a) \quad (67)$$

where T , T_a and r , r_a represent the temperature and mixing ratio of a layer at a given location, respectively, before and after large-scale condensation has occurred, and $r_s(T)$ is the saturation mixing-ratio for the temperature T . To account for sub-grid-scale variations in moisture an empirical parameter, $h_s \leq 1$, has been introduced in (67), representing the value of relative humidity above which large scale condensation is considered to occur in the presence of ascending motion. At the present, the system (66)–(67) is solved, without iteration, by the generalized Newton-Raphson procedure described by Langlois (1973). The latent heat and moisture changes, corresponding to the differences $T_a - T$ and $r_a - r$ are included in the source terms H_T and H_M of the dynamic equations (4) and (7). Note that H_T correctly appears in both the temperature and dew point depression equations. The resulting amount of precipitation for a layer of thickness $\sigma_{n+1} - \sigma_n$ (in units of length) is then computed by the formula

$$P_r = p_s \frac{(\sigma_{n+1} - \sigma_n)}{\rho_w g} (r - r_a) \quad (68)$$

where ρ_w is the density of liquid water.

To make sure that the large-scale latent heating remains stable, a moist convective adjustment based on the principles of Manabe *et al.* (1965) is performed. The scheme changes the vertical profiles of temperature and moisture at a given location while conserving moist static energy and serves as a crude parameteriza-

tion of the effects of moist convection, including an evaluation of convective precipitation.

The conditions of its application to a given layer of the atmosphere are: (i) the relative humidity is greater than a critical value h_c , (ii) the air motion is directed upward and (iii) the lapse rate γ of potential temperature is less than a critical value γ_c , where γ_c is defined as a linearly weighted function of the dry adiabatic lapse rate $\gamma_d = 0$ and the moist adiabatic lapse rate γ_s :

$$\gamma_c = \chi_c(h, h_c)\gamma_s(T, r_s(T)) \quad (69)$$

with

$$\chi_c(h, h_c) = \begin{cases} 0 & h \leq h_c \\ (h - h_c)/(1 - h_c) & h_c < h < 1 \\ 1 & h \geq 1 \end{cases} \quad (70)$$

The last condition is similar to that imposed by Gadd and Keers (1970) to prevent the development of shocks caused by large sudden adjustments.

The convective adjustment process itself is best described by defining its end result:

$$\gamma_a(T_a) \geq \chi_c(h_a, h_c)\gamma_s(T_a, r_s(T_a)) \quad (71)$$

$$r_a = h_a r_s(T_a) \quad (72)$$

$$\int_0^1 (T_a - T) d\sigma = \frac{L}{C_p} \int_0^1 (r - r_a) d\sigma \quad (73)$$

where γ_a , T_a and r_a are the adjusted profiles of γ , T and r . These profiles are different from the original ones only in the layer (which may include several model levels) where inequality (71) was violated before and/or during the adjustment. In this layer, the relative humidity is now uniform and equal to the original humidity at the bottom; the equality sign in (71) is now valid. An upward transport of heat and moisture has taken place and any excess moisture has been released as convective precipitation. The discretized version of (71)–(73) must be solved iteratively.

In practice, the calculations of both large-scale and convective precipitation are done simultaneously. This rather efficient procedure is possible since the large-scale condensation scheme (66)–(67) is a subset of the moist convective adjustment scheme (71)–(73) corresponding to vanishing vertical heat and moisture fluxes with $h_a = h_s$. Furthermore, whenever the lapse rate γ of potential temperature is less than zero, a dry convective adjustment will be performed subject to the constraint of conservation of dry static energy. This is also a special case of system (71)–(73) with $\gamma_c = 0$ and no latent heat release.

b Orography

The model attempts to simulate orographic effects. Φ_s (the earth's surface topography) is represented by a series of spherical harmonics with the same truncation (J) as the other variables in the model.

Since the earth's surface topography has quasi-discontinuities in the first

derivative at the continental boundaries, Gibb's phenomena do occur in the truncated series representation of Φ_s . This is manifested primarily in negative values of Φ_s over the ocean, adjacent to high mountains, such as off the coast of Greenland. These negative excursions in Φ_s , although aesthetically displeasing, have never been observed to degrade the quality of the forecasts produced by the model.

c *Boundary Layer Parameterization*

Though more sophisticated parameterizations are under evaluation, F_λ , F_θ , H_T and H_M are presently calculated by bulk aerodynamic formulae.

For F_λ and F_θ at the lowest level, Cressman's (1960) drag formulation is used. H_T and H_M are assumed to be zero over land and ice. Over the open ocean, fluxes of heat and moisture into the lowest model layer are calculated. H_T depends upon the windspeed and the difference between the lowest layer air temperature extrapolated adiabatically to the surface and a given sea surface temperature. H_M is a function of the windspeed and the difference between the lowest layer mixing ratio and the saturated mixing ratio of air in contact with the sea.

7 Summary

A multi-level spectral primitive equation model has been developed for short-range forecasting over the globe or a hemisphere. The model, as described above, has certain theoretical advantages with respect to classical grid-point models.

Part II of this paper will attempt to demonstrate that the theoretical potential of this model can be realized in practice. Firstly, initialization from real data, model resolution and computational efficiency will be discussed. Then, case studies and verification statistics collected over many months of parallel forecasting with other models will be presented. The results of these experiments will clearly indicate that spectral models do indeed have operational capabilities for short-range forecasting.

Acknowledgements

The authors wish to particularly thank Dr. Richard Asselin for his advice and encouragement and Dr. William Bourke for sending us an early version of his multi-level spectral model. The authors also wish to thank Drs. André Robert, Ian Rutherford, Andrew Staniforth, Brian Hoskins and David Baumhefner. The manuscript was typed by Mrs. Lise Paradis.

References

- ASSELIN, R., 1972: Frequency filter for time integrations. *Mon. Wea. Rev.*, **100**, 487-490.
- 1975: Personal communication.
- BAER, F., 1972: An alternate scale representation of atmospheric energy spectra. *J. Atmos. Sci.*, **29**, 649-664.
- BLINOVA, E.N., 1943: *Dokl. Akad. Nauk SSSR (Rept. Acad. Sci. USSR)*, **39**, pp. 284.
- BOURKE, W., 1972: An efficient one-level

- primitive equation spectral model. *Mon. Wea. Rev.*, **100**, 683-689.
- 1974: A multi-level spectral model. I - Formulation and hemisphere integrations. *Mon. Wea. Rev.*, **102**, 687-701.
- CRESSMAN, G.P., 1960: Improved terrain effects in barotropic forecasts. *Mon. Wea. Rev.*, **88**, 327-342.
- ELIASSEN, E.B., B. MACHENHAUER and E. RASMUSSEN, 1970: On a numerical method for integration of the hydrodynamical equations with a spectral representation of the horizontal fields. Institute of Theoretical Meteorology, University of Copenhagen, Report No. 2.
- ELLSAESSER, H.W., 1966: Evaluation of spectral versus grid methods of hemispheric numerical weather prediction. *J. Appl. Meteor.*, **5**, 246-262.
- FLATTERY, THOMAS W., 1970: Spectral models for global analysis and forecasting. Air Weather Service Technical Report 242.
- GADD, A.J., and J.F. KEERS, 1970: Surface exchanges of sensible and latent heat in a 10-level model atmosphere. *Quart. J.R. Met. Soc.*, **96**, 297-308.
- LANGLOIS, W.E., 1973: A rapidly convergent procedure for computing large-scale condensation in a dynamical weather model, *Tellus*, **25**, 86-87.
- MACHENHAUER, B. and R. DALEY, 1972: A baroclinic primitive equation model with a spectral representation in three dimensions. Institute of Theoretical Meteorology, University of Copenhagen, Report No. 4.
- MANABE, S., J. SMAGORINSKY and R.F. STRICKLER, 1965: Simulated climatology of a general circulation model with a hydrologic cycle. *Mon. Wea. Rev.*, **93**, 769-798.
- ORSZAG, STEVEN A., 1970: Transform method for calculation of vector coupled sums: application to the spectral form of the vorticity equation. *J. Atmos. Sci.*, **27**, 890-895.
- 1974: Fourier series on spheres. *Mon. Wea. Rev.*, **102**, 56-75.
- PHILLIPS, N.A., 1957: A coordinate system having some special advantages for numerical forecasting. *J. Meteor.*, **14**, 184-185.
- ROBERT, A.J., 1966: The integration of a low-order spectral form of the primitive meteorological equations. *J. Meteor. Soc. Japan*, **44**, 237-245.
- J. HENDERSON and C. TURNBULL, 1972: An implicit time integration scheme for baroclinic models of the atmosphere. *Mon. Wea. Rev.*, **100**, 329-335.
- SILBERMAN, I., 1954: Planetary waves in the atmosphere. *J. Meteor.* **11**, 27-34.
- SIMMONDS, I., 1975: The spectral representation of moisture. *J. Appl. Meteor.*, **14**, 175-179.

**Short-Term Forecasting with a Multi-Level Spectral
Primitive Equation Model
Part II – Hemispheric Prognoses and Verification**

Roger Daley, Claude Girard and John Henderson
*Atmospheric Environment Service
Montreal, Quebec*

and

Ian Simmonds
*Geophysical Fluid Dynamics Program/NOAA
Princeton University, Princeton, N.J., 08540. U.S.A.*

[Manuscript received 18 December 1975; in revised form 24 February 1976]

ABSTRACT

The spectral global baroclinic primitive equation model described in Part I of this paper has been extensively tested. The model has been run daily from operational analyses for over a year. From this large sample of forecasts, verification statistics have been collected and compared with similar statistics collected from three competitive grid-point models. The spectral model is also compared with the grid-point models in a synoptic case study.

A second case study demonstrates the effect of horizontal resolution and physical effects on spectral model forecasts. The results of these experiments demonstrate that the spectral model is highly competitive with other models, in terms of both accuracy and computational efficiency. On 18 February 1976 the spectral model became the operational Canadian large-scale forecast model.

1 Introduction

A multi-level spectral primitive equations model was introduced in Part I of this paper (hereinafter referred to as I). The model was designed for short- or medium-range numerical weather prediction over the globe or a hemisphere. In I we claimed that the model could compete successfully with conventional grid-point models in terms of both accuracy and efficiency. We will attempt to substantiate this claim by means of timing tests, verification statistics and a synoptic case study involving the spectral model and various grid-point models. In addition, a second synoptic case study will test various aspects of the spectral model alone, such as horizontal resolution and moisture processes.

The spectral model is based upon the spherical harmonic method of Eliassen *et al.* (1970) and Bourke (1972, 1974). All vertical operations are handled by finite differencing and a semi-implicit algorithm in the manner of Robert *et al.* (1972) enables the model to use relatively long timesteps. Physical pro-

cesses include orography, precipitation and latent heat release, dry and moist convective adjustment and a simple boundary layer parameterization.

The model has been run and verified daily at the Canadian Meteorological Centre on a quasi-real-time basis since late 1974. This version of the model has 5 vertical levels (equally spaced in σ). The horizontal resolution is $J = 20$ (see I) and the model will be designated as SP20 (spectral 20). This model is hemispheric and includes all physical processes mentioned in I, unless otherwise indicated. We will on occasion refer to SP15 or SP30 which are the same as SP20, except that $J = 15$ or $J = 30$ respectively.

First, we will discuss the initialization of the spectral model from real data objective analyses. We will then proceed to a synoptic case study in which the forecasts produced by various configurations of the model will be examined. This case study will demonstrate that the spectral model can successfully forecast a developing cyclone. The effect of horizontal resolution and moisture processes on the forecast will be briefly examined.

We will then proceed to an inter-model comparison, which has three sections. First, we will introduce three grid-point models. Two of the grid-point models are primitive equation models and have the same vertical structure, semi-implicit algorithm and physical parameterization as the spectral model. The similarities between the spectral model and these grid-point models provide a unique opportunity for comparison of the grid-point and spectral techniques. We will then proceed to compare equivalent grid-point and spectral models from the point of view of computational efficiency. The inter-model comparison will terminate with a discussion of model accuracy utilizing verification statistics, a synoptic case study and a displacement error study.

Care must be taken in the interpretation of the results of these inter-model comparisons. The two primitive equation models are indeed very similar to the spectral model and meaningful comparisons can be made. However, they were not developed primarily for the purpose of this comparison and differ from the spectral model in many minor respects not explicitly mentioned here. Moreover, there is a fundamental difficulty in comparing the horizontal resolutions of the grid-point and spectral models. These uncertainties in the experiment do not permit us to conclude anything more definite than that the spectral and grid-point models are competitive.

2 Initialization

The model is run from an objective analysis (Rutherford, 1976) which provides wind components, heights, temperatures and dewpoint spreads at standard pressure levels on a 2805-point polar-stereographic grid (381-km grid-length at 60°N). For the spectral model these variables are first bi-cubically interpolated to the Gaussian transform grid. This requires some extrapolation in the tropics. The symmetry conditions are then used to determine the Southern Hemisphere. The surface topography Φ_s is then used for the vertical interpolation to the sigma surfaces of the model. The spectral coefficients of the model variables Φ , ζ , D , S , q are obtained by spectral analysis.

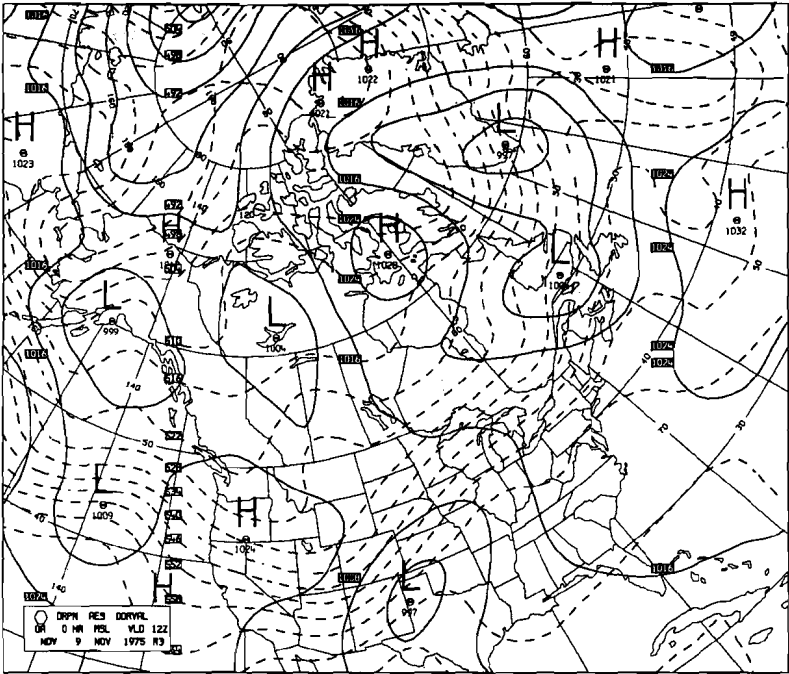


Fig. 1 (a) Mean sea level pressure in millibars (solid lines) and 1000–500 millibar thickness in dekameters (dotted lines) from objective analysis of 12Z 9 November 1975 over North America.

After the model has run, the reverse procedure is used to produce polar stereographic grid-point values on constant-pressure surfaces.

3 Spectral model synoptic case study

We first present a synoptic case study involving the spectral model alone. The case of 12Z 9 November 1975 was chosen primarily because there was a good example of cyclogenesis over the North American continent. We will examine 36-h forecasts produced by SP15, SP20 and SP30, as well as SP20 run without moisture processes.

In Fig. 1(a) is the initial mean-sea-level pressure (millibars) and 500–1000-mb thickness (dekameters) for the region of North America. In 1(b) is the verifying objective analysis for 36 h later. In 1(c) is the standard SP20 36-h forecast. In 1(e) and 1(f) are the forecasts made with SP15 and SP30 respectively. In these cases, the models are run with all the physical processes described in I. In Fig. 1(d) is shown the forecast made with SP20 but with all moisture processes (precipitation, latent heat release and moist convective adjustment) turned off.

The interesting cyclone is the one that starts off in northern Texas and ends up near James Bay, deepening 15 millibars. It is interesting to note that the displacement errors of all the models are relatively small and similar, although

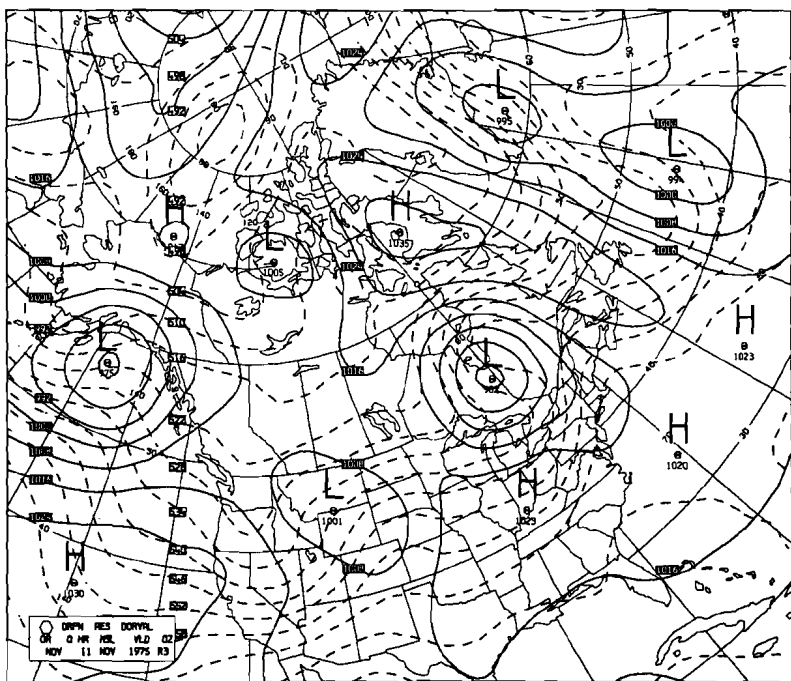


Fig. 1(b) Objective analysis 36 h later, 00Z 11 November 1975.

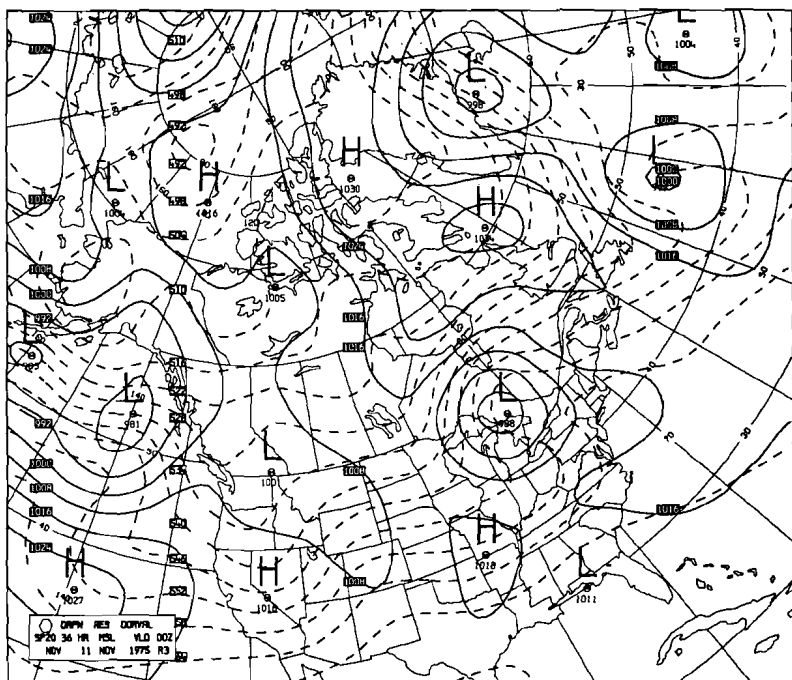


Fig. 1(c) 36-h forecast by sp20.

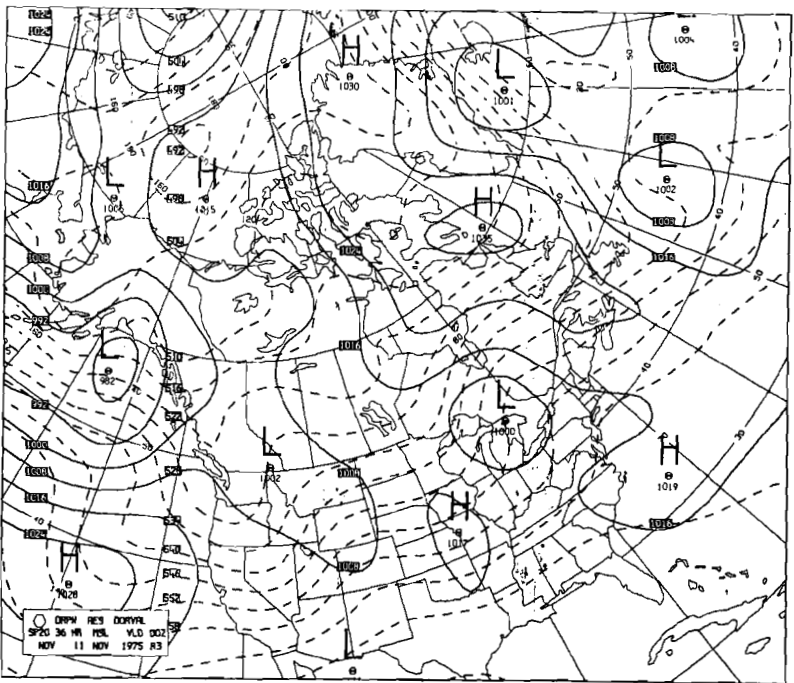


Fig. 1(d) 36-h forecast by SP20, without moisture.

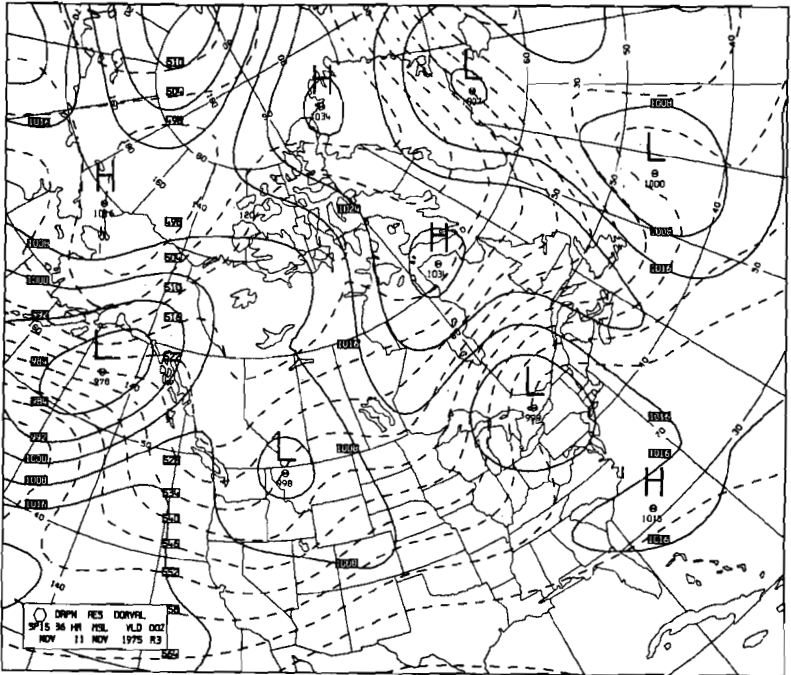


Fig. 1(e) 36-h forecast by SP15.

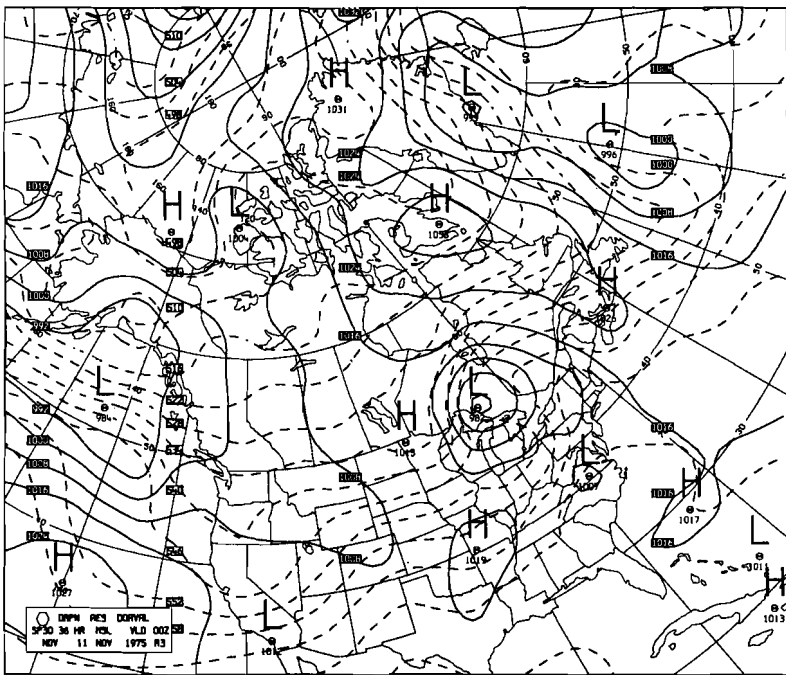


Fig. 1(f) 36-h forecast by SP30.

SP15 has a somewhat larger cross-track error. In other words, for this case at least, increasing resolution does not affect the displacement error markedly.

However, both the addition of moisture processes and increasing resolution clearly affect the development of this cyclone. The associated frontal wave, as seen in the thickness pattern, is clearly handled best by SP30. The system off the west coast of Canada is not handled well by SP30, but there is less data in this region.

In Fig. 2 is presented the 24-h precipitation (inches) over North America for the period 00Z 10 November 1975 to 00Z 11 November 1975. This is the last 24 hours of the case shown in Fig. 1. In Fig. 2a is the observed precipitation, in Fig. 2b that predicted by SP20, corresponding to the mean sea level pressure forecast of Fig. 1(c).

The main precipitation area associated with the James Bay low is well forecast, but the secondary area over Labrador is completely missing. There is some skill on the Pacific coast, but the precipitation there is underforecast, possibly due to insufficient resolution in the topography field.

4 Inter-Model Comparison

a The Control Models

In this section will be introduced three grid-point models with which the spectral model will be compared. The three grid-point models are the Canadian

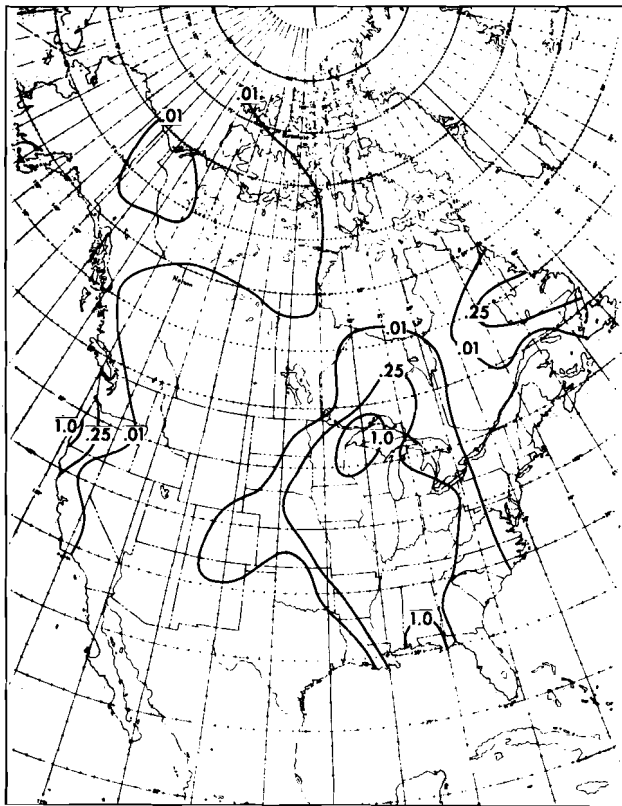


Fig. 2 (a) 24-h observed accumulated rainfall (inches) for the period 00Z 10 November 1975 to 00Z 11 November 1975.

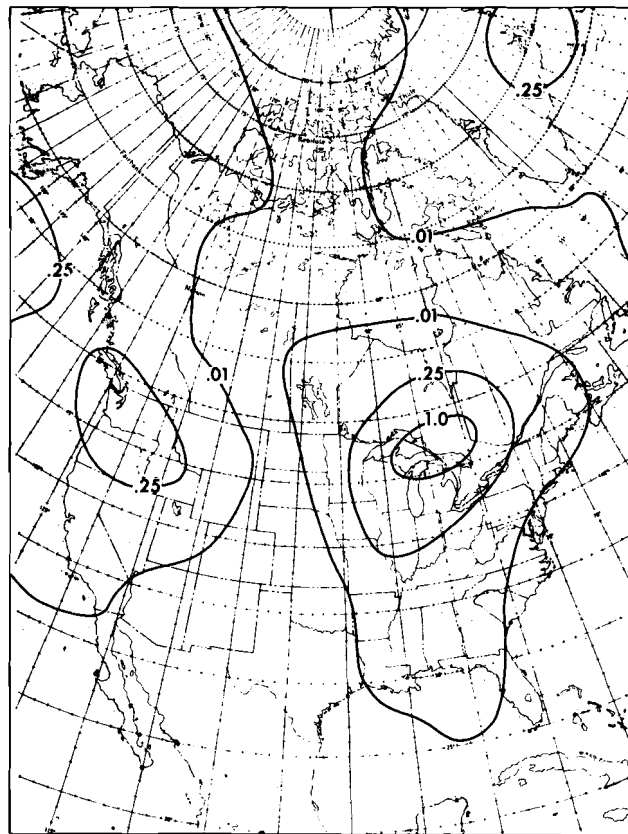


Fig. 2(b) Same as (a) except forecast by sp20.

operational large-scale numerical forecast model and experimental coarse-mesh and fine-mesh primitive equation grid-point models.

The Canadian operational model (in November 1975) was a 4-level (constant-pressure surface) filtered baroclinic model. It has been described by Robert (1963) and will be designated as FB. This model is a statistical-dynamical model run with a standard 381-km grid-length (at 60°N) over a 2805-point polar-stereographic grid covering most of the Northern Hemisphere. This is the same polar stereographic grid mentioned in Section 2. It has very little physical parameterization, except certain statistical features which correct for missing physical effects. The model is also used to provide input to the operational precipitation forecasting scheme of Davies and Olson (1973). Despite its simplicity, the model has been very successful, particularly in forecasting cyclogenesis off the east coast of North America. The timestep of this model is one hour.

The next model is a 5-level primitive equation grid-point model. This model has been described in an early version by Robert *et al.* (1972) and will be designated as CMGP (coarse-mesh grid-point). The model has similar physical parameterization, vertical structure and semi-implicit algorithm as the spectral model and runs on the same grid as FB. This model uses Shuman (1962) semi-momentum differencing and both second-order and fourth-order versions exist. The boundary conditions of CMGP are a point of difference with the spectral model. The grid-point model's boundary is a rectangle on the polar stereographic grid, which appears as a curved line with 4 cusps on the globe. The boundary conditions have been described by Asselin (1972) and consist of: the relative vorticity at inflow points is zero and the normal wind and normal surface pressure gradient are specified initially and are independent of time. Another point of difference with the spectral model is that the resolution of CMGP varies substantially between pole and equator because of the polar stereographic projection. The timestep is 60 min (second-order) and 45 min (fourth-order).

The third model is a limited-area fine-mesh version of CMGP. A one-level version of this model has been described by Asselin (1972). The model has 5 levels and runs with a 190.5-km grid-length on a polar stereographic grid with 2784 grid-points. The boundary conditions are: the relative vorticity tendency at inflow points, the normal wind tendency and normal surface pressure gradient tendency are all specified externally at each timestep. Both CMGP and SP20 have been used for this purpose. This model generally runs over an area covering North America with a 30 min timestep. We will hereinafter designate this model as FMGP (fine mesh grid-point).

b *Model Efficiency*

Model efficiency is usually not dwelt upon in scientific discussions, but an exception must be made here, for two reasons. Firstly, these models are designed to run from real data in real time and speed is very important. Secondly, the

TABLE 1. Running time for 36-hour forecasts by two different models.

	SP20	CMGP
	64 longitudes 26 Gaussian latitudes 40 minute timestep	2805 points 4th order differencing 45 minute timestep
Central Processor Time	5 minutes	6 minutes
Total Running Time	5.5 minutes	17 minutes ¹

most telling criticism of the spectral model has always been its computational inefficiency.

Ideally, we should wish to compare the efficiencies of spectral and grid-point models with equivalent horizontal resolution, all other aspects being equal. Unfortunately, it is very difficult to compare the resolution of the spectral model, which is expressed in terms of the shortest wavelength resolved, with the resolution of the grid-point model which is expressed in terms of the grid-length at some latitude. It is clearly not reasonable to compare them with respect to degrees of freedom, as a grid-point model has many redundant degrees of freedom (Orszag, 1971). Neither is it reasonable to use the two grid-length wave of the grid-point model as the shortest wave that it can resolve, because of the large truncation error in that wave. Consequently we will not attempt here to objectively compare model resolutions. Instead, we will simply state that on the basis of the results to be shown later and on many other forecasts not specifically discussed here, CMGP (fourth order) and SP20 produce an approximately equivalent forecast.

If this subjective statement is accepted, it is possible to compare computational efficiency. Firstly, it is clear that the spectral model has a considerable advantage in computer storage. SP20 (hemispheric) has 441 degrees of freedom per variable per vertical level. (As mentioned in I, for hemispheric integrations only the non-zero coefficients are retained). CMGP has 2805 degrees of freedom per variable per vertical level. This means that SP20 uses much less storage both on disk and in core.

As far as computation time is concerned, the results given here are machine dependent. We quote them for a CDC 7600 with approximately 25,000 words of fast core memory and 100,000 words of slow core memory available to the user. This is enough memory to allow SP30 (hemispheric) to run in core without core overlays and without core-to-disk data transfers during the time integration. CMGP, on the other hand, requires extensive overlaying and core-to-disk transfers every timestep.

In Table 1 is given the central processor time and total elapsed time (including core-to-disk transfers) for SP20 and CMGP to produce 36-h hemispheric forecasts. Both have 5 levels and include all physical processes mentioned in I.

¹Note added in proof: since reduced to 7 min by program optimization.

TABLE 2. Percentages of central processor time for various parts of the calculation in spectral models of different resolution.

	Gaussian Latitudes (hemisphere)	Longitudes	Time per Timestep (seconds)	Percentage of Time			
				Legendre Transform	FFT	Transform Grid Calculations	Misc
SP15	19	48	2.15	20.5	36.0	36.8	6.7
SP20	26	64	4.13	24.5	35.2	34.8	5.5
SP30	38	96	8.93	28.4	32.4	35.4	3.8

The number of Gaussian latitudes refers only to those in the Northern Hemisphere.

In the sense of Orszag (1970) where N indicates the number of degrees of freedom per dimension, the grid-point models have $O(N^2)$ operations per timestep per vertical level. By the same token, in the spectral model, the Fourier transforms are $O(N^2 \ln N)$, the Legendre transforms are $O(N^3)$ and the evaluation of the non-linear and forcing terms on the transform grid are $O(N^2)$. Clearly, because the Legendre transforms are $O(N^3)$, the spectral model will be less efficient at large N . However, at more moderate N , because of the large amount of calculation required in physical parameterizations, we might expect the $O(N^2)$ terms of the transform grid to predominate. The question is: at what value of N do the $O(N^3)$ terms start to seriously affect the efficiency?

Table 2 demonstrates that this point has clearly not been reached at $N = 30$. In Table 2 are plotted the percentages of central processor time involved in the Legendre transforms (including the time for evaluation of the Legendre functions), Fast Fourier Transforms, and the evaluation of the non-linear and forcing terms on the transform grid. There is also a miscellaneous column for the remaining time which consists largely of the semi-implicit algorithm and the diagnostic calculation of Φ , T from P and U , V from ζ , D . These timings are for SP15, SP20 and SP30 run hemispherically with all physical processes mentioned in I.

It can be seen that the total running time increases roughly as $O(N^2)$ between SP15 and SP30. In addition, even with SP30, the evaluation of the Legendre transforms is still not the most time-consuming operation. So we must conclude that the resolution at which the calculations become $O(N^3)$ is greater than $N = 30$.

Although it must be stated that the degree of program optimization of CMGP is not as great as in SP20, one must nevertheless conclude from Tables 1 and 2 and the above discussions, that numerical forecasting by the spectral method is an efficient procedure on a large-scale computer.

c Forecast Accuracy

This section will consist firstly of a synoptic case study of the four models SP20,

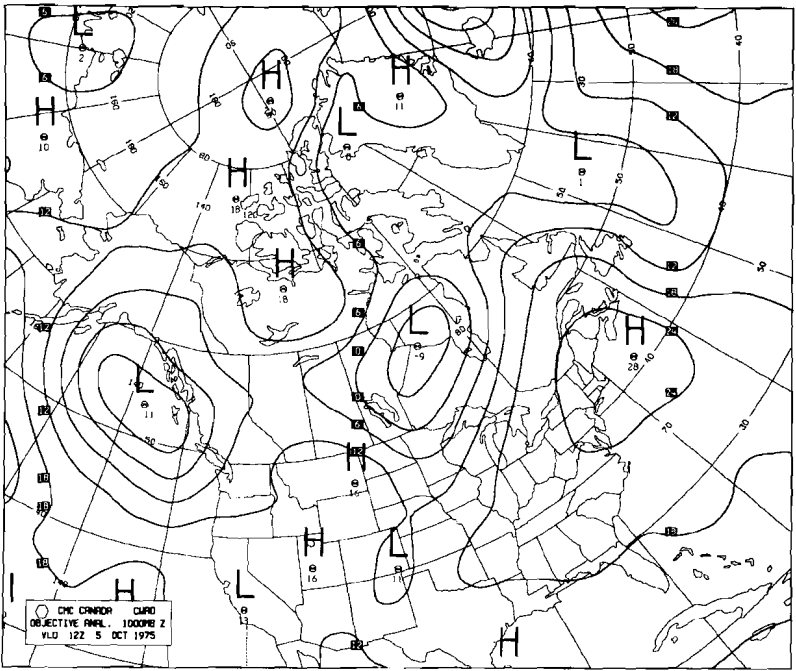


Fig. 3 (a) 1000-mb height (dam) from objective analysis of 12Z 5 October 1975.

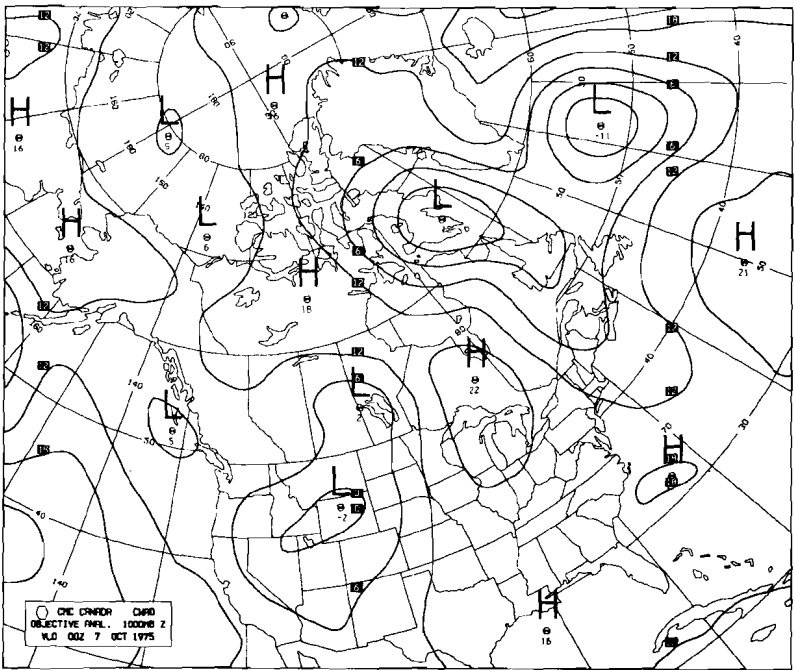


Fig. 3(b) Objective analysis 36 h later, 00Z 7 October 1975.

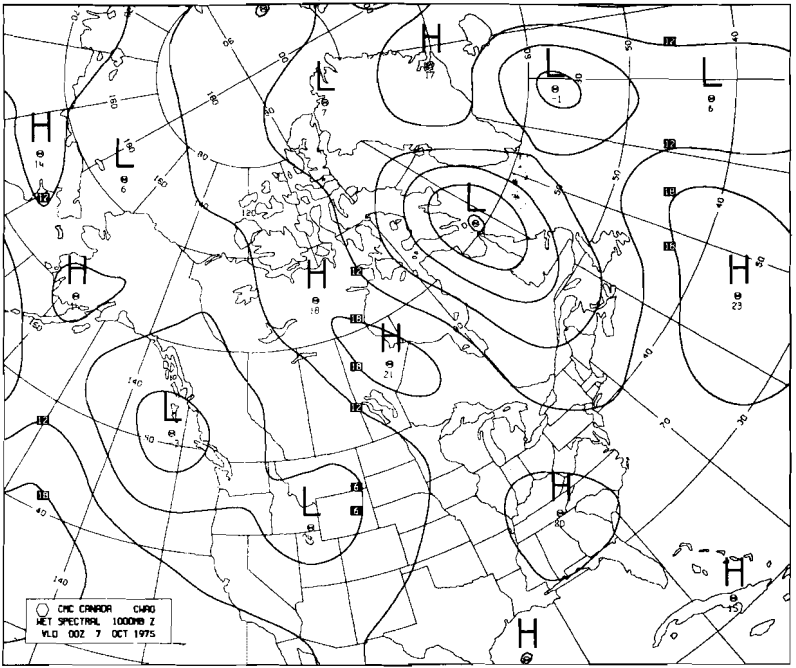


Fig. 3(c) 36-h forecast by sp20.

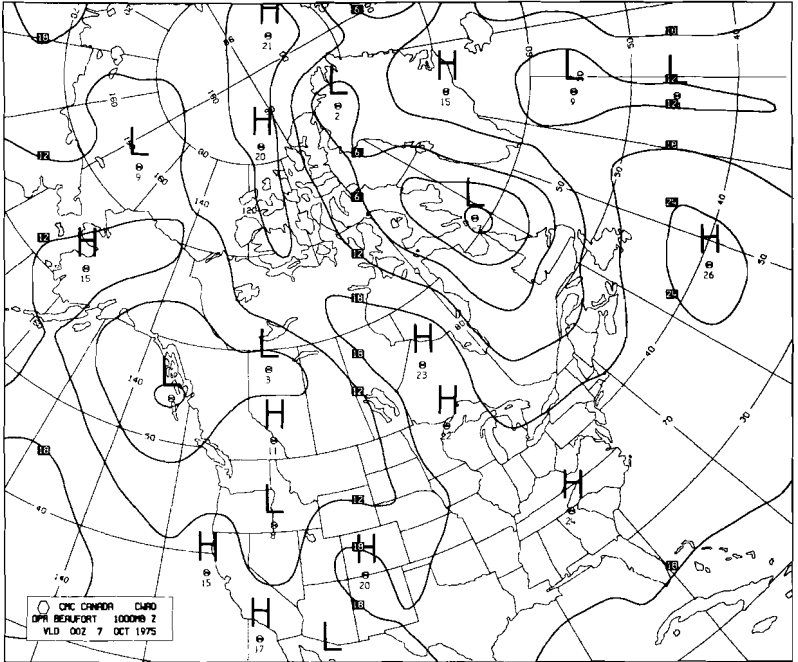


Fig. 3(d) 36-h forecast by cmgp.

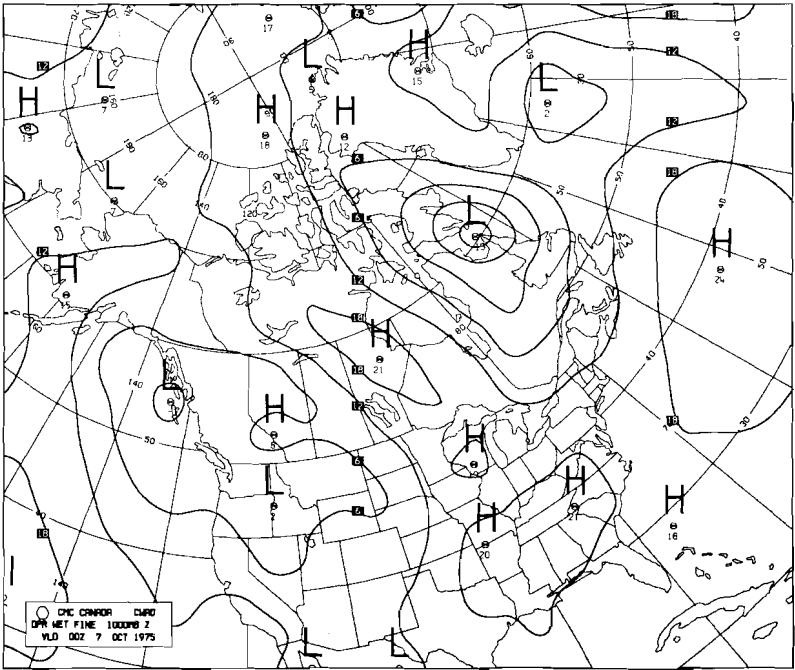


Fig. 3(e) 36-h forecast by FMGP.

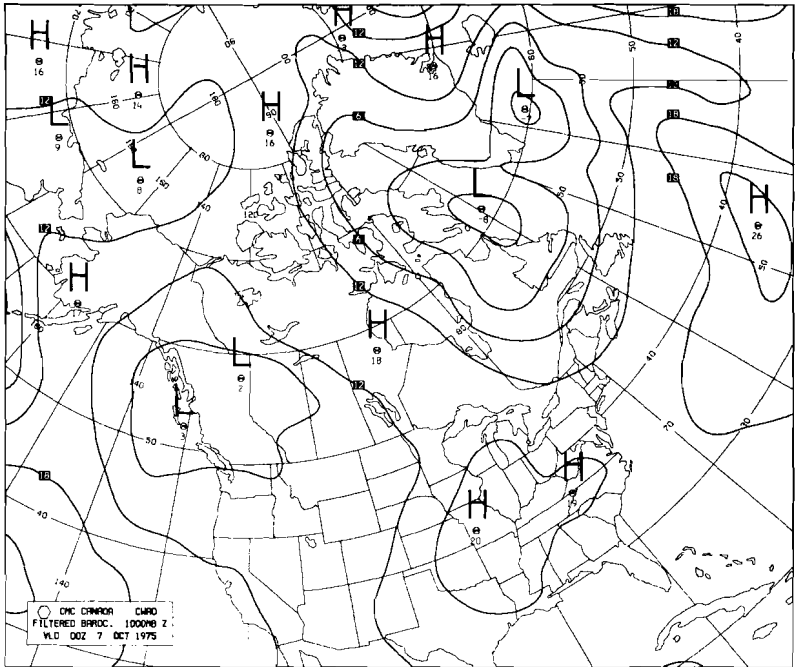


Fig. 3(f) 36-h forecast by FB.

FB, CMGP and FMGP. Next, verification statistics for the four models for the period January 1975 to October 1975 will be examined. Finally the results of a study of the 1000-mb 36-h displacement errors in SP20, CMGP and FB will be presented.

In Fig. 3(a) is presented the initial 1000-mb height field (dekametres) for 12Z 5 Oct. 1972 over a North American window. In 3(b) is shown the verifying objective analysis 36 h later. In 3(c), 3(d), 3(e) and 3(f) are shown the 36-h forecasts of SP20, CMGP, FMGP and FB verifying at the same time.

This case was chosen more or less randomly and does not contain a particularly interesting or difficult synoptic situation. Similarly, it does not demonstrate marked superiority for any particular model. What it is primarily intended to show is that SP20 has sufficient resolution to provide as creditable a forecast as the three grid-point models. It is able, for example, to forecast the displacement of the Hudson Bay low reasonably accurately and it correctly forecasts the development of a low in the Western U.S. On the other hand, the development of the cyclone that moves southeast of Greenland is not well forecast, although, the other primitive equation models CMGP and FMGP have the same fault.

Model verification statistics such as root-mean-square-error and S1 score (Teweles and Wobus, 1954) give some indication of the relative performance of different models. We have collected verification statistics from 10 months of daily forecasts by the models. Despite the large sample, however, some caution must be exercised in interpreting the results. Both types of scores are somewhat sensitive to space filtering. In addition all of the models except FB were altered occasionally during the period. However, the intention here is merely to show that the spectral model is competitive with grid-point models, and the following three figures would certainly indicate that this is so.

In Fig. 4 is presented the 500-mb 36-h r.m.s. height error averaged monthly for the models, SP20, FB, CMGP and FMGP. The graphs cover the period January

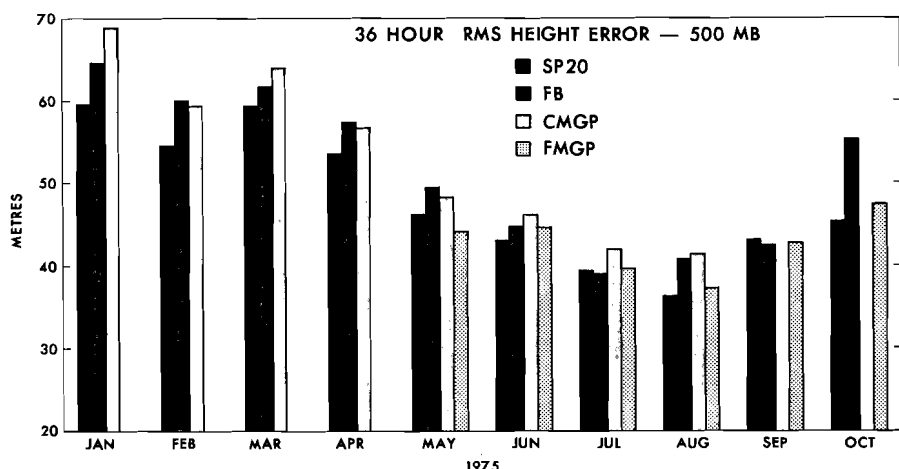


Fig. 4 Monthly averaged 36-h root mean square 500-mb height errors (m) for SP20, FB, CMGP and FMGP for January to October, 1975.

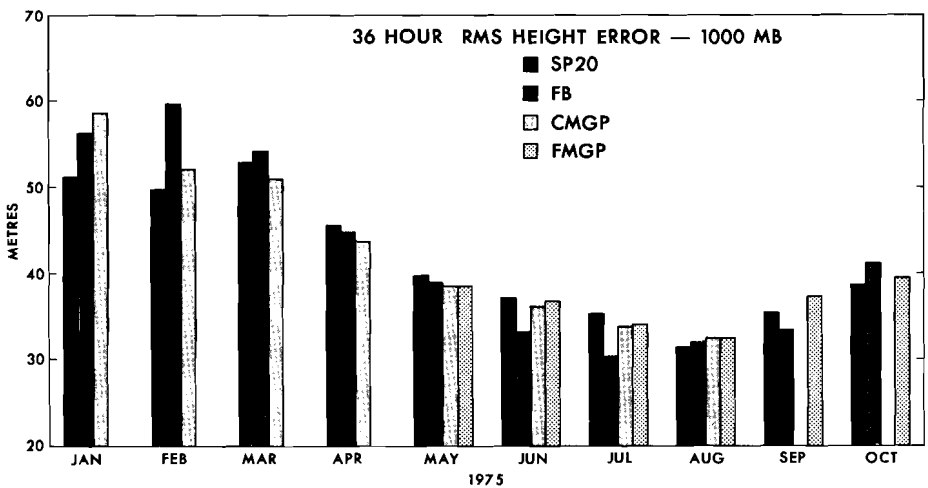


Fig. 5 Same as Fig. 4, except at 1000 mb.

to October, 1975, although verification statistics for FMGP were available only from May on. The averages represent at least one run daily for each model. All models were run from late (i.e. complete) objective analyses. The verification area is what is known as Area 6 at the Canadian Meteorological Centre and covers Canada and parts of the U.S., Alaska and Greenland. It is a rectangle on the polar stereographic projection with the corner points (21.9°N, 111.4°W), (49.9°N, 154.7°W), (68.8°N, 20.9°W), (28.2°N, 64.5°W).

Several facts should be noted in order to interpret these results correctly. Firstly, SP20 was run without moisture processes until September, 1975. Secondly, CMGP was run with only second-order differencing until the summer months, and was no longer verified after August, 1975.

In Fig. 5 are presented the 1000-mb 36-h r.m.s. height error averaged monthly for the four models. Fig. 6 shows the monthly averaged S1 scores for 36-h forecasts at 500 mb and 1000 mb for three models from August to October, 1975. The S1 scores before that point were unfortunately calculated incorrectly for all models and are unuseable. The comments appropriate to Fig. 4 apply also to Figs. 5 and 6.

Spectral models, by their very nature, have no linear phase error. There is of course time-truncation error (which should overestimate the phase speed) and there are non-linear effects. In practice, however, it is not clear whether the spectral model should have larger or smaller displacement errors than grid-point models.

In Table 3 are presented 1000-mb displacement errors for three models during the period 18 January 1975 to 18 March 1975. The procedure followed was similar to that of Druyan (1974). Ten identifiable cyclones, with tracks that could be followed easily, were chosen. The displacement errors of the 36-h prognoses of the three models were calculated and presented in the same

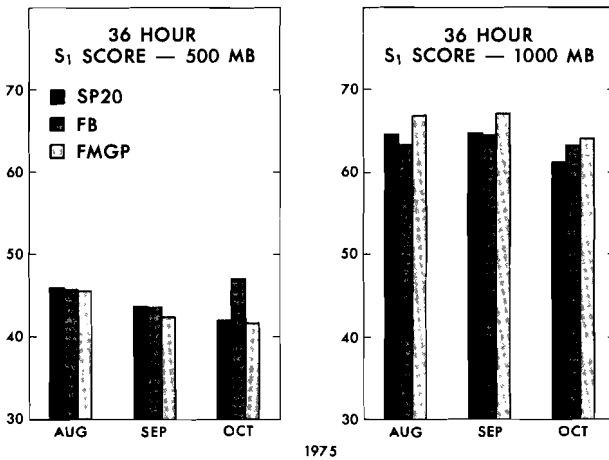


Fig. 6 Monthly averaged 36-h S₁ scores at 500 mb and 1000 mb for SP20, FB and FMGP for August, September and October, 1975.

TABLE 3. Errors in the displacement of 1000-mb cyclones in forecasts by three different models.

Cyclone Number	Total Distance Moved (km)	Percent of Downstream Movement Forecast			Cross Track Position Error (Km)		
		SP20	FB	CMGP	SP20	FB	CMGP
1	2050	100	105	90	160	120	300
2	2400	90	80	60	200	250	500
3	2000	80	70	60	0	200	400
4	0		Correct		0	0	0
5	2250	70	50	60	250	600	0
6	400	130	100	100	100	0	100
7	2500	75	80	60	300	0	150
8	1800	100	100	70	0	0	0
9	1400	80	85	45	200	0	500
10	2300	85	85	65	0	0	0

manner as Druyan (1974). Each cyclone was separate and was tracked using analyses every 12 hours.

The three models used were SP20, FB and CMGP (FMGP was not available at the time). What particularly stands out is how badly CMGP has underestimated the displacement of the cyclones. This can be attributed largely to the use of second-order differencing. It is interesting to note that SP20 is only fast on a single case, but never seriously underestimates the displacements. Cross-track errors are relatively small for all models.

5 Conclusions and future development

The potential and promise of the spectral method can now be realized for numerical weather prediction. A multi-level primitive-equation spectral model

has been constructed which yields competitive short-range forecasts in an efficient manner. The important breakthrough of Eliassen *et al.* (1970) and Orszag (1970) simultaneously eliminated the problems of inefficiency and physical parameterizations. The results of Bourke (1974) and the present study indicate that most of the remaining problems have been overcome.

The synoptic case study of Section 3 suggests that SP20 has sufficient resolution to stimulate cyclogenesis, although SP30 is even better.

The important results come from the inter-model comparison in Section 4. Three grid-point models, two of which had the same vertical structure, semi-implicit algorithm and physical parameterization as the spectral model, provided particularly appropriate comparisons. Timing tests demonstrated that the spectral model was at least as computationally efficient as an equivalent grid-point model. More importantly, a synoptic case study, ten months of verification statistics, and a displacement error study indicated that the spectral model was as accurate as the other models.

In the future the model will be improved in several directions. It is expected that the model will be run regularly with greater vertical and/or horizontal resolution (SP30 – 5 levels or SP20 – 10 levels are both quite feasible). In addition, much more sophisticated physical parameterizations will be used. Radiative effects will be taken into account and a planetary boundary layer simulation is currently being evaluated.

It is also expected that the model will be tested in the Canadian Meteorological Centre objective analysis cycle (Rutherford, 1976) to produce trial fields. Some experiments have been performed with the global version of the model, and it is anticipated that the model will be used during the First GARP Global Experiment.

After extensive subjective evaluation by the forecasting meteorologists of the Canadian Meteorological Centre and with due consideration to its computational efficiency, the spectral model has been chosen to replace the filtered baroclinic model as the operational Canadian forecast model. The implementation date was February 18, 1976.

Acknowledgements

The authors particularly wish to thank Dr. Richard Asselin and the staff of DRPN for their advice and encouragement. The manuscript was typed by Mrs. Lise Paradis.

References

- ASSELIN, RICHARD, 1972: Integration of a semi-implicit model with time-dependent boundary conditions. *Atmosphere*, **10**, 44–55.
- BOURKE, W., 1972: An efficient one-level primitive equation spectral model. *Mon. Wea. Rev.*, **100**, 683–689.
- 1974: A multi-level spectral model. I Formulation and hemisphere integrations. *Mon. Wea. Rev.*, **102**, 687–701.
- DAVIES, D., and M. OLSON, 1973: Precipitation forecasts at the Canadian Meteorological Centre. *Tellus*, **25**, 43–57.
- DRUYAN, LEONARD, 1974: Short-range fore-

- casts with the GISS model of the global atmosphere. *Mon. Wea. Rev.*, **102**, 269-279.
- ELIASSEN, E.B., B. MACHENHAUER and E. RASMUSSEN, 1970: On a numerical method for integration of the hydrodynamical equations with a spectral representation of the horizontal fields. Institute of Theoretical Meteorology, University of Copenhagen, Report No. 2.
- ORSZAG, STEVEN, 1970: Transform method for calculation of vector coupled sums: application to the spectral form of the vorticity equation. *J. Atmos. Sci.*, **27**, 890-895.
- 1971: Numerical simulation of incompressible flows within simple boundaries, I. Galerkin (Spectral) Representations. *Studies in Applied Mathematics*, **50**, 293-327.
- ROBERT, A.J., 1963: Baroclinic prediction experiments with a four-level statistical-dynamical model. *Canadian Meteorological Memoirs* 15, 32 pp.
- J. HENDERSON and C. TURNBULL, 1972: An implicit time integration scheme for baroclinic models of the atmosphere. *Mon. Wea. Rev.*, **100**, 329-335.
- RUTHERFORD, I.D., 1976: An operational three-dimensional multivariate statistical objective analysis scheme. JOC Study Group Conference on Four-Dimensional Data Assimilation - Paris 17-21 November, 1975. Report No. 11, the GARP Programme on Numerical Experimentation, 98-121.
-

NOTES AND CORRESPONDENCE

ON SNOW DEVILS

H.P. Wilson and D.B. Fraser

Arctic Weather Central

Edmonton, Alberta

[Received 22 January 1976]

In a recent issue of *Atmosphere*, Peterson (1975) has summarized the material on snow devils that he has been able to glean from the literature. We would like to add three items which have been collected by members of the Arctic Weather Centre in Edmonton.

The first is an occurrence which was observed by a pilot approaching for a landing at Paulatuk on 16 December 1966. He encountered severe turbulence and noted a set of conditions similar to those shown in Peterson's diagram and, in particular, snow devils on the slope to the south of Paulatuk. He landed on the ice which had been scoured almost free of snow by an intense snow devil on the previous day.

Paulatuk is situated at the head of Darnley Bay on the east side of Parry Peninsula. From the base of Parry Peninsula to the vicinity of Paulatuk the land rises to the south 250 m in 15 km to a lake-covered plateau. A shallow fan-shaped trough is evident south of Parry Peninsula with the Smoking Hills to the west and the higher Melville Hills to the east. The slope of the smoking hills is 10^{-1} and gale force downslope winds are common in early winter from the trough emptying on Parry Peninsula westward to Franklin Bay. When there is a moderate southerly foehn type flow of very stable air downslope winds are common along a zone about 50 km in width mainly to the west of Paulatuk.

Stefansson (1943) observed the wind when Langton Bay was open or covered only with thin ice. "When you come from inland travelling north towards the coast of Franklin Bay you notice a light breeze blowing at your back when you are six or eight miles from the edge of the plateau. By the time you come to the edge, about three or four miles from the ocean and begin to descend there is a terrific gale blowing. This gale may be sixty or eighty miles per hour on the beach but if you proceed north along the neck of Parry Peninsula eight or ten miles from the cliffs you gradually walk out of it and find yourself in calm weather or a light wind blowing in another direction."

The behaviour of katabatic flows down long steep slopes has been studied by Ball (1956 a and b). He showed that what was observed at Cape Denison, Antarctica, constituted an atmospheric jump that corresponded closely to a hydraulic jump. Fraser (1959) has used Ball's theory successfully to explain sudden changes of surface winds at Resolute but snow devils or "whirlies" have

not been observed there. A recent photo Auer (1973) confirms that atmospheric jumps are common.

As a third item, we would like to suggest that the presence of snow devils downslope from a jump may be explained as a result of the formation of Karman trails in the flow above the jump and their intensification by vertical stretching while passing through the jump.

This explanation depends on the assumption that there are obstacles to the flow above the jump, such as large boulders. From Karman's theory, as given in Prandtl and Tietjens (1957), beginning on page 130, vortices are shed from the sides of an obstacle, provided that the Reynold's Number is sufficiently high, and carried downstream in two parallel rows. The most stable arrangement is a systematically staggered pattern such that the separation of the two rows equals the width of the obstacle, and the spacing along each row is roughly four times that width. The motion of the vortices is somewhat slower than that of the undisturbed flow. Looking downstream, the sense of rotation is anticyclonic in the left and cyclonic in the right row.

Karman vortex trails have often been noted in satellite pictures of low clouds to the lee of isolated mountainous islands, sometimes extending downwind for distances greater than 100 km.

If a vortex from upwind enters a jump, it would be subjected to stretching and intensification, assuming that the pattern of flow in a vertical plane oriented along the flow is dominantly divergent. On emerging from the jump, its forward speed would decrease in response to the decrease of the speed of the ambient flow. The result would be an accumulation of vortices in a zone immediately downwind from the jump, and because of reduced separations of centres, the motions of individual vortices would tend to become random, resulting in collisions and dissipation.

This explanation appears to be preferable to one based on the assumption that the vortices are formed by twisting and tilting of horizontal to vertical vorticity.

References

- AUER, A.H., 1973: Cover photograph. *Bull. Amer. Meteor. Soc.*, **54**, No. 7 (July).
- BALL, F.K., 1956: The theory of strong katabatic winds. *Austral. J. Phys.*, **9**, 373–386.
- BALL, F.K., 1956: The katabatic winds of Adelieland and King George V Land. *Tellus*, **9**, 201–208.
- FRASER, D.B., 1959: Unstable character of northeasterly winds at Resolute, N.W.T., CIR-3189, TEC-300, Canadian Meteorological Service.
- PETERSON, R.E., 1975, Snow devils – early observations. *Atmosphere*, **13**, 77–79.
- PRANDTL, L. and TIETJENS, O.G., 1957: *Hydro and Aero-dynamics*, Dover Publications Inc., New York.
- STEFANSSON, V., 1943: *The Friendly Arctic*, New York, p. 478.
-

A STUDY OF PHOTOCHEMICAL AIR POLLUTANTS IN THE URBAN
AIRSHEDS OF EDMONTON AND CALGARY

H.S. Sandhu
Research Secretariat
Alberta Department of the Environment
Edmonton, Alberta

[Received 8 March 1976]

This study was commissioned by the Alberta Department of the Environment in 1974 and its objectives were:

1. To examine carefully the existing air pollutant data base for airsheds of Edmonton and Calgary;
2. To test the steady-state mechanism for the production of ozone through photochemical means by employing ambient air pollutant data available for extremes of meteorological conditions prevalent in Edmonton and Calgary;
3. To make available a report of the findings which will include a set of recommendations.

Meteorological and air pollutant data for the months of July and December 1974, monitored by different agencies for the two airsheds, were employed in carrying out the final analysis.

The final report was made public during December 1975. It was concluded that ozone was generated through photochemical reactions of air pollutants present in the urban airsheds of Edmonton and Calgary. Precise amounts of ozone produced could not be determined because of the lack of background ozone levels. Oxidant/ozone concentrations would stay below the provincial standard of 50 parts per billion in winter months because of frequent temperature inversions and relatively high concentration of nitric oxide in the airsheds. During summer months, oxidant/ozone concentrations above the Alberta standard would occur occasionally on sunny days. It was recommended that:

1. a short description of the strong and weak points of the present monitoring sites should be made available because many persons expressed interest concerning the criteria which were considered in establishing monitoring station sites;
2. monitoring instrument replacements and/or changes should be well documented in the pollution summary reports;
3. new instruments should be run alongside those already in operation for a minimum period of two weeks or longer prior to putting the new instruments into full operation;
4. calibration of the instruments should be checked regularly;

5. a better instrument should be used for monitoring both particulate matter and aerosols;
6. a study should be undertaken to determine Alberta background ozone levels as well as of all other air pollutants;
7. at least one monitor of solar intensity should be operated continuously for a minimum of three years in each of the two cities;
8. Alberta Department of the Environment should take steps to obtain carefully monitored data on ozone/oxidants from Edmonton Power in addition to data on oxides of nitrogen because of the importance of ozone in the city airsheds;
9. the mobile monitoring unit should be employed to measure air pollutants in the river valley in Edmonton;
10. the release of the Air Quality Index in the present form and its representativeness of city air quality should be examined critically;
11. a simple photochemical reaction scheme should be incorporated into the existing urban airshed models for the two cities;
12. environmental research relating to ozone-green plant interactions, in the presence and absence of sulphur dioxide, should be promoted;
13. field and laboratory investigations related to major air pollutant chemical transformations at sub-zero temperatures should be promoted;
14. short term micrometeorological studies related to urban airsheds should be promoted;
15. monitoring of *PAN* (peroxyacetyl nitrate) and *PPN* (peroxypropionyl nitrate) should be carried out prior to establishing a standard for hydrocarbons.

Most of these recommendations have already been adopted by the Alberta Department of the Environment. Technical papers from this study will be submitted for publication.

BOOK REVIEWS

WORLD SURVEY OF CLIMATOLOGY, volume 14, CLIMATES OF THE POLAR REGIONS. S. Orvig, Editor. Elsevier Publishing Company, Amsterdam, 1970, 370 pp. hardcover \$47.50.

Conceived in the same spirit as the Köppen-Geiger *Handbuch der Klimatologie* of the 1930's, the 15-volume *World Survey of Climatology* under the general editorship of Helmut Landsberg is providing an opportunity to stop and assess what has been accomplished by a whole new generation, an age of remarkably imaginative technical advance in instrumentation and observation, and in the form of the computer; years which have seen the expansion of the observational network into the upper atmosphere and into less accessible regions. Although volume 14, *Climates of the Polar Regions* first appeared in 1970, its value as part of this classic series should in no way have lessened. The explosion of information for the Arctic and Antarctic came about in the 1950's and early 1960's. This volume was well-timed.

Climates of the Polar Regions retains the same regional division as the Köppen-Geiger Handbook, with quite separate studies of *Greenland* (now unified under a single author, P. Putnins), the *North Polar Basin* (E. Vowinckel and S. Orvig) and the *Antarctic* (W. Schwerdtfeger). The volume has been edited by Sverre Orvig, who has written a brief introduction. Each regional account is approached in a completely different manner which makes for an interesting comparison in the interpretation and presentation of basically similar types of data.

Putnins takes a dynamic-synoptic approach to the *Climate of Greenland*. After an introduction, in which he discusses succinctly the nature of the island and some of the essential climatic questions which follow, the author plunges into the *weather dynamics* of the Greenland area, emphasizing the role of this extraordinary, longitudinal, mountain/ice barrier to westerly flow, pointing to its asymmetry with respect to the pole (unlike Antarctica) in the furthering of meridional exchanges. A detailed discussion follows on the many aspects of disturbances in this region, including the problem of their crossing the ice cap. The effect of the shallow but strong, persistent radiation inversion over the ice cap on coastal cyclogenesis and winds enters into the discussion, but the radiative role of this great mass of ice has still to be fully explored. To follow, the distributions of the main climatic elements are described for the ice cap and for the coastal region, with general reference to major flow patterns, storm systems and local winds. The section on *the ice cap* includes a brief treatment of sunshine, radiation and albedo, but in general the radiation balance is integrated into the overall scheme in so far as atmospheric conditions of clear sky, cloud and humidity set certain limits to energy exchanges. For the *coastal region*, no sunshine or radiation data are given; here, the considerable variation in temperature is seen qualitatively as a result of the interaction of synoptic situations with such local factors as orography and the presence of open water. The concluding section on *climatic trends* (temperature) is the least effective. Since this volume was published there has been much soul-searching concerning the best use of climatic information to define significant fluctuation. It is a pity that some results from the CRREL deep ice core studies could not have been incorporated. The references reach to 1964. Other sources are given, together with tables for 18 stations in the format accepted for the Survey. The tabulations refer to periods within 1931 and 1956.

The chapter contains a wealth of information, but to have proceeded at times by means of explicit synoptic example would have added further to its value and clarity. Also, the climate of the coastal region has been rather short-changed. Further analysis could have been undertaken with the data and published work available. It is interesting to see the ice cap section the richer in statistical information and physical explanation, and this in spite of the long records for the coast. This may reflect the importance of relatively short periods of intensive observation by highly trained and motivated researchers, or simply the belief

that the climate of the ice cap is of greater general significance than the local climates of the coastal valleys. Applied climatology is not considered.

Putnins text is smooth, the detail intricately woven, but there is a real need for more visual representation of some of the verbal descriptions of the atmospheric circulation, as well as a general map to help set the scene and indicate the sites mentioned in the text. Sustained descriptive writing is also helped by careful "phrasing" of the text in the visual lay-out of the printed page. It seems that this author has suffered most from two oddities of the type-set: firstly, the minimal distinction between section and sub-section headings so that the design of the text is not readily visible; secondly, the absence of indentation and spacing to mark the beginning of a new paragraph—nothing to pace the eye, to prepare the mind for a new idea or further development of the logic.

In their energy budget approach to the *Climate of the North Polar Basin*, Vowinckel and Orvig present as a whole the results of a number of years of sustained research. Their model, which lays stress on the physical processes of energy exchange between atmosphere and ocean, has to rely not only on limited data over the Arctic Ocean (essentially the drifting ice stations), but on those elements most difficult to measure such as cloud and humidity; it also requires a knowledge of the changing ice-cover characteristics and water temperatures. However, even if we are asked by the authors to consider the resulting climatological values as only first approximations, the model provides an excellent framework for a detailed discussion of the fundamental processes and problems in Arctic climatology. Orvig, however, as Editor, goes further: he suggests that for polar regions the testing and verifying of theories with real data would seem to be the major guide, *if not the sole guideline* (reviewer's italics), for a climatology (p. 1). This is a strong statement.

Separating the Arctic Ocean into three broad regions based on the seasonal ice cover and amount of open water, the authors discuss the physical characteristics of these surfaces. The major section on *clouds and radiation*, which follows, leads to the estimates of the total radiation balance of the surface and troposphere. In the absence of sufficient measured radiation values, both the shortwave surface input and the longwave radiation (so important a component in the Arctic) have had to be calculated. The main difficulty (as the authors point out) is that the net radiation value is a very small residual of large components and hence highly sensitive to inaccuracies. The results suggest that even in winter the radiative processes predominate with respect to the energy requirements of the atmosphere.

This chapter continues with *evaporation and sensible heat exchange*, and the fundamental consideration of the import of energy into the Arctic through the circulation of the oceans and atmosphere. In the section on *atmospheric circulation and advection*, and the short section which follows on *climatic features* (including studies by Prik), the work rests more firmly on observed data. The decade 1951–60 was one of great advance in knowledge of the atmospheric circulation over the Arctic and sub-Arctic. The authors deal with this with admirable clarity, but it remains brief and subservient to the general theme. To conclude, there is a discussion of *the heat budget and stability of Polar Ocean climate*. Vowinckel and Orvig offer various solutions with respect to different ice and cloud covers as well as a general discussion. The references are selective, and extend to 1967. There are 27 tables of station data. For seven of the Russian stations the length of period is shown, but not the actual years; in the case of Barrow and Barter Island, the time is not indicated.

The unity and internal coherence of this study are sustained, and it is a pleasure to read. Maps, diagrams and tables are skillfully integrated. The wealth of illustration adds precision to the regional and seasonal differentiation. However, to appraise the reliability of the individual components of the energy budget the reader must turn to the original publications to find out which data and how many data were used, and how the calculations were carried out. These are fundamental to accepting the results. Since this volume was completed, there has been an upsurge in computer modelling, including several attempts to simulate the effects on climate of changes in the ice surface of the Polar Ocean. This present study points to the kinds of information and measurement which are *still*

needed in order to pursue this approach further. One looks forward to the implementation of a comprehensive POLEX programme.

Knowledge of the *Climate of the Antarctic* has been acquired by an orchestrated effort, particularly during the IGY of 1957-58. This is reflected in Schwerdtfeger's classic study, incorporating the results of many researchers and many countries. Working with measured data, the author proceeds inductively, taking the climatic elements in groups, and concludes with sections on related topics.

After a short introduction to the region and to the availability of meteorological information up to 1969, the climatology opens with a major section on the *radiation and temperature regime*. In discussing the radiation balance, Schwerdtfeger immediately states his case for substituting "quantitative argument for qualitative reasoning" (p. 256), and his combined radiative-dynamic approach. He underlines the complexity and uncertainty of knowledge of the radiation processes over the Antarctic - for example, with respect to cloud and the intense surface inversion. Such considerations may raise doubts "regarding the often quoted unique role of Antarctica as the 'refrigerator of the Southern Hemisphere'"; or they may suggest that the role is due to a combination of radiation effects and the meridional atmospheric circulation (favoured by the height and size of the plateau), rather than to radiation conditions alone. Maintaining this theme, in the next section on atmospheric circulation, *pressure and winds*, Schwerdtfeger emphasizes the remarkable asymmetry of the circumpolar vortex, its geographical persistence and the consequences for western and eastern Antarctica. The illustrations show average conditions. In spite of any shortcomings in the series of daily weather charts, it would have been useful to have had more synoptic material. Of the elements, the *hydrometeors* are the least well-known; the contribution is interesting - thin persistent haze all over the sky which can either be classed as 0 or 10/10 cloud, no-cloud precipitation and so on.

Concluding sections on the Antarctic deal with *annual budgets*: the ice mass budget and changes with time, and the heat budget of the atmosphere; *climate change*: a summary of evidence suggests a possible increase in snow accumulation in the interior and a decrease in coastal regions. It remains uncertain as to whether it is continent-wide; and finally, *brief topics*, including variable atmospheric constituents, spring warming of the stratosphere, cooling power as a climatic index (the only brief concession to applied climatology in the volume), the Antarctic peninsula as a climatic divide, dry valleys and oases. The reference list is comprehensive and up to 1969. There are 25 station tables.

Schwerdtfeger's presentation is masterly, the style clean, concise, the illustrations well-chosen and carefully integrated into the text. A small point, but to have indicated the degrees of latitude and longitude on the Antarctic maps would have been helpful. This appears to have been the last manuscript received, both from the point of view of references and the inclusion of such recent material as the GHOST balloon flights and results from the CRREL deep ice-core studies. None of the authors has included any information from the weather satellite programme.

As Editor, Dr. Orvig opens the volume with the statement that "climatology is usually defined as being the description of average weather conditions", and offers an interesting critical discussion of the use of 30-year mean climatology with particular reference to the Polar regions. It is timely to point out the over-dependence on this single model in climatology in the past, and the time-period is certainly a matter of debate, especially in marginal regions as Orvig remarks. However, let us not throw out the baby with the bath water. The full use of the statistical model based on the normal distribution (*when appropriate*) offers both insights and strict limitations as does any other, and would seem far more flexible an analytical tool than is conceded here. It is perhaps not so much the concept as the frequent misuse and abuse which is under contention.

In this volume it is the occasional description quoted from an expedition observer that momentarily brings the study to life and catches the imagination. Perception of the weather by a receptive observer will perhaps always remain a key factor in the understanding of climate. And there is so much in the nature of the climate and of past climatic events in

Polar regions to stimulate the scientific imagination, so much in the opposing and varied nature of the surface geography of the two poles to offer unparalleled opportunities for comparison, in the study of differences in process, for sifting out the essentials. The present study will be invaluable for indicating future directions for polar research.

Cynthia Wilson
(formerly) Centre d'Etudes Nordiques
Université Laval
Québec

CLOUDS, RAIN AND RAINMAKING. 2nd edition. B.J. Mason. MacMillan of Canada, Toronto, 1975, 189 pp., hardcover, \$16.95.

B.J. Mason's "Clouds, Rain and Rainmaking", 2nd edition, is a considerably revised and somewhat expanded version of his concise introduction to cloud physics which was first published in 1962. At that time, it was available in a paperback edition, with yellowish pages, for \$1.95. The new edition is available only in hardcover, on higher quality white paper, at a price of \$16.95.

The book consists of seven chapters which begin with a description of the macroscopic features of clouds and weather systems and continue with a description of cloud micro-physics and the generation of precipitation in various forms. The final chapters deal with weather modification and thunderstorm electrification. This book is well organized and, with minor exceptions, quite lucid and readable. Being a mere 189 pages long, it can be rapidly digested to give the educated layman an overview of the current state of cloud physics as Mason sees it. Unfortunately, its brevity is also a drawback since it means that the book leans heavily on the author's more weighty tome 'The Physics of Clouds' for both the detailed derivation of the equations and for references to original research. Consequently, it cannot stand by itself as a textbook in cloud physics, although it could serve a useful function as supplementary reading material for a survey course in meteorology. It can also be recommended to the specialist in another branch of meteorology who wishes to learn some of the terminology and theory of cloud physics.

The book is largely descriptive. There are forty or so equations which the author uses primarily to make order of magnitude calculations or to draw illustrative graphs. However, understanding of the equations is not essential and the non-mathematical reader could probably ignore them without serious loss except perhaps in the final chapter on electricity. Ample illustrations, including graphs, line drawings and a good collection of black and white photographs, support the textual material. In the new edition, the photographs have been removed from the centre of the book and placed in the text where they belong. This was judged a convenience. Another useful feature of the book consists of brief descriptions of several illustrative experiments which can be carried out by the reader with the aid of fairly simple home-made equipment.

The process of updating the book has been quite thorough. Few pages have not received at least minor amendments and, in places, fairly substantial additions and deletions have been made, dropping outmoded theories and introducing new ideas which have appeared during the past thirteen years. As an example, Bowen's theory of extraterrestrial ice nuclei now receives short shrift, but Mason's own theory on the inductive charging of ice pellets has been extensively presented. Examples of other new concepts which have been introduced into the 2nd edition include the stochastic model of raindrop growth, organic ice nuclei (but not biogenic nuclei), Doppler radar, the randomized cross-over design for weather modification experiments and new developments in cloud-physics instrumentation. The result is an overall addition of about thirty-five pages, much of this extra bulk occurring in the chapters on electrification and weather modification. Inevitably, some old errors have been overlooked and a few new ones introduced. Nevertheless, this reviewer spotted only half a dozen misprints and relatively few errors of fact. The largest hailstone now on record, for example, fell in Coffeyville, Kansas, in 1970 and not in Nebraska, as the

author suggests on p. 115. Further, Fig. 21, which is a map, has no scale. But these are minor points.

One might argue most strongly with the author over questions of opinion and emphasis. He has, for example, almost completely ignored Vonnegut's theory of electrification and, in his eagerness to set forth his own ideas on this subject, he has tended to forget the fact that many readers will have little more than an elementary knowledge of basic physics. His skepticism concerning the possible success of any large-scale weather modification attempts pervades the chapter on rainmaking experiments (a misnomer in a sense since the author also discusses snow augmentation and hail suppression). Nevertheless, Dr. Mason has been perhaps the most prominent scientist in cloud physics, and if one wishes to obtain the insights into the field which he provides in this book, one must also be prepared to be exposed to his scientific and philosophical bias.

E.P. Lozowski
The University of Alberta
Edmonton

FACULTY OPENING

UNIVERSITY OF WATERLOO, DEPARTMENT OF MECHANICAL ENGINEERING, requires an assistant professor to teach undergraduate and graduate courses in fluid mechanics and to supervise research in environmental fluid mechanics. Applicants should have an engineering background, a doctorate or equivalent and research interests in air pollution, air-water interactions and/or large scale atmospheric motions. Appointment to commence on or about September 1, 1976. Send résumé to Dr. D. J. Burns, Professor and Chairman, Department of Mechanical Engineering, University of Waterloo, Waterloo, Ontario.

4th CANADIAN SYMPOSIUM ON REMOTE SENSING

The 4th Canadian Symposium has been scheduled for May 16, 17 and 18, 1977, in Québec City, Québec. The Department of Lands and Forests of the Province of Québec will host the meeting, which is sponsored by the Canadian Remote Sensing Society of the Canadian Aeronautics and Space Institute and other professional societies and government departments.

The Symposium will examine Remote Sensing as a vital and mature technology which embodies conceptual problem definition, technological development, and proven application. It hopes to demonstrate the wide applicability of particular sensors and interpretation algorithms in a way which enhances our appreciation of the interdependence of processes on the earth's surface, its water bodies and in the atmosphere.

Those wishing to present a paper at the 4th Canadian Remote Sensing Symposium are asked to send a detailed, comprehensive summary of 250 words (in English or French) no later than *September 30, 1976*, to the address given below. Since selection of papers to be presented at the meeting will be based upon this summary, it must include an outline of the problem, methods used in its solution, and results obtained. Papers accepted for presentation will be refereed prior to publication in the Symposium Proceedings. Papers may be presented in either English or French.

Dr. J. Kruus
Technical Program Chairman
4th Canadian Symposium on Remote Sensing
Canada Centre for Remote Sensing
2464 Sheffield Road
Ottawa, Ontario
K1A 0E4

APPEL DE TEXTES

LE 4ème SYMPOSIUM CANADIEN SUR LA TELEDETECTION

Le 4ème Symposium canadien se tiendra dans la ville de Québec les 16, 17 et 18 mai 1977. Le Ministère des Terres et Forêts du Québec sera l'hôte de cette réunion, sous l'égide de la Société canadienne de Télédétection de l'Institut canadien de l'Espace et de l'Aéronautique et de divers ministères et sociétés professionnelles.

Le Symposium a pour objet d'analyser la télédétection comme une technologie essentielle et ayant atteint la maturité à la fois sur le plan de la définition des orientations, du développement technologique et des applications concrètes. Il vise à démontrer que certains capteurs et algorithmes d'interprétation accroissent considérablement notre capacité de perception des interrelations entre les processus présent sur la surface de la terre, ses eaux et dans notre atmosphère.

Ceux qui désirent présenter un article au 4ème Symposium canadien sur la télédétection sont priés d'envoyer un résumé clair et détaillé de 250 mots (en français ou en anglais) avant le *30 septembre 1976* à l'adresse ci-dessous. Puisque ce résumé servira au choix des articles présentés au Symposium, il devra comprendre un aperçu du problème, des méthodes utilisées pour sa solution et des résultats obtenus. Les articles retenus pour fins de présentation seront arbitrés avant d'être publiés dans les comptes rendus du Symposium. Les articles peuvent être présentés en français ou en anglais.

Dr. J. Kruus
Président du Comité technique
4ème Symposium canadien sur la télédétection
Centre canadien de télédétection
2464, rue Sheffield
Ottawa, Ontario
K1A 0E4

INFORMATION FOR AUTHORS

Editorial policy. *Atmosphère* is a medium for the publication of the results of original research, survey articles, essays and book reviews in all fields of atmospheric science. It is published quarterly by the CMS with the aid of a grant from the Canadian Government. Articles may be in either English or French. Contributors need not be members of the CMS nor need they be Canadian; foreign contributions are welcomed. All contributions will be subject to a critical review before acceptance. Because of space limitations articles should not exceed 16 printed pages and preferably should be shorter.

Manuscripts should be submitted to: *Atmosphère*, Dept. of Meteorology, McGill University, P.O. Box 6070, Montreal, Quebec H3C 3G1. Three copies should be submitted, typewritten with double spacing and wide margins. Heading and sub-headings should be clearly designated. A concise, relevant and substantial abstract is required.

Tables should be prepared on separate sheets, each with concise headings.

Figures should be provided in the form of three copies of an original which should be retained by the author for later revision if required. A list of legends should be typed separately. Labelling should be made in generous size so that characters after reduction are easy to read. Line drawings should be drafted with India ink at least twice the final size on white paper or tracing cloth. Photographs (halftones) should be glossy prints at least twice the final size.

Units. The International System (SI) of metric units is preferred. Units should be abbreviated only if accompanied by numerals, e.g., '10 m', but 'several metres.'

Footnotes to the text should be avoided.

Literature citations should be indicated in the text by author and date. The list of references should be arranged alphabetically by author, and chronologically for each author, if necessary.

RENSEIGNEMENTS POUR LES AUTEURS

Politique éditoriale. *Atmosphère* est un organe de publication de résultats de recherche originale d'articles sommaires, d'essais et de critiques dans n'importe lequel domaine des sciences de l'atmosphère. Il est publié par la SMC à l'aide d'une subvention accordée par le gouvernement canadien. Les articles peuvent être en anglais ou en français. Il n'est pas nécessaire que les auteurs soient membre de la SMC; les contributions étrangères sont bien-venues. A cause des limitations d'espace les articles ne doivent pas dépasser 16 pages dans le format final. Tout article sera soumis à un critique indépendant avant d'être accepté.

Les manuscrits doivent être envoyés à: *Atmosphère*, Dépt. de Météorologie, L'Université McGill, C.P. 6070, Montréal, Québec H3C 3G1. Ils doivent être soumis en trois exemplaires dactylographiés à double interlignes avec de larges marges. Les titres et sous-titres doivent être clairement indiqués. Chaque article doit comporter un résumé qui soit concis, pertinent et substantiel.

Les tableaux doivent être préparés et présentés séparément accompagnés d'un titre et d'un numéro explicatifs concis.

Les graphiques doivent être présentés en trois copies dont les originaux devraient être conservés par l'auteur au cas où ils seraient nécessaire de les reviser. Une liste des légendes des graphiques doit être dactylographiée séparément. L'étiquetage doit être de grand format de façon à ce qu'il soit facilement lisible après réduction du format. Le traçage des lignes doit s'effectuer au moyen d'encre de chine en doublant, au moins, le format final, le tout sur papier blanc ou sur papier à calquer et identifié adéquatement. Les photographies (demi-teintes) devraient être présentées sur épreuves glacées au double du format final.

Les unités. Le Système International (SI) d'unités métriques est préférable. Les unités devraient être abrégées seulement lorsqu'elles sont accompagnées de nombres, ex: "10m", mais "plusieurs mètres".

Les notes de renvoi au texte doivent être évitées.

Les citations littéraires doivent être indiquées dans le texte selon l'auteur et la date. La liste des références doit être présentée dans l'ordre alphabétique, par auteur et, si nécessaire, dans l'ordre chronologique pour chaque auteur.

The Canadian Meteorological Society / La Société Météorologique du Canada

The Canadian Meteorological Society came into being on January 1, 1967, replacing the Canadian Branch of the Royal Meteorological Society, which had been established in 1940. The Society exists for the advancement of Meteorology, and membership is open to persons and organizations having an interest in Meteorology. At nine local centres of the Society, meetings are held on subjects of meteorological interest. *Atmosphere* as the scientific journal of the CMS is distributed free to all members. Each spring an annual congress is convened to serve as the National Meteorological Congress.

Correspondence regarding Society affairs should be directed to the Corresponding Secretary, Canadian Meteorological Society, c/o Dept. of Geography, Simon Fraser University, Burnaby 2, B.C.

There are three types of membership – Member, Student Member and Sustaining Member. For 1976 the dues are \$20.00, \$5.00 and \$60.00 (min.), respectively. The annual Institutional subscription rate for *Atmosphere* is \$15.00.

Correspondence relating to CMS membership or to institutional subscriptions should be directed to the University of Toronto Press, Journals Department, 5201 Dufferin St., Downsview, Ontario, Canada, M3H 5T8. Cheques should be made payable to the University of Toronto Press.

La Société météorologique du Canada a été fondée le 1^{er} janvier 1967, en remplacement de la Division canadienne de la Société royale de météorologie, établie en 1940. Cette société existe pour le progrès de la météorologie et toute personne ou organisation qui s'intéresse à la météorologie peut en faire partie. Aux neuf centres locaux de la Société, on peut y faire des conférences sur divers sujets d'intérêt météorologique. *Atmosphere*, la revue scientifique de la SMC, est distribuée gratuitement à tous les membres. À chaque printemps, la Société organise un congrès qui sert de Congrès national de météorologie.

Toute correspondance concernant les activités de la Société devrait être adressée au Secrétaire-correspondant, Société météorologique du Canada, Département de Géographie, L'Université Simon Fraser, Burnaby 2, B.C.

Il y a trois types de membres: Membre, Membre-étudiant, et Membre de soutien. La cotisation est, pour 1976, de \$20.00, \$5.00 et \$60.00 (min.) respectivement. Les Institutions peuvent souscrire à *Atmosphère* au coût de \$15.00 par année.

La correspondance concernant les souscriptions au SMC ou les souscriptions des institutions doit être envoyée aux Presses de l'Université de Toronto, Département des périodiques, 5201 Dufferin St., Downsview, Ontario, Canada, M3H 5T8. Les chèques doivent être payables aux Presses de l'Université de Toronto.

Council / Conseil d'Administration 1976-77

President/Président – J.E. Hay
Vice President/Vice-Président – K.F. Harry
Past President/Président sortant –
P.E. Merilees
Corresponding
Secretary/Secrétaire-correspondant –
R.B. Sagar
Treasurer/Trésorier – D.G. Schaefer
Recording Secretary/
Secrétaire d'assemblée – L.E. Parent

Councillors-at-large/Conseillers
– M.G. Ferland, D.B. Fraser,
A.D.J. O'Neill
Chairmen of Local Centres/Présidents des centres
Oceanography Division/Division
d'océanographie:
Chairman/Président – D.M. Farmer
Secretary/Secrétaire – P.H. LeBlond
Councillors/Conseillers – E.P. Jones,
B. Sundby

ATMOSPHERE

Editor/Rédacteur – I.D. Rutherford
Associate Editors/Rédacteurs associés – J. Derome, C. East, J.B. Gregory, W. Gutzman, P.H. LeBlond, R. List, C.L. Mateer, G.A. McBean, D.N. McMullen, P.E. Merilees, R.R. Rogers, V.R. Turner, R.E. Thomson, E.J. Truhlar, E. Vowinckel

Sustaining Members/Membres de soutien – Air Canada. – MacLaren Atlantic Ltd.